

Note: Figs 4, 6, 7a-j and 8 are slightly degraded to make the total file size not too large. A gzipped postscript file of this paper that shows better versions of these figures can be found at <ftp://astro.princeton.edu/library/preprints/pop843.ps.gz>

The Distribution of Thermal Pressures in the Interstellar Medium from a Survey of C I Fine-Structure Excitation¹

Edward B. Jenkins and Todd M. Tripp

Princeton University Observatory

Princeton, NJ 08544-1001; ejb@astro.princeton.edu, tripp@astro.princeton.edu

ABSTRACT

We used the *Space Telescope Imaging Spectrograph* (STIS) with its smallest entrance aperture ($0''.03$ wide slit) and highest resolution echelle gratings (E140H and E230H) to record the interstellar absorption features for 10 different multiplets of neutral carbon at a resolving power of $\lambda/\Delta\lambda = 200,000$ in the UV spectra of 21 early-type stars. Our objective was to measure the amount of C I in each of its three fine-structure levels of the ground electronic state, so that we could determine the thermal pressures in the absorbing gas and how much they vary in different regions. Our observations are principally along directions out to several kpc in the Galactic plane near longitudes $\ell = 120^\circ$ and 300° , with the more distant stars penetrating nearby portions of the Perseus and Sagittarius-Carina arms of the Galaxy. We devised a special analysis technique to decipher the overlapping absorption features in the different multiplets, each with different arrangements of the closely spaced transitions. In order to derive internally consistent results for all multiplets, we found that we had to modify the relative transition f -values in a way that made generally weak transitions stronger than amounts indicated in the current literature.

We compared our measured relative populations of the excited fine-structure levels to those expected from equilibria calculated with collisional rate constants for various densities, temperatures and compositions. The median thermal pressure for our entire sample was $p/k = 2240 \text{ cm}^{-3} \text{ K}$, or slightly higher if the

¹ Based on observations with the NASA/ESA Hubble Space Telescope obtained at the Space Telescope Science Institute, which is operated by the Association of Universities for Research in Astronomy, Incorporated, under NASA contract NAS5-26555.

representative temperatures of the material are much above or below a most favorable temperature of 40K for the excitation of the first excited level at a given pressure. For gas that is moving outside the range of radial velocities permitted by differential Galactic rotation between us and the targets, about 15% of the C I indicates a thermal pressure $p/k > 5000 \text{ cm}^{-3} \text{ K}$. For gas within the allowed velocities, this fraction is only 1.5%. This contrast reveals a relationship between pressure enhancements and the kinematics of the gas.

Regardless of velocity, we usually can register the presence of a very small proportion of the gas that seems to be at $p/k \gtrsim 10^5 \text{ cm}^{-3} \text{ K}$. We interpret these ubiquitous wisps of high pressure material to arise either from small-scale density enhancements created by converging flows in a turbulent medium or warm turbulent boundary layers on the surfaces of dense clouds moving through an intercloud medium. For turbulent compression, our C I excitations indicate that the barotropic index $\gamma_{\text{eff}} \gtrsim 0.90$ must apply if the unperturbed gas starts out with representative densities and temperatures $n = 10 \text{ cm}^{-3}$ and $T = 100 \text{ K}$. This value for γ_{eff} is larger than that expected for interstellar material that remains in thermal equilibrium after it is compressed from the same initial n and T . However, if regions of enhanced pressure reach a size smaller than $\sim 0.01 \text{ pc}$, the dynamical time starts to become shorter than the cooling time, and γ_{eff} should start to approach the adiabatic value $c_p/c_v = 5/3$.

Some of the excited C I may arise from the target stars' H II regions or by the effects of optical pumping from the sub-millimeter line radiation emitted by them. We argue that these contributions are small, and our comparisons of the velocities of strongly excited C I to those of excited Si II seem to support this outlook.

For 6 stars in the survey, absorption features from interstellar excited O I could be detected at velocities slightly shifted from the persistent features of telluric origin. These O I* and O I** features were especially strong in the spectra of HD 93843 and HD 210839, the same stars that show exceptionally large C I excitations.

In appendices of this paper, we present evidence that (1) the wavelength resolving power of STIS in the mode we used is indeed about 200,000, and (2) the telluric O I* and O I** features exhibit some evidence for macroscopic motions, since their broadenings are in excess of that expected for thermal Doppler broadening at an exospheric temperature $T = 1000 \text{ K}$.

Subject headings: ISM: atoms — ISM: kinematics and dynamics — ISM: lines and bands — techniques: spectroscopic — ultraviolet: ISM

1. Introduction

The many diverse ways now available to observe the interstellar medium (ISM) in the Galactic disk has brought about an awareness that the gas exhibits a vast range of densities and temperatures, along with large contrasts in the molecular fractions and degrees of ionization. In large part, the extremes in these quantities arise from the gas being driven by injections of energy and momentum from the impulsive, far-reaching disturbances created by shock waves arising from supernova explosions (McKee & Ostriker 1977; McCray & Snow 1979; Mac Low, McCray, & Norman 1989) whose energy inputs are sufficient to maintain a network of very hot gases in the disk of the Galaxy (Cox & Smith 1974; Smith, 1977; Jones et al. 1979).

Supplementing the disturbances created by explosions are the much more gradual effects from certain classes of stars (Abbott 1982; McKee 1986). For instance, stars that have bipolar outflows (Bally 1982; Genzel & Downes 1982; Königl 1996) or have large rates of mass loss while they are on the main sequence (Lamers 1981) have a strong influence on the dynamics and physical state of the gas that surrounds them. Spherically symmetric outflows should create volumes of hot, low density gas surrounded by dense shells of cooler gas (Castor, McCray, & Weaver 1975; Weaver et al. 1977). Adding to the effects of direct mechanical energy are pressurizations which arise from the ultraviolet radiations from hot stars that rapidly create zones of fully ionized gas whose temperatures are much higher than that of the ambient, initially neutral material. For a brief time, such regions can have substantially elevated thermal pressures that are eventually relieved by a dynamical response.

Taken together, supernovae and their accompanying young stellar associations represent sources that are largely responsible for creating some of the vivid contrasts in conditions, along with distinctive morphological signatures manifested in the forms of shells and loops (Heiles 1979). The outcomes from these disturbances are made even more conspicuous by the tendency for many of these sources to act together, since they are clustered in space and time. Their direct effects also bring about various secondary processes that influence the state of the gas, such as interactions from Alfvén waves (Elmegreen 1997), density fluctuations caused by turbulence (Vázquez-Semadeni, Passot, & Pouquet 1995; Ballesteros-Paredes, Vázquez-Semadeni, & Scalo 1999), and the nonlinear responses of gaseous material arising from thermal and gravitational instabilities (Wada, Spaans, & Kim 2000). In high density clouds, these processes and their compound effects play an important role in star formation.

From a superficial viewpoint, gases in the Galactic disk show an inverse relationship between density and temperature, leading to an approximate equality of thermal pressure

$p = nkT$ for different locations. While this may be true for the simplest depiction of the states of widely different phases of the gas in the Galactic disk, it is unlikely to hold over small scales and at all times. The weight of material within the Galactic gravitational potential produces a substantial reservoir of total pressure $p_{\text{total}}/k \approx 3 \times 10^4 \text{ cm}^{-3} \text{ K}$ (Boulares & Cox 1990), made up of several sources that supplement the thermal one, such as turbulence, cosmic rays and magnetic fields. Under the right conditions, these other forms can be transformed into temporary excesses or rarefactions in thermal pressure. Our purpose in studying thermal pressures is to examine the inevitable deviations that must arise from the random, tempestuous character of the medium. Any information that we can gather about base pressure value together with the size and character of fluctuations around this value represent a valuable constraint for theories on the processes that shape the global conditions of the ISM.

An excellent probe of densities and temperatures in diffuse H I regions is the relative population of neutral carbon atoms in excited fine-structure levels of the ground electronic state. The levels' energy separations, collisional excitation rate constants, and spontaneous radiative decay rates are ideal for differentiating different regimes of density and temperature that are expected in this particular phase of the ISM. The first large scale survey of C I absorption features in the uv spectra of hot stars was carried out by Jenkins & Shaya (1979), who used the spectrometer on the *Copernicus* satellite (Rogerson et al. 1973). The sample size was doubled by a subsequent survey, again with *Copernicus*, carried out by Jenkins, Jura & Loewenstein (1983). In a discussion of the outcomes from both surveys, Jenkins et al. (1983) were not able to recover the full distribution of pressures from their data because a substantial fraction of the cases had large uncertainties. Nevertheless, they were able to express quantitatively the relative fraction of material at either extremely low or high pressures. These conclusions gave some guidance on the applications of general theories of the ISM that had just been developed, such as the calculations of random pressure fluctuations caused by supernova explosions (McKee & Ostriker 1977) and the crushing effects on clouds overtaken by blast waves (Cox 1979, 1981).

A significant investment in space astronomy technology and facilities since the launch of *Copernicus* almost 30 years ago now enables us to greatly surpass the earlier achievements in studying C I absorption features. Over the last decade, a number of studies have provided interesting new insights on physical conditions based on interpretations of the C I fine-structure excitation. In an early observation using the *Goddard High Resolution Spectrograph* (GHRS) on the *Hubble Space Telescope* (HST), Smith et al. (1991) studied the C I absorptions along line of sight to ξ Per and found evidence for large contrasts in conditions for components at different radial velocities. Jenkins & Wallerstein (1995) discovered an unusually large fine-structure excitation of C I for high velocity gas in the

Vela supernova remnant, using a spectrum recorded by GHRS at intermediate resolution (with the G160M grating) for the star HD 72089. This result was confirmed and recorded in more detail by Jenkins et al. (1998) using the *Space Telescope Imaging Spectrograph* (STIS) (Kimble et al. 1998; Woodgate et al. 1998), a later generation spectrograph that replaced GHRS. Wannier et al. (1999) explored the physical conditions in the outer envelope of the B5 molecular cloud in Perseus by recording 3 C I multiplets (plus a CO absorption band) in the spectra of 3 stars at strategic locations behind the cloud’s periphery.

In this paper, we report on our use of STIS to record the spectra of 21 early-type stars. The power of STIS to record many wavelength elements simultaneously allowed us encompass ten different C I multiplets with only a modest amount of effort. To achieve the best possible wavelength resolution to differentiate parcels of gas with small separations in radial velocity, we employed the highest resolution modes of the echelle spectrograph (E140H and E230H) and used its narrowest entrance slit ($0''.03$ wide). As shown by the results in Appendix A, the spectrograph in this configuration yields $\lambda/\Delta\lambda = 200,000$, a resolving power ten times greater than that of *Copernicus* and at least twice as good as the highest resolution echelle grating on GHRS. This is especially beneficial for studying C I, since its features probably behave very much like those of other neutral species that are normally expected to be in the singly-ionized state in H I regions, such as Na I and K I. It is well documented that Na I and K I can have widths narrower than 1 km s^{-1} (Welty, Hobbs, & Kulkarni 1994; Welty & Hobbs 2001).

The observing program was organized to yield a good sampling of directions within the limits of HST observing time allocated for the project. The details of target selection and STIS observing configurations are discussed in §2 and §3, respectively. In §4 we discuss various phases of the data reduction, including the correction for scattered light for obtaining a proper zero level for intensities (§4.1), the sensing and elimination of a high-frequency modulation of the spectrum caused by uneven responses to half-pixel photoevents by the detector’s electronics (§4.2), special precautions to co-align the wavelengths of separate exposures before they were combined (§4.3), our method of defining the continuum levels above the absorption features (§4.4), and the means we used to register accurately the wavelengths from one multiplet to another (§4.5).

The C I multiplets consist of complex blends of individual lines from different fine-structure levels. The patterns vary from one multiplet to the next, and in §5.1–5.2 we describe a special analysis technique that takes advantage of these changes to unravel the structures of the velocity profiles in the absence of such interference. However, to obtain self-consistent results for all of the multiplets, we found it necessary to adjust their relative f -values. This was done by a special analysis of all of the data in the survey, as described

in §5.3, followed by various checks to show that outcomes were not influenced by fine-scale structures in the C I velocity profiles that were saturated but still not resolved by the instrument (§5.3.2). Section 5 ends with one subsection that presents an example of profile reconstructions to show that the outcome of the analysis is consistent with the input data (§5.4) and another that discusses various sources of error in the results (§5.5).

After some introductory remarks in §6.1, we describe in §6.2 our calculations for the expected fine-structure population ratios for various interstellar conditions and compositions (§6.2). A graphical means for comparing for each line of sight the C I population ratios with these expected values is presented in §6.3, followed later by a general discussion on the implications from the entire survey in §7 and how the findings relate to the kinematics of the gas in §7.5. Accompanying these main arguments are some digressions on a few detections of the absorptions by neutral oxygen atoms in excited fine-structure states (§6.4), the unusual conditions seen toward one star, HD 210839 (§6.5), and a simple check (§7.2) on some of the more surprising outcomes expressed in §7.1 that bypasses the assertion that the f -values need revision, as we claimed earlier in §5.3. In §§7.3,7.4 we cover the possibility that some small fraction of the C I might arise from H II regions instead of H I regions. Finally, in the discussion section (§8) we present our interpretation that the admixtures of small amounts of high-pressure gas with the ordinary material may signify the presence of density enhancements that arise from turbulence, and that perhaps this is the same phenomenon that is responsible for small-scale structures in the gas.

2. Selection of Targets

Our objective was to obtain moderately good signal-to-noise ratios (S/N) on as many targets as possible within our allocation of HST orbits for this program. To accomplish this, we chose targets that were in the Continuous Viewing Zone (CVZ) of HST, thus eliminating the losses of time caused by Earth occultations. The advantage in integration time is about a factor of two over non-CVZ targets. A few targets were outside the CVZ; these targets were chosen to satisfy the requirements of another research program which had pooled its orbital allocations with ours. A consequence of our favoring the CVZ is that the galactic longitudes of the targets are clustered around $\ell = 120^\circ$ and 300° .

The target stars in our survey are listed in Table 1. They were selected such that their predicted ultraviolet fluxes would yield far-UV MAMA global count rates just below the maximum permitted value of $2 \times 10^5 \text{ s}^{-1}$. Generally, stars that were expected to have much lower count rates were disfavored, again in the spirit of maximizing the S/N in a short observing time. We generally tried to avoid stars that had visual binary companions that

might complicate the acquisition process, but there were several exceptions that did not pose any problems. These stars can be identified in Table 1 as ones with an “A” following the HD number. To make the interstellar features easy to separate from stellar ones, we chose stars that had large projected rotational velocities (listed in column 4 of Table 1).

Noteworthy information about the targets is given in Table 1, such as the identification by HD number (col. 1), spectral classification (col. 2), radial velocity (col. 3), projected rotational velocity $v \sin i$ (col. 4), V magnitude (col. 5), and the far-UV continuum flux F_λ at 1300 Å (col. 6). Readers are cautioned against using flux values obtained from our observations in the HST archive, since they do not consider the effect from the reduced transmission of the narrow entrance slit. The last two columns of the table show important parameters for our observations. Column 7 lists the S/N that we obtained at the most favorable wavelength (1280 Å) for obtaining a strong signal with the E140H observing mode. Approximate values of S/N for multiplets at wavelengths well removed from this one can be calculated by multiplying S/N_{1280} by the numbers in parentheses below the multiplet identifiers in column 1 of Table 3. The identification numbers for the exposures that exist in the HST archive are given in column 8. Readers who wish to know the exact details about the exposures (observing dates, durations, etc.) may construct the appropriate tables in this archive (these observations are listed under Program ID’s 8043 and 8484).

Various parameters that pertain to the lines of sight and are relevant to the interstellar conditions are given in Table 2. For each line of sight identified by the star’s HD number (col. 1) we give the galactic coordinates (cols. 2–3), estimated distance (col. 4), the difference between radial velocities in the heliocentric system and the Local Standard of Rest (LSR) (col. 5), the expected radial velocity at the position of the star arising from differential galactic rotation (col. 6), $B - V$ color excess (col. 7), and H I column density (col. 8).

Table 1. Target Stars and Exposures

HD (1)	Sp. Type & [Ref.] ^a (2)	v_* ^b (km s ⁻¹) (3)	$v \sin i$ ^c (km s ⁻¹) (4)	V ^d (5)	F_λ ^e (1300 Å) (6)	S/N (1280 Å) (7)	HST Archive Rootname (8)
108	O6:f?pe [5] ^f	−63 ^g	115 ^h	7.40	2.0	25	O5LH01010–1080
3827	B0.7 V((n)) [4]	−22 ^g	125 ^h	8.00	13.	36	O54359010–9030
15137	O9.5 II–III(n) [4]	−35 ^g	135 ^h	7.87	1.8	25	O5LH02020–2050
69106	B0.5 IVnn [7]	+6 ^g	320 ^h	7.14	13.	42	O5LH03010–3050
88115	B1.5 IIn [7]	−18 ^g	245 ^h	8.30	2.2	23	O54305010–5060
93843	O5.5 III(f) [7]	−9 ^g	90 ^h	7.33	9. ⁱ	35	O5LH04010–4040
94493	B1 Ib [7]	−1 ^g	145 ^h	7.27	5.	26	O54306010, 6020
99857A	B0.5 Ib [7]	−10 ^g	180 ^h	7.45	3.0	31	O54301010–1060
103779	B0.5 Iab [7]	−9 ^j	78 ^k	7.21	7.	25	O54302010, 2020
106343	B1.5 Ia [7]	−7 ^g	85 ^h	6.22	3.8 ^l	28	O54310010, 0020
109399	B0.7 II [7]	−50 ^g	125 ^h	7.62	5.	24	O54303010, 3020
116781A	B0 IIIne [7]	7.60	4.	22	O5LH05010–5040
120086	B3 III [3]	−1 ^g	120 ^h	7.87	8.	30	O5LH06010–6050
122879	B0 Ia [7]	2 ^g	92 ^k	6.41	9.	35	O5LH07010–7040
124314A	O6 V(n)((f)) [6]	−13 ^g	270 ^h	6.64	5.	23	O54307010, 7020
203374A	B0 IVpe [2]	−7 ^m	350: ^h	6.68	2.5	30	O5LH08010–8060
206267A	O6.5 V [5] ⁿ	−8 ^m	155 ^h	5.62	5.	23	O5LH09010–9040
208947	B2 V [1] ^o	+2 ^m	250 ^h	6.43	...	40	O5LH0A010–A040
209339A	B0 IV [2]	−20 ^m	220 ^h	6.65	...	35	O5LH0B010–B040
210839 ^p	O6 I(n)f [5]	−74 ^m	275 ^h	5.04	10.	18	O54304010, 4020

Table 1—Continued

HD (1)	Sp. Type & [Ref.] ^a (2)	v_* ^b (km s ⁻¹) (3)	$v \sin i$ ^c (km s ⁻¹) (4)	V ^d (5)	F_{λ} ^e (1300 Å) (6)	S/N (1280 Å) (7)	HST Archive Rootname (8)
224151	B0.5 II [2] ^q	-26 ^m	115 ^k	6.00	5.	26	O54308010, 8020

^aSources of spectral types: [1] = (Johnson, H. L. & Morgan 1953), [2] = (Morgan, Code, & Whitford 1955), [3] = (Hill, P. W. 1970), [4] = (Walborn 1971). [5] = (Walborn 1972), [6] = (Walborn 1973), [7] = (Garrison, Hiltner, & Schild 1977).

^bStar's heliocentric radial velocity, taken from the indicated sources.

^cStar's projected rotational velocity, taken from the indicated sources.

^d V magnitudes from Mermilliod (1987).

^eStar's continuum flux at 1300 Å, measured from large-aperture IUE spectra (except where noted), expressed in units of 10^{-11} erg cm⁻²s⁻¹Å⁻¹.

^fIdentified as a spectroscopic binary by Hutchings (1975), with the secondary being much fainter than the primary. However this duplicity is questioned by Vreux & Conti (1979).

^g (Evans 1967).

^hValues from the catalog of Uesugi & Fukuda (1981) provided by the Vizier web site (Strasbourg Data Center).

ⁱOnly a small-aperture IUE exposure is available. Fluxes scaled using the TD1 flux at 1565 Å reported by Thompson et al. (1978).

^j (Thackeray, Tritton, & Walker 1973)

^k (Howarth et al. 1997).

^lOnly a small-aperture IUE exposure is available. Fluxes scaled using the ANS flux at 1500 Å reported by Wesselius et al. (1982)

^m (Wilson 1953).

ⁿHD 206267 is a strong x-ray source (Schulz, Bergher, & Zinnecker 1997). Its A component is a triple system (Stickland 1995), with the primary being brightest by $\Delta m = 0.8$ (1971).

^oIdentified as a spectroscopic binary by Petrie & Petrie (1967), with $\Delta m = 0.6$.

^pλ Cep

^qIdentified as a spectroscopic binary by Hill & Fisher (1987), with $\Delta m = 2.0$.

Table 2. Lines of Sight

HD (1)	ℓ (deg.) (2)	b (deg.) (3)	Dist. ^a (pc) (4)	$v_{\text{LSR}} - v_{\odot}$ ^b (km s ⁻¹) (5)	$v_{\text{gal. rot.}}$ ^c (km s ⁻¹) (6)	$E(B - V)$ ^d (7)	$\log N(\text{H I})$ ^e (cm ⁻²) (8)
108	117.93	+1.25	2000	8.6	-29.3	0.50	21.53
3827	120.79	-23.23	2100	4.0	-26.7	0.04	20.56
15137	137.46	-7.58	2800	1.6	-34.7	0.33	21.11
69106	254.52	-1.33	1400	-17.2	15.3	0.18	21.08
88115	285.32	-5.53	3700	-12.4	-6.1	0.18	21.02
93843	288.24	-0.90	2900	-11.1	-14.8	0.28	21.33
94493	289.01	-1.18	3500	-11.0	-14.9	0.20	21.11
99857A	294.78	-4.94	3200	-9.9	-26.3	0.34	21.31
103779	296.85	-1.02	3700	-8.9	-30.9	0.22	21.16
106343	298.93	-1.83	3000	-8.4	-32.4	0.29	...
109399	301.71	-9.88	2800	-8.6	-34.1	0.25	21.11
116781A	307.05	-0.07	1900	-5.9	-30.0	0.43	...
120086	329.61	+57.50	1000	7.0	-4.6	0.01	20.41
122879	312.26	+1.79	2400	-4.0	-39.5	0.37	...
124314A	312.67	-0.42	1100	-4.2	-19.3	0.53	21.34

Table 2—Continued

HD	ℓ (deg.)	b (deg.)	Dist. ^a (pc)	$v_{\text{LSR}} - v_{\odot}$ ^b (km s ⁻¹)	$v_{\text{gal. rot.}}$ ^c (km s ⁻¹)	$E(B - V)$ ^d	$\log N(\text{H I})$ ^e (cm ⁻²)
(1)	(2)	(3)	(4)	(5)	(6)	(7)	(8)
203374A	100.51	+8.62	730	13.8	-5.4	0.60	21.11 ^f
206267A ^g	99.29	+3.74	790	13.5	-5.6	0.53	...
208947	106.55	+9.00	510	12.5	-5.2	0.19	...
209339A	104.58	+5.87	1000	12.6	-10.0	0.37	...
210839 ^h	103.83	+2.61	880	12.4	-8.4	0.57	21.15
224151	115.44	-4.64	1100	8.5	-15.7	0.49	21.32

^aSpectroscopic distances computed from the spectral types and V magnitudes given in columns 2 and 5 of Table 1, the color excesses $E(B - V)$ given in column 7 of this table, and using the absolute magnitudes of Vacca et al (1996) for the O stars and Lesh (1968) for the B stars and assuming that $A_V = 3.1E(B - V)$. Known spectroscopic binaries, as noted in Table 1, had their M_V values adjusted as noted. Since we avoided stars with low values of $v \sin i$ (column 4 of Table 1), special corrections in M_V outlined by Lamers et al. (1997) are not needed.

^bCorrection to be added to heliocentric velocity scales shown in Figs. 6–9 to obtain velocities in the “standard definition” of Local Standard of Rest (LSR) (Kerr & Lynden-Bell 1986). While more rigorous derivations (Mihalas & Binney 1981), pp. 389–409) may be more physically accurate and better suited for the analysis presented in §7.5, we retained the standard definition to make it more easy to compare our radial velocities with those reported by radio astronomers.

^cCalculated LSR velocity arising from differential galactic rotation for a point defined by the coordinates given in columns 2 and 3 and the distance in column 4, using the Galactic rotation curve of Clemens (1985) and assuming the Sun is 8.5 kpc from the center of the Galaxy.

^d B and V magnitudes from Mermilliod (1987). Color excess computed using the Johnson’s (1963) intrinsic colors for the spectral types listed in column 2 of Table 1.

^eDerived from Ly α absorption in IUE spectra by Diplas & Savage (1994)

^fFrom Table 2 of Diplas & Savage (1994), hence of reduced accuracy due to uncertain stellar parameters.

^gSituated within IC 1396, an H II region with bright-rimmed globules (Weikard et al. 1996), similar to the Orion Trapezium.

^h λ Cep

3. Observations

All of the targets were observed with both the E140H and E230H echelle modes of STIS (Woodgate et al. 1998) between 1999 February and 2000 August. Since the C I lines were expected to be quite narrow and our analysis benefits from the highest possible resolution, spectra with both gratings were obtained with the $0''.1 \times 0''.03$ slit, the narrowest slit available. Similarly, to maximize the resolution of the data, the spectra were extracted with “Hi-Res” half-pixel centroiding (see §4.2 below). We estimate that this STIS configuration and analysis option provides a resolving power of $R = \lambda/\Delta\lambda \approx 200,000$ or $\text{FWHM} \approx 1.5 \text{ km s}^{-1}$ (see Appendix A). The grating tilts were selected to cover as many of the C I multiplets as possible: the E140H grating was positioned to provide spectra extending from $\sim 1160 - 1361 \text{ \AA}$, while the E230H observations were set up to cover $\sim 1630 - 1902 \text{ \AA}$. While this second setup covers only one C I multiplet – the strongest one at 1657 \AA – it has an additional advantage of covering a weak Si II line at 1808.013 \AA , which is useful to compare with the strong transition from its excited fine-structure level at 1264.738 \AA .

Figure 1 shows a single diffraction order of the E140H grating. Three C I multiplets are visible over the wavelength range covered by this order.

All of the stars are too bright for standard acquisition procedures. Thus the targets had to be initially acquired with a neutral-density filter and then peaked-up in the narrow slit with a low-dispersion grating before switching to the high-dispersion modes for the science exposures.

4. Data Reduction

4.1. Scattered Light Correction

The data were reduced with the CALSTIS routines developed by the STIS Investigation Definition Team. In a number of respects, these routines perform functions that are similar to those of the standard pipeline reductions, so that the calibrated data benefit from the usual flat-fielding, wavelength calibrations, and so forth. Notable exceptions, however, are the extractions with Hi-Res sampling mentioned earlier and a more elegant means of estimating scattered light developed by Lindler & Bowers (2001). This method explicitly accounts for grating scatter from the echelle and cross-disperser elements in STIS (using a model for these effects derived from preflight test exposures), as well as for the point spread functions of the telescope, spectrograph, and MAMA detectors. By comparing spectra with

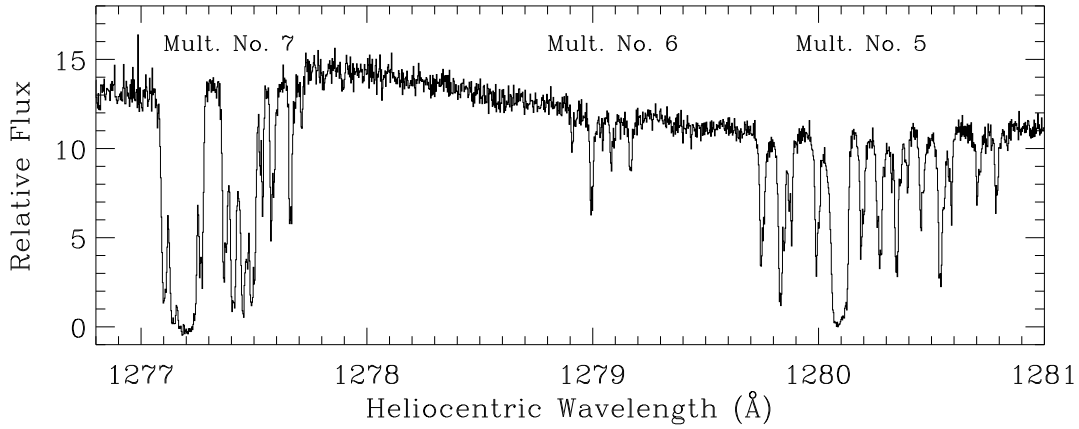


Fig. 1.— A part of the spectrum of HD 210839. This wavelength interval appears in a single diffraction order of the E140H grating on STIS. The three multiplets of C I are identified in Table 3.

and without these corrections, we verified that small-scale artifacts are not being introduced with an amplitude that is large enough to matter for the objectives of our program.

4.2. Rebalancing the Intensities in Adjacent Hi-Res Pixels

To achieve the highest wavelength resolution possible with the output from the STIS MAMA detector (and avoid aliasing with our narrow-slit spectra), we made use of the separate Hi-Res intensity output signals (Woodgate et al. 1998), rather than binning them together in pairs (the usual default with the STIS data products). At times, the raw signals showed a significant, high-frequency modulation that arose from a small imbalance in the responses to the “even-fold” and “odd-fold” events, i.e., ones that contribute to adjacent Hi-Res pixels, as sensed by the outputs from the fine-array elements in the MAMA

detector’s anode (Kasle & Morgan 1991). To overcome this effect, we measured the relative intensity amplitudes of even-numbered pixels with respect to their odd-numbered neighbors and then performed a least-squares fit to the outcomes to create a low-order polynomial representation along each spectral order. (We could not just evaluate a global average for the imbalance, because it changed slowly with position on the detector format.) In performing the fit, the relative weights for these even-odd signal ratios were scaled to the signal strength so that the best-fit polynomial would not be influenced by nonsense information in the middles of strong absorption features with a zero-intensity signal level. After measuring the effect in this manner, we corrected alternate Hi-Res pixels so that their responses would be matched to their neighbors.

4.3. Combining Exposures

Some of the target stars required more than one exposure over a given spectral interval to achieve the desired S/N . Before these exposures were added together to obtain a composite spectrum, we checked for small shifts in the positions of the strongest, sharpest features. All of the spectra that exhibited shifts relative to the first exposure in a sequence were realigned to eliminate the degradation in resolution that would have occurred if the spectra were simply added together in their original form. A typical accuracy in registering one spectrum with respect to another was about 0.2 Hi-Res pixels = 0.14 km s^{-1} , and the largest shifts between spectra were of order 1 Hi-Res pixel = 0.7 km s^{-1} . The intensities for spectra that had non-integral numbers for the magnitudes of their shifts were computed using midpoint interpolations represented by sinc functions (Bracewell 1965, pp. 194–195).

When the spectra were added together, they were assigned relative weights in proportion to the inverse squares of their respective errors. These errors were taken from the error vectors supplied by the CALSTIS routines but subsequently smoothed with a five-point running average. The smoothing reduces the effect that measurements with large positive or negative random noise excursions in individual samples are systematically assigned an inappropriate weight, either too large or too small. New errors ϵ_c for the composite spectrum were derived from the relation $\epsilon_c = (\sum_i \epsilon_i^{-2})^{-0.5}$.

Some multiplets appear simultaneously at opposite ends of two adjacent echelle orders. These multiplets are identified in Table 3 – see note m . We did not combine these separate recordings, since their agreement (or lack thereof) could be used to validate our conclusions about random and systematic errors (§5.5).

4.4. Definition of the Continuum Level

The spectral segments spanning the C I multiplets were normalized to continuum levels defined by the fits of Legendre polynomials to fluxes at wavelengths on either sides of (or between) the lines. A detailed description of the method and its merits has been presented by Sembach & Savage (1992). To be sure that we were not defining continuum levels in places where there were very weak lines, we determined the velocity intervals over which C I could be seen in the strongest lines. These intervals were subsequently marked off for the weaker lines to serve as a guide for regions to avoid when the continuum levels were defined, so that the fitting regions were not contaminated by very weak absorption features. In some cases, we had to violate these guides to constrain the continuum levels over broad expanses of wavelengths that were technically forbidden. When these circumstances arose, we exercised our best judgement on a choice of regions that avoided a downward bias in the outcome.

4.5. Velocity Registration of Multiplets

When we analyzed the results from different multiplets to create a composite picture of the C I, C I* and C I**, we recognized the importance of having an accurate registration of the velocity scales. Otherwise, the velocity resolution of the final result would be inferior to the original resolution of the individual spectra. The wavelength scales supplied by CALSTIS are not accurate enough for this purpose.

To align the spectra, we selected in each multiplet a velocity marker consisting of a feature that was not blended with other transitions. We then used pairs of these markers to measure the relative offsets from one multiplet to the next. In some cases, these shifts were as large as 1.3 km s^{-1} , but usually they were less than 0.4 km s^{-1} . In a few cases where the absorptions from isolated excited fine-structure levels were too weak, we had to use the absorptions out of just the unexcited level, recognizing that, in principle, some were contaminated by nearby lines from excited levels. The alignments started with the weakest multiplets and progressed to successively stronger ones so that the comparisons had the smallest disparities in strength (and hence profile shapes, if they had any asymmetries).

For all but one of the multiplets, the wavelength scales supplied by the STIS data reduction routine were excellent (except for the small offsets described above). The one exception was the echelle order containing the 1657 \AA multiplet. The individual transitions in this multiplet span a large range in wavelength, and it was apparent from the spacing of the absorption features that scale factor for wavelength vs. linear distance on the detector

was slightly incorrect. This is probably caused by the paucity of emission lines supplied by the on-board calibration lamp in this region. We compensated for the error by adding an artificial correction term $\Delta\lambda$ to the published laboratory wavelengths λ in this multiplet, with $\Delta\lambda = 0.002615(\lambda - 1656.15 \text{ \AA})$.

5. Analysis of the C I Multiplets

5.1. General Principles

Figure 1 shows that the complex patterns of velocity components for C I, C I* and C I** overlaid on the closely spaced line configurations within each multiplet often create a strongly overlapping arrangement of absorption that is usually difficult to interpret by simple inspection. If one were to try to avoid this confusion by inspecting only lines with large separations from others or lines at the extreme ends of the multiplet, a very large fraction of the data would be overlooked. This is not a palatable notion, since our objective is to obtain the most accurate results given the resolution and S/N of the data. The challenge, then, is to untangle the overlapping lines and their multiple velocity components, and to do so without sacrificing information where there is overlap. With the analysis of any single multiplet the solution is likely to be ambiguous, since Doppler velocity shifts cannot be distinguished uniquely from the shifts in going from one line to the next. However, the line patterns differ from one multiplet to the next, and this change allows one to resolve the ambiguities if many multiplets are interpreted collectively.

One approach to analyzing the C I multiplets is to create hypothetical absorption models that consist of superpositions of various Gaussian components, compare them to the data, and then modify them so that they converge on the best solution by minimizing the χ^2 of the fit. This is a popular analysis scheme among interstellar line investigators [e.g., Vidal-Madjar et al (1977), Ferlet et al. (1980), Lemoine et al. (1995), Welsh et al., (1990, 1991), Hobbs & Welty (1991), Welty et al. (1991, 1994), Vallerga et al., (1993), Spitzer & Fitzpatrick, (1993, 1995), Fitzpatrick & Spitzer (1994), Crane et al., (1995) and Hébrard et al. (1999)]. However, there is the requirement that the initial definition of the model's properties (such as the number of components and their approximate positions, amplitudes and widths) be based on a subjective initial guess or, alternatively, on evidence from the investigations of lines from other species in the same line of sight. Also, one may end up with the lingering concern that another solution set, created from a different initial trial model or method of convergence, could provide a better fit. Even so, component fitting yields useful insights and has even been employed with good success to C I multiplets with up to 7 identified velocity components (Jenkins & Wallerstein 1995; Jenkins et al. 1998).

For our survey of C I and its excited fine structure states, we wish to avoid the labor-intensive task of model fitting and invoke a purely mechanical analysis method that presents a more objectively derived output product. One such procedure that can be applied to single transitions is the apparent optical depth method (Savage & Sembach 1991), where we first derive an apparent optical depth τ_a as a function of radial velocity,

$$\tau_a(v) = \ln \left(\frac{I_0(v)}{I(v)} \right). \quad (1)$$

from a recorded intensity $I(v)$ and an estimate for the continuum level $I_0(v)$ that would be present in the absence of any absorption. When $\tau_a(v)$ is not so large that noise and uncertainties in the background level create substantial errors, we obtain a differential column density per unit velocity through the relation

$$N_a(v) = 3.768 \times 10^{14} \frac{\tau_a(v)}{f\lambda} \text{cm}^{-2} (\text{km s}^{-1})^{-1}, \quad (2)$$

where f is the transition's oscillator strength and λ is expressed in Å. If the detailed velocity structure is unresolved by the instrument, then the derived $N_a(v)$ is a smoothed version of the true distribution $N(v)$. If there are unresolved narrow structures *and* the lines are strong, then $N_a(v)$ underrepresents $N(v)$ and one must apply a correction at each velocity based on a comparison of $N_a(v)$ for two or more lines of differing strength, much as one would invoke a curve-of-growth analysis for the equivalent widths of saturated lines (Jenkins 1996). We must watch for this effect when we analyze strong absorptions.

5.2. Specific Applications to C I Multiplets

5.2.1. Equations that Unravel Blended Features

As we stated earlier, the features within the multiplets strongly overlap each other, and this precluded our being able to derive $N_a(v)$ for either C I, C I* or C I** by a straightforward application of Eq. 2 to the observed continuum-normalized intensities. Consequently, we had to develop a new method of analysis that could eliminate the profile confusion and present simple representations of the separate $N_a(v)$'s for the three species.

Within a single multiplet that contains a mixture of lines from the three excitation levels, we re-expressed their separate $N_a(v)$ in terms of a collection of discrete unknowns $X_{k,\epsilon}$, with the index k specifying any of L velocity bins and ϵ specifying the level of excitation ($\epsilon = 0, 1, 2$ for C I, C I* and C I**, respectively). For the survey described here, we found it adequate to have $L = 300$ for a contiguous set of bins, each 0.5 km s^{-1} wide,

covering the interval from -100 to $+50 \text{ km s}^{-1}$. No C I lines are apparent outside of this velocity range, except for the star HD 69106, where we had to redefine the velocities to run from -50 to $+150 \text{ km s}^{-1}$.

As with the unknown variables $X_{k,\epsilon}$, we considered the observed optical depths $\tau_a(\lambda)$ over the relevant wavelength interval in terms of a large collection of discrete measurements $\tau_a(i)$ sampled at successive wavelengths $[\lambda_0(i - 200)/6 \times 10^5] + \lambda_0$. (λ_0 is an arbitrary reference wavelength within or near the multiplet.) Associated with each $\tau_a(i)$ is an expectation for the combined contribution from all transitions (each designated with the subscript ℓ) within a multiplet,

$$\tau(i) = C \sum_{\ell} (f\lambda)_{\ell} X_{k,\epsilon} \quad (3)$$

where $C = (3.768 \times 10^{14})^{-1}$, i.e., the inverse of the constant that appears in Eq. 2. For each case ℓ , the index k is set to the nearest integer in the expression

$$k = i - 6 \times 10^5 \frac{\lambda_{\ell} - \lambda_0}{\lambda_0} \quad (4)$$

and ϵ is defined according to the line's originating excitation level. Our objective is to find a solution set for all $X_{k,\epsilon}$ that minimizes

$$\chi^2 = \sum_i \left\{ [\tau_a(i) - \tau(i)] / \sigma_{\tau(i)} \right\}^2 \quad (5)$$

where $\tau(i)$ is the true, composite optical depth given in Eq. 3, but sampled as an apparent optical depth $\tau_a(i)$ with an estimated uncertainty $\sigma_{\tau(i)}$. Noise, systematic uncertainties arising from improper definitions of the continuum level I_0 and the zero-intensity baseline, and the incorrect interpretations of unresolved saturated structures can, in principle, all conspire to make $\tau_a(i)$ slightly different from the real $\tau(i)$.

The derivative of χ^2 with respect to any one of the variables $X_{j,\epsilon}$ is given by

$$\frac{\partial \chi^2}{\partial X_{j,\epsilon}} = -2A \sum_i \sum_{\ell} \left\{ \delta \left[i, \left(j + 6 \times 10^5 \frac{\lambda_{\ell} - \lambda_0}{\lambda_0} \right) \right] (f\lambda)_{\ell} \left[\frac{\tau_a(i) - \tau(i)}{\sigma_{\tau(i)}^2} \right] \right\}. \quad (6)$$

The δ expression is a Kronecker delta that activates the terms only when there is a close match in wavelength between a portion of an individual line's absorption profile with the relevant $X_{j,\epsilon}$. From the argument of δ , it is clear that the meaning of the index j in terms of wavelength offsets is the same as that for k given in Eq. 4. Nevertheless, j is distinct from k that appears when Eq. 3 is substituted into the expression for $\tau(i)$.

For each of the 900 possible combinations of (j, ϵ) , we have different forms of Eq. 6. The best solutions for $X_{j,\epsilon}$ are found by setting these expressions equal to zero for a minimum in χ^2 and then solving all of the equations simultaneously. In each case, we have an equation that involves a sum of a constant number that includes $\tau_a(i)$, a term that is composed of $X_{j,\epsilon}$ times a coefficient, and then numerous additional terms that include other $X_{k,\epsilon}$ variables that overlap in wavelength (multiplied by other coefficients). By expanding the sums to cover results for many different multiplets, we unravel the ambiguity in the solutions for $X_{j,\epsilon}$ arising from the overlap of the lines in any single multiplet. That is, we can obtain unique answers for all $X_{j,\epsilon}$ by virtue of the different arrangements of the transitions within each multiplet.

A large fraction of the coefficients in the 900×900 matrix for the entire system of equations are zero. The only non-zero ones are those along diagonals that satisfied the identity required by the Kronecker delta of Eq. 6. This condition allows us to take advantage of numerical techniques for solving sparse matrices [e.g., Press et al. (1992)], which makes the problem tractable.

The most elementary way to express the error $\sigma_{\tau(\lambda)}$ is simply to multiply the error in intensity $\sigma_{I(\lambda)}$ by $|d\tau/dI|$ to get $\sigma_{I(\lambda)}/I(\lambda)$. However, this is a poor approximation when $\sigma_{I(\lambda)}$ is not very much less than $I(\lambda)$ or when there are errors in the estimate for the zero level that can have a large relative effect on the derived value of $I(\lambda)$. For this reason, we felt that it was prudent to declare much larger errors for low intensities by creating a modification (the second term in the equation) to yield

$$\sigma_{\tau(\lambda)} = \frac{\sigma_{I(\lambda)}}{I(\lambda)} \times \frac{2}{1 + \tanh[\pi(I - I_t)/0.1]} \quad (7)$$

that doubled the assumed error in the vicinity of transition intensity I_t and made it virtually infinite for intensities that were much lower. The effect of this representation for $\sigma_{\tau(\lambda)}$ is that we essentially discard all intensity measurements below a level of about $I_t - 0.1$ and then provide a smooth transition to the simple form $\sigma_{I(\lambda)}/I(\lambda)$ for much larger intensities.

To arrive at reasonable values for I_t , we studied the departures between a Gaussian distribution in τ with a standard deviation equal to $\sigma_{I(\lambda)}/I(\lambda)$ (i.e., our adopted approximation for the probability density) and the actual distribution that arises from a transformation of a Gaussian distribution with a standard deviation $\sigma_{I(\lambda)}$ through the nonlinear operation of taking a logarithm. This comparison was done for various values of I/I_0 and the signal-to-noise ratio (S/N) at the continuum. For a spectrum with $S/N = 10$, the true probability distribution begins to show moderate differences from the approximation when $I/I_0 = 0.20$, and the deviations become appreciable for lower intensities. For $S/N = 20$ the departures become noticeable only when the intensity

approaches $I/I_0 = 0.15$.

For all multiplets in Table 3 except the ones near 1657 Å (Mult. nr. 2), 1192 Å (Mult. nr. 12) and 1189 Å (Mult. nr. 14), we adopted $I_t = 0.1$ because their S/N generally ranged between 20 and 30. The signal quality for the 3 exceptions was lower, generally $8 < S/N < 12$, so we set $I_t = 0.2$ when their $\sigma_{\tau(\lambda)}$ were evaluated. We believe that these 3 multiplets also have a greater chance of having an incorrect assignment of the zero intensity level, so the absolute insensitivity to intensities lower than $0.1I_0$ seemed warranted. To check that our derivations of N_a were not sensitive to the choice of I_t , we performed a duplicate, experimental analysis where each of the values of I_t were increased by a factor of two. There were only very small changes in the outcomes. The rederivations of f -values described in §5.3.1 are likewise not sensitive to the adopted values of I_t .

Since unwarranted changes in $\sigma_{I(\lambda)}$ may be caused by noise fluctuations in $I(\lambda)$, we needed to take a special precaution that the correlation between the two did not give negative noise spikes an unjustifiably higher weight. To guard against this from happening, we smoothed the $\sigma_{I(\lambda)}$ vector with a 5-point running mean to reduce the correlation.

5.2.2. A Validation of the Method

To demonstrate that the analysis described above gives results that are equivalent to the more traditional techniques of profile fitting, we compare the two for one particular example and show that they yield results that are nearly identical. Jenkins et al. (1998) interpreted the complex pattern of absorption by C I, C I* and C I** toward HD 72089 by defining a set of Gaussian velocity components and then using a component-fitting program developed by one of the authors [E. Fitzpatrick, see e.g., Spitzer & Fitzpatrick (1993) or Fitzpatrick & Spitzer (1997)] to minimize the χ^2 between the data and the components' column densities, central velocities, and velocity dispersions. We now analyze once again the same observations, but this time by using the equations in §5.2.1 that unravel the apparent optical depths.

Figure 2 shows the outcome of the comparison between the two methods. To within the uncertainties that probably arise from differences in defining continuum levels and backgrounds, the outcomes are virtually identical. To make the comparison more meaningful, we used the f -values given by Morton (1991), as done by Jenkins et al (1998), rather than the revised f -values described in §5.3 below.

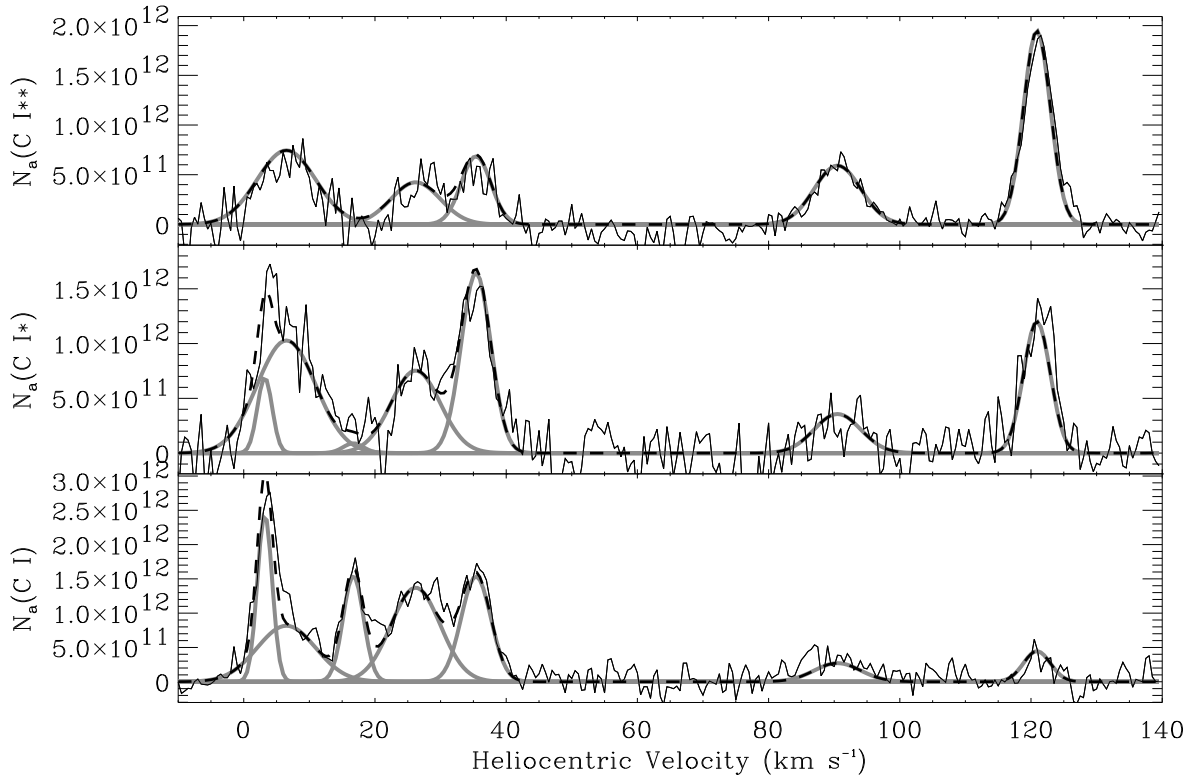


Fig. 2.— A comparison between a re-analysis done here for the STIS observations of C I multiplets in the spectrum of HD 72089 and the original analysis of the same data by Jenkins et al (1998) using a component-fitting technique. Column densities per unit velocity were derived according to the method described in §5.2.1 (top panel: C I^{**}, middle panel: C I^{*}, and bottom panel: C I) and are plotted (thin, solid line) as a function of heliocentric radial velocity. Overplotted on our determinations are the original, best-fitting Gaussian components defined by Jenkins et al (thick, gray lines), and their sum is depicted by a heavy, dashed line.

5.3. Self Consistent f -values

5.3.1. Optical Depth Comparisons

After deriving $X_{j,\epsilon}$ and comparing the observed $\tau_a(i)$ with reconstructions based on Eq. 3, we were not surprised to find systematic differences in the strengths of features compared to their expectations as we went from one multiplet to the next. In the face of inconsistencies, the system of equations discussed above struck a compromise, with appropriate weight factors $\sigma_\tau(i)^{-2}$, between the preferred solutions for lines within the various multiplets. We felt that it was most likely that the differences arise from errors in the published f -values, although we could not rule out additional, probably much smaller contributions from errors in the estimates for the zero intensity levels associated with the observations. On this premise, we chose to solve for revisions in the f -values that gave mutually consistent results. After doing so, we substituted the new f -values into the equations of §5.2 to give modified values for $X_{j,\epsilon}$, ones that we expect are better than those that came from the relative f -values that gave disparate results.

Ultimately, we must trust that the f -values in one of the multiplets are correct, so that we can establish an absolute standard against which the other findings must be found to be in agreement.² Of all the multiplets included in our study, the ${}^3P - {}^3P^0$ multiplet at 1657.2 Å is assigned the highest accuracy (of order 3%) in the compilation by Wiese et al. (1996). Since the energy of this multiplet’s upper state is well isolated from others, deviations from LS coupling are likely to be small. This gave us some confidence about the accuracy of the relative populations of C I in the three levels of excitation, as derived from this multiplet and others that are coupled to it by our comparative analysis.

To solve for the best (relative) f -values, we repeated the general strategy of minimizing the χ^2 that we employed for determining the the best set of $X_{j,\epsilon}$ outlined in §5.2, except that this time we differentiate with respect to the $f\lambda$ under question, which we designate

²One might question why we bothered to derive the f -values of multiplets other than the one we trusted if we were simply adjusting them so that they were consistent with the C I column densities derived from the primary multiplet. There are two answers to this question. First, the lines in a single multiplet can define $N_a(v)$ only under the condition that the appropriate $\tau_a(v)$ ’s are much larger than their respective noise levels or continuum level errors, or, in the case of very strong lines, not so large that the absorptions are nearly saturated. When these conditions are not satisfied, results from the other multiplets must fill in the gaps. Second, we combined the results for many stars to obtain a more accurate set of relative f -values. These generalized results will not automatically give trivial agreements for certain lines with the outcomes for the primary multiplet in any single, given star.

as $(f\lambda)_{\ell'}$. This gives the equation

$$\frac{\partial \chi^2}{\partial (f\lambda)_{\ell'}} = -2A \sum_* \sum_i \left\{ X_{j,\epsilon} \left[\frac{\tau_a(i) - \tau(i)}{\sigma_{\tau(i)}^2} \right] \right\} \quad (8)$$

which may be written for every line in a given multiplet. As before, Eq. 3 gives the expression for $\tau(i)$ and Eq. 4 gives the transformations from i to k . The transformation from i to j is similar, except that the appropriate λ_ℓ is $\lambda_{\ell'}$, i.e., the one for the value of $f\lambda$ that is being considered. The sum with index “*” indicates that we included data for all of the target stars. When we derived solutions to the equations, we needed to consider only one multiplet at a time, since there is no mixing of signals across multiplets.³

After deriving revised f -values, we repeated the determinations of $X_{j,\epsilon}$ since small changes arose from the adjustments to $(f\lambda)_{\ell'}$. We repeated the cycles that alternately implemented Eqs. 6 and 8 until the results converged. Column 7 of Table 3 shows the final outcomes for $\log(f\lambda)$. To give an indication on the consistency of the results from one star to another (by using Eq. 8 without the \sum_* in each case), we computed the median absolute deviation (Mosteller & Tukey 1977) of the individual results from the overall result for all stars. These results are shown in the last column of the table. For the purposes of comparison, we show some previously listed transition strengths in the recent literature (columns 4–6), again in terms of $\log(f\lambda)$.

Generally, from the median absolute deviations from star to star and also the differences in the outcomes for multiplet nrs. 7 and 8.01 that were recorded twice (in different orders) and evaluated separately, we judge that random errors in $\log(f\lambda)$ are of order 0.025 dex. (Exceptions are a few weak lines where the median absolute deviations are extraordinarily large.) This is probably a good measure for the errors in the relative f -values for multiplets whose strengths are about the same order of magnitude. However, in addition to these random errors, we recognize that there could be a gradual buildup in a systematic error as we progress from the strongest multiplets to the weakest ones. This effect can arise from the fact that each multiplet is constrained by ones that are only mildly stronger or weaker. There is no direct coupling between the very strong and the very weak multiplets because at places where the latter are strong enough to register above the noise, the former are saturated and thus of no use. By design, the solutions reflect this by making the $\tau_a(i) - \tau(i)$ terms in Eq. 6 very small compared to their accompanying $\sigma_{\tau(i)}$. As a result, there is no way restrain a gradual, progressive creep in the systematic errors as we go from the strong to the weak multiplets. Unfortunately, the magnitude of this error is difficult to assess.

³While the third line in Multiplet 7.01 at 1277.1901 Å has a wavelength very close to that of the first line in Multiplet 7 at 1277.2454 Å, it is so weak that its contribution should be negligible (see Table 3).

Table 3. New Line Strengths [$\log(f\lambda)$]

		Previously Published $\log(f\lambda)$				This Paper		
Mult.	nr. ^a	λ (Å) ^b	ϵ^c	M91 ^d	WFD96 ^e	ZFC97 ^f	$\log(f\lambda)$	MAD ^g
2 (0.35)	2	1656.2672	1	1.987	1.989	...	h	...
		1656.9283	0	2.367	2.362	...	h	...
		1657.0082	2 ⁱ	2.242	2.236	...	h	...
		1657.3792	1	1.765	1.771	...	h	...
		1657.9068	1	1.890	1.893	...	h	...
		1658.1212	2	1.765	1.771	...	h	...
4 (0.95)	4	1328.8333	0	1.887	1.924	...	2.077	0.010 ($n = 21$)
		1329.0853	1	1.410	1.452	...	1.680	0.025 ($n = 19$)
		1329.1004	1	1.507	1.539	...	1.762	0.029 ($n = 19$)
		1329.1233	1	1.285	1.328	...	1.613	0.024 ($n = 19$)
		1329.5775	2	1.762	1.801	...	1.886	0.023 ($n = 17$)
		1329.6005	2	1.285	1.325	...	1.610	0.046 ($n = 13$)

Table 3—Continued

		Previously Published $\log(f\lambda)$				This Paper		
Mult.	nr. ^a	λ (Å) ^b	ϵ^c	M91 ^d	WFD96 ^e	ZFC97 ^f	$\log(f\lambda)$	MAD ^g
5	1279.8904	1		1.243	1.208	j	1.557	0.022 ($n = 19$)
	1280.1353	0		1.493	1.467	j	1.789	0.024 ($n = 21$)
	1280.3328	2		1.273	1.260	j	1.548	0.036 ($n = 13$)
	1280.4042	1		0.749	0.737	j	1.228	0.083 ($n = 17$)
	1280.5970	1		0.942	0.936	j	1.357	0.032 ($n = 17$)
	1280.8470	2		0.811	0.798	j	1.231	0.058 ($n = 6$)
6	1279.0558	1		-0.026 ^k	-0.026	0.412	0.892	0.078 ($n = 11$)
	1279.2286	2		0.684 ^k	0.684	0.617	1.061	0.035 ($n = 5$)
	1279.4977	2		-0.600 ^k	-0.594	0.063	0.593 ^l	...
7 (0.75)	1277.2454	0		2.091	2.077	j	2.225 ^m	0.019 ($n = 21$)
	1277.2823	1		1.967	1.955	j	2.017 ^m	0.049 ($n = 21$)
	1277.5130	1		1.489	1.455	j	1.703 ^m	0.021 ($n = 19$)
	1277.5496	2		2.016	2.004	j	2.042 ^m	0.042 ($n = 19$)
	1277.7229	2		1.268	1.297	j	1.548 ^m	0.028 ($n = 13$)
	1277.9538	2		0.092	0.019	j	0.593 ^m	0.154 ($n = 1$)

Table 3—Continued

Mult. nr. ^a	λ (Å) ^b	ϵ ^c	Previously Published $\log(f\lambda)$			This Paper	
			M91 ^d	WFD96 ^e	ZFC97 ^f	$\log(f\lambda)$	MAD ^g
7.01 (1.0)	1276.4825	0	0.759	0.758	0.331	1.178	0.041 ($n = 19$)
	1276.7498	1	0.564	0.508	0.485	1.022	0.072 ($n = 12$)
	1277.1901 ⁿ	2	-0.362	-0.468
8.01 (0.85)	1270.1434	0	-0.307	-0.455	-0.265	0.439 ^m	0.061 ($n = 12$)
	1270.4080	1	-1.080	...	-0.582	-0.285 ^m	...
	1270.8439 ⁿ	2	-2.869
9 (0.90)	1260.7355	0	1.696	1.681	j	1.870	0.025 ($n = 21$)
	1260.9266	1	1.219	1.231	j	1.517	0.031 ($n = 18$)
	1260.9962	1	1.094	1.122	j	1.444	0.039 ($n = 18$)
	1261.1223	1	1.316	1.268	j	1.537	0.020 ($n = 18$)
	1261.4257	2	1.094	1.105	j	1.417	0.099 ($n = 12$)
	1261.5519	2	1.571	1.582	j	1.746	0.015 ($n = 16$)
12 (0.40)	1192.2175	0	0.496	-0.004	0.019	0.827	0.065 ($n = 17$)
	1192.4507	1	0.399	0.226	...	0.885	0.078 ($n = 11$)
	1192.8347 ⁿ	2	...	-0.476

Table 3—Continued

Mult. nr. ^a	λ (Å) ^b	ϵ ^c	Previously Published $\log(f\lambda)$			This Paper	
			M91 ^d	WFD96 ^e	ZFC97 ^f	$\log(f\lambda)$	MAD ^g
14 (0.40)	1188.8332 ^o	0	1.299	1.105
	1188.9925	1	0.822	0.736	...	1.156	0.116 ($n = 14$)
	1189.0650	1	0.697	0.664	...	1.138	0.080 ($n = 14$)
	1189.2487	1	0.919	0.529	...	1.041	0.079 ($n = 11$)
	1189.4469	2	0.697	0.602	0.737	1.18 ^l	...
	1189.6307	2	1.174	1.056	1.215	1.42 ^l	...

^aNumbering system of Moore (1998), also adopted by Morton (1991). Numbers in parentheses show the average multipliers that should be applied to the S/N values listed in column 7 of Table 1.

^bValues taken from Morton (1991)

^cFine-structure excitation: 0 = ground state (3P_0), 1 = first excited level (3P_1), and 2 = second excited level (3P_2).

^d (Morton 1991).

^e (Wiese, Fuhr, & Deters 1996).

^f (Zsargó, Federman, & Cardelli 1997).

^gMAD = Median Absolute Deviation [(Mosteller & Tukey 1977), Chap. 10] for results from individual stars that are expected to show a sustained absorption feature with a depth of at least 10%. The number of stars used is given in parentheses. If this number is less than 4, no value for the MAD is given.

^hResults given by Wiese et al (1996) for the f -values of this multiplet were adopted as a standard against which other f -values were compared.

ⁱIn (Morton 1991) there is an incorrect assignment of the excitation energy for this particular transition.

^jIn the paper by Zsargó et al. (1997), the results given by Morton (1991) for the f -values of this multiplet were adopted as a standard against which other f -values were compared.

^kValues taken from erratum (Morton 1992).

^lOnly the spectrum of HD 206267A could be used for this determination.

^mThis transition is seen twice, in different orders. This determination is based on a consolidation of information from both orders.

ⁿThis line is too weak to show up in our spectra.

^oA Cl I transition at 1188.7742 is likely to interfere with this C I line. For this reason, we exclude this line from our analysis.

One could imagine that lines that are from the same level and very close to each other in wavelength, such as those from the excited levels in Multiplet nr. 4, might have larger than usual errors, especially if they are not well resolved from each other because the C I* and C I** features are intrinsically broad. The errors that could arise would be in the relative strengths of the lines within a group, while the sum of f -values for the individual groups should remain accurate.

5.3.2. Misleading Trends Arising from Unresolved, Saturated Substructures?

A striking conclusion that emerges from a comparison of the previous determinations of $\log(f\lambda)$ and our new derivations is that there is a progressive increase in the differences between the two when going from strong to weak transitions. This phenomenon is illustrated in Fig. 3. In view of the smooth and progressive nature of this trend, we must ask the question, “Is this effect real and a consequence of some generalized problem with the previous determinations, or are we being systematically deceived by distortions of the apparent optical depths from one transition to the next?”

In principle, an effect similar to that exhibited in Fig. 3 could arise if the profiles that we observed are really composed of very narrow velocity components that do not overlap each other and are badly saturated for the strong transitions. While the spectrograph has a high wavelength resolving power ($\lambda/\Delta\lambda = 200,000$; see Appendix A), we still expect that many components are well short of being resolved, if we consider the profiles of Na I recorded by Welty, Hobbs & Kulkarni (1994) as representative. As we pointed out earlier (§5.1), when very narrow profiles are badly saturated and unresolved, their apparent optical depths may not accurately reflect the real optical depths, or even a smoothed representation of them. When we compare different transitions, the resulting error will always work in the direction of making strong lines appear to be not as strong as they should be, relative to the weaker ones where the distortions virtually disappear.

Several tests indicate that it is unlikely that we are being deceived by this effect. First, nearly all of the values for the median average deviations in our derived values of $\log(f\lambda)$, when measurable, are below 0.1. Many are well below this value. Variations in the special circumstances for saturated profiles from one star to the next would probably create a more erratic outcome. It is difficult to be quantitatively precise in this conclusion however.

Second, in any given multiplet, the line out of the unexcited level is much stronger than other lines that come from the excited levels (for the most part, simply because there are more carbon atoms in the unexcited level). Since the saturation distortion becomes

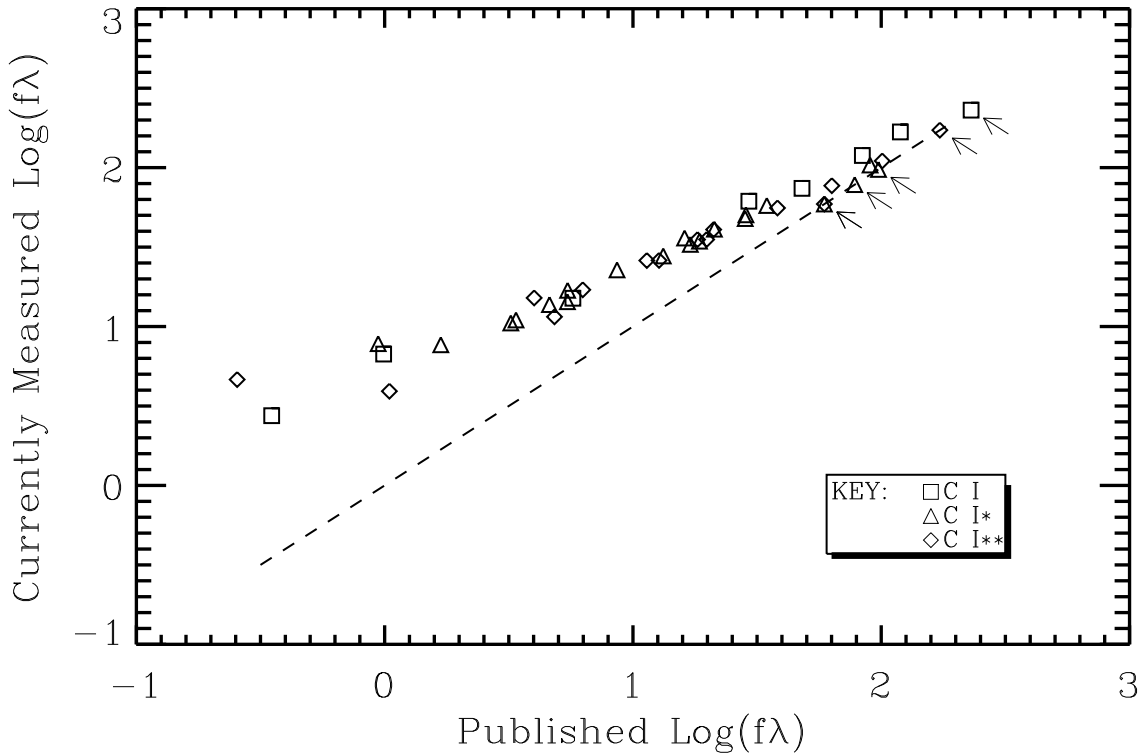


Fig. 3.— A comparison of f -values: each symbol [squares are out of the 3P_0 unexcited level (C I), triangles from the 3P_1 first excited level (C I*), and diamonds from the 3P_2 second excited level (C I**)] has an abscissa corresponding to the value of $\log(f\lambda)$ given by Wiese et al. (1996) and an ordinate equal to our values reported in Table 3. Arrows indicate transitions in Multiplet 2 at 1657 Å, which served as our reference standard and fall on the line of equality (dashed line) by definition. For the probable errors of our determinations, see the discussions at the ends of §§ 5.3.1 and 5.5.2

worse when the lines are stronger, we would expect that the difference trend would be more pronounced for the lines out of the unexcited level than for those out of the excited levels. This appears not to be happening, since the points in Fig. 3 all seem to lie on a common track (as indicated in the caption, different symbols represent transitions out of the three different levels).

Third, as an experiment to probe how sensitive the outcomes for the f -values were to the wavelength resolution of the spectra, we repeated the analyses which derived $N_a(v)$ and the transition strengths, but with the same spectra after they had been artificially degraded by a smoothing operation. The degradation was carried out by convolving the spectra with a Gaussian function that had a width equal to $\sqrt{3}$ times that of the instrumental profile, thus decreasing the net resolution by a factor of 2 from the original recording. Some random differences were seen between the two sets of outcomes for $\log(f\lambda)$ (degraded vs. original), with magnitudes generally of order 0.05 dex or less. In addition, there was a small shift (of order 0.025 dex) of the weaker transitions to even lower values, an effect *opposite* to the one that we would have expected under the hypothesis that the smoothing should make the weak lines look less different from the strong ones. That is, the trend was the reverse of that shown in Fig. 3 (but very much smaller in magnitude), if we plotted the outcomes from the degraded spectrum on the y -axis against the results at full resolution on the x -axis.

A fourth way to sense whether or not our revised strengths for weak C I lines are misguided is to compare one of the lines to a strong line from another, similar element that has a much lower cosmic abundance. A good comparison element is sulfur, since it has a similar first ionization potential to that of carbon (in H I regions, both elements are predominately singly ionized) and, like carbon, sulfur is not heavily depleted. One good pair of lines to consider is made up of the C I line at 1192.218 Å and the S I line at 1295.653 Å. As close as we can determine, both features have nearly identical strengths (and shapes) in the spectra of all stars, except for HD's 3827 and 120086 which do not have enough foreground material to make the lines visible. Since C I and S I are expected to have very similar velocity structures, lines of equal strength should have identical systematic offsets, if they exist, produced by the effects of saturated, unresolved components. As a result, we have confidence that the ratio of column densities should be reflected by the inverse ratio of the lines' values of $f\lambda$.

In the interstellar medium, the abundance of carbon relative to hydrogen is about 1.4×10^{-4} over a broad range of average densities (Hobbs, York, & Oegerle 1982; Cardelli et al. 1991, 1993, 1996; Sofia et al. 1997; Sofia, Fitzpatrick, & Meyer 1998). While one could be critical of these results because they rely on the calculated f -value for one semi-forbidden line at 2325.403 Å, it is reassuring that Sofia et al. (1994) found similar

relative abundances of carbon toward ξ Per and ζ Oph by measuring the damping wings on the allowed transition of C II at 1334.532 Å. The amount of sulfur in the interstellar medium is generally very close to its solar abundance ratio relative to hydrogen, S/H = 1.9×10^{-5} (Federman et al. 1993; Spitzer & Fitzpatrick 1993; Fitzpatrick & Spitzer 1994, 1997; Howk, Savage, & Fabian 1999).

From the above, we conclude that free carbon atoms and ions in the interstellar medium are about 7.5 times as abundant as the sulfur ones. If we multiply this ratio by a correction for the effects of steady-state photoionization and recombination,

$$\frac{n(\text{C I})n(\text{S II})}{n(\text{C II})n(\text{S I})} = \frac{\alpha(\text{C})\Gamma(\text{S})}{\Gamma(\text{C})\alpha(\text{S})} \quad (9)$$

we find the expected $n(\text{C I})/n(\text{S I})$ should range between 16 and 24 for $A_V = 0$ and 1.0, respectively (the variation is caused by alterations in the spectral distribution of the ionizing radiation for different depths inside a cloud). In arriving at this conclusion, we used the photoionization rates calculated by van Dishoeck (1988) and the fitting equations of Shull & van Steenberg (1982) for the recombination rates. We expect that the outcome for Eq. 9 will not change much if we allow for additional recombinations that could arise from collisions with grains or large molecules, since the ratios of the reaction rate coefficients of C and S differ little from $\alpha(\text{C})/\alpha(\text{S})$ (Weingartner & Draine 2001). Dissociative recombination of CH^+ is another channel for producing C I; it is unclear whether or not this might have a stronger influence than its counterpart involving SH^+ or if, for our stars, these channels are at all important relative to the simple recombinations of C and S with free electrons. For the ratio of our value for $f\lambda$ for the C I transition at 1192.218 Å to that of the S I line at 1295.653 Å determined by Federman & Cardelli (1995) [$\log(f\lambda) = 2.052$] we obtain a value of 22, which is approximately midway between the two extremes for the expected ratio of C I to S I densities. Had we instead used the values listed by either Morton (1991), Wiese et al. (1996), or Zsargó et al. (1997), we would have obtained 36, 114 and 108, respectively.

Our fifth and final test makes use of a large survey of K I absorption. Welty & Hobbs (2001) observed features toward HD 206267A and HD 210839 (λ Cep) at a resolution of 0.56 km s^{-1} , i.e., a value about three times better than our STIS observations. Both stars are in our target list and their C I lines resulted in f -values similar to the general determinations listed in Table 3. Of the two, HD 210839 seems to have the narrowest, well-separated components and is thus most likely to manifest any bias that might be caused by our not resolving saturated features. We believe that this star serves as a good test case to examine the behavior of line profiles when they are not fully resolved.

Welty & Hobbs used a profile-fitting analysis, one that takes into account the small amount of their instrumental smearing, to derive component column densities, central

velocities, and velocity dispersions. On theoretical grounds, we expect the profiles of K I and C I to be similar. This expectation is validated by the good tracking of $N(\text{K I})$ to $N(\text{C I})$ over many lines of sight studied by Welty & Hobbs. With these considerations, we felt that it would be instructive to perform a mock evaluation of f -values that duplicated our method discussed in §5.3.1, but using the K I components acting as surrogates for C I. The aim of our mock analysis was to find out what would happen if the previously determined f -values, such as those listed by WFD96, were indeed correct. Would these f -values arise out of the analysis intact, or would the saturation effects mislead us into deriving progressively larger corrections in an upward direction as the lines became weaker, as depicted in Fig. 3?

To answer this question, we undertook the following steps. First, we defined our synthetic C I profiles on a fine velocity grid (0.02 km s^{-1}) such that they adequately sampled the K I components, with their very small b -values (generally ranging from 0.5 to 1.0 km s^{-1}), as listed by Welty & Hobbs. For each component, we estimated the relative proportions of atomic carbon in the three different levels of fine-structure excitation, so that the behavior of each N_a approximately duplicated what we found for HD 210839. While these operations specified the detailed *shapes* of the C I features,⁴ they did not tell us *how much* C I is really present. For the latter, we took the conservative assumption that the *weakest* lines that showed measurable absorption were the only ones that could be trusted (and their real f -values are lower than our determinations), and this forced us to raise our logarithms of the overall outcomes for $N(\text{C I})$, $N(\text{C I}^*)$ and $N(\text{C I}^{**})$ by the amounts 0.80, 0.65 and 0.40 dex, respectively. These enhancements corresponded to the disparities in $\log f\lambda$ between our determinations and those listed by WFD96. With this assumption, we effectively synthesized a case where the weak lines duplicated what we saw with STIS, but strong lines were driven much harder into saturation than what we surmised to be true (and we are testing the proposition that this stronger saturation might not be apparent at our resolution).

Following the definition of the C I, C I* and C I** profiles, we evaluated their detailed optical depths in each multiplet and then smoothed the resulting intensities with the STIS instrumental profile function (a Gaussian function with a width of 1.5 km s^{-1} FWHM was adopted – the smoothed synthetic profiles for weak lines gave an excellent match with the STIS observations). After adding random noise of approximately the same magnitude as in

⁴To obtain a good match with the strongest C I lines observed with STIS, we had to add some low-level, broad components that added some very shallow wings to the main profiles. These wings are below the detection threshold in the K I observations, but they show up well in the much stronger Na I D1 features recorded by Hobbs (1976).

the observations, we analyzed collectively the synthesized profiles from all of the multiplets using the same methods as with the real data. In the end, we obtained values of $\log f\lambda$ that were very close to those that we specified initially (from WFD96), and the results did not show any tendency to drift upward for the weakest lines. The root mean squared deviations from real to calculated values of $\log f\lambda$ equaled 0.06.

To summarize, a broad selection of different tests appears to support our premise that the apparent optical depth comparisons are valid for establishing our upward revisions in weak f -values. This diminishes our concern that we are being systematically misled by unresolved, saturated velocity components.

In their introductory comments that recognize the complexity of the interacting electronic states of C I, Wiese et al. (1996) acknowledge that “...for some multiplets of neutral carbon and nitrogen, sizeable differences remain even between these multiconfiguration results and accurate experimental data.” While this may be true, it is still surprising that for the weakest multiplets there are differences between our findings and the published results that approach nearly one order of magnitude. However for such multiplets there are few opportunities to compare theoretical calculations with experimental determinations; their strengths are usually reported on the basis of theory only.

5.4. Reconstructions of the Profiles

After deriving the three forms of $N_a(v)$ for a given star, we checked that reconstructions of the intensity profiles $\exp[-\tau(i)]$ agreed with the original data $\exp[-\tau_a(i)]$ recorded for each multiplet (see Eqs. 1, 3 and 4). Figure 4 shows such a series of comparisons for λ Cep (HD 210839). This star has enough C I to show absorptions in all of the multiplets covered in the program. One can see that the reconstructions (red traces) agree well with the original data (black traces).

All stars except HD 108 showed excellent correspondences between the original data and the reconstructions. For HD 108, the tracking between the two was inferior to those of the other stars; some limited portions of a few multiplets showed observed absorptions that were stronger than those predicted by the analysis.

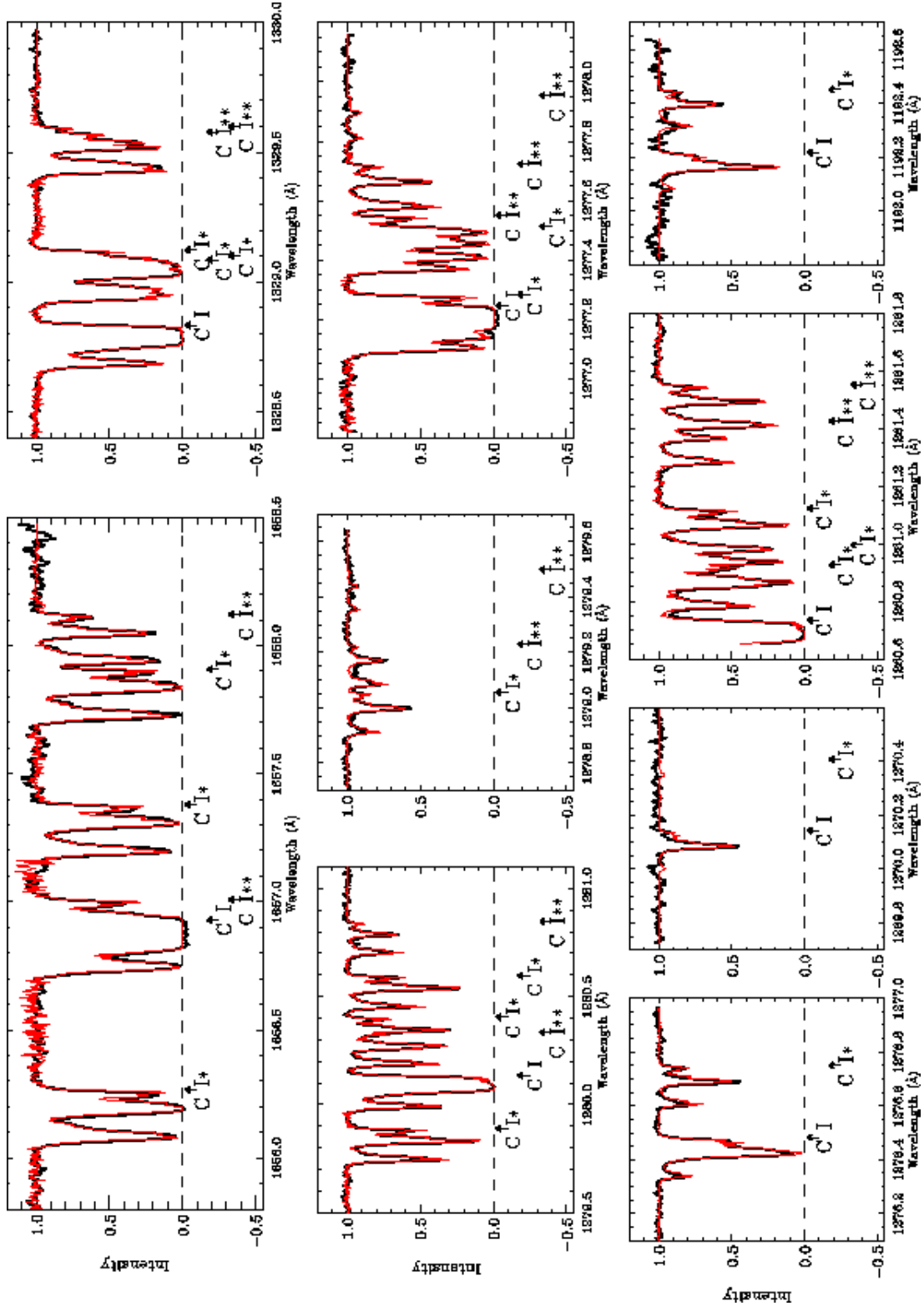


Fig. 4.— A comparison of the original data normalized to a continuum (black traces) for all multiplets in the spectrum of λ Cep (HD 210839) (except for the one at 1189 Å) against reconstructions (overlaid red traces) generated from the derived $X_{k,\epsilon}$ being substituted into Eq. 3 to obtain $\tau(i)$, which in turn gives the intensity through the relation $I(v) = \exp[-\tau(i)]$.

5.5. Errors

5.5.1. Random Errors

The complexities of the calculations and weight factors discussed in §5.2.1 make it difficult to estimate the expected errors for a given set of input spectra, which themselves have varying signal qualities and degrees of influence. Nevertheless, we can sense empirically the random errors in the end results by studying the sizes of the fluctuations in $N_a(v)$ over velocity ranges where we think there is no C I (if C I is present at a level that is below what might be obvious, our error estimate will be too large). Table 4 shows the outcomes for the *rms* deviations away from the zero level for blocks that are 5 km s^{-1} wide. Since random errors may be correlated over small velocity differences, it is probably not safe to conclude that the noise scales in proportion to $\Delta v^{0.5}$ for smaller scales. For scales greater than 5 km s^{-1} , the *random* errors due to noise probably scale in proportion to that expected for independent events, but one must also consider the effects of possible systematic errors discussed below.

Judging from the appearance of the residuals discussed in §5.4, we estimate that in the vicinity of strongest C I features, the estimates for the errors shown in Table 4 should be doubled.

5.5.2. Systematic Errors

We recognize three principal sources of error that might lead to our results being systematically offset from the true values of $N_a(v)$. First, there may be instrumental artifacts that are not accounted for in the analysis, or perhaps done so incorrectly. While errors in the adopted background levels can lead to error, we found that the estimates of these levels by the CALSTIS routines seem to be reasonably accurate. By inspecting the strongest interstellar features that are clearly saturated with flat bottoms, such as C II $\lambda 1334.532$, Si II $\lambda 1304.370$, O I $\lambda 1302.169$, and the triplet of N I at 1200 \AA , we found that the apparent positions of the line bottoms never deviated from zero by more than 3% of the local continuum flux.

One instrumental effect for which we are not making explicit corrections in our analysis is the existence of broad halos that are a part of the point-spread functions of the Far- and Near-UV MAMA detectors in STIS (Leitherer 2000, pp. 128–129). The most pronounced effects of the halos are to alter the background levels and slightly degrade the resolution. However, since the bottoms of saturated lines appear to be near zero, as we stated above, it

Table 4. Observed Random Deviations^a in Column Density

HD	$\sigma[N(\text{C I})]$ (10^{12}cm^{-2})	$\sigma[N(\text{C I}^*)]$ (10^{12}cm^{-2})	$\sigma[N(\text{C I}^{**})]$ (10^{12}cm^{-2})	Number of Samples
108	0.64	1.31	2.17	12
3827	0.36	0.53	0.46	15
15137	0.68	0.80	0.72	17
69106	0.63	0.58	0.38	15
88115	0.43	0.93	0.68	14
93843	0.50	0.82	1.25	13
94493	0.49	0.93	1.03	16
99857A	0.43	0.84	0.91	13
103779	0.49	0.70	0.70	14
106343	0.45	0.60	0.69	16
109399	0.50	1.34	0.49	13
116781A	0.61	0.74	0.93	15
120086	0.32	0.39	0.38	22
122879	0.22	0.65	0.86	15
124314A	0.42	0.85	0.65	16
203374A	0.43	0.64	0.45	17
206267A	0.58	0.68	0.52	17
208947	0.30	0.48	0.46	18
209339A	0.39	0.69	0.81	18
210839	0.55	0.91	0.62	16
224151	0.27	0.70	0.45	11

^aEvaluations of $\left\{\sum_n [\int N_a(v)dv]^2 / n\right\}^{0.5}$, where the integration intervals are over contiguous series of 5 km s^{-1} wide blocks outside the velocity ranges shown in Figs. 6 and 7, i.e., where we expect there to be no C I. Note that these are not *rms* deviations about a mean value of the samples with a correction of $(n/n - 1)^{0.5}$ to obtain a population dispersion; they are simply the *rms* deviations about a zero value. The number n of blocks is shown in the last column of the table.

is clear that the background corrections of CALSTIS include the effects of the halos. As for degradation of the resolution, it is clear from our findings reported in Appendix A that any such degradation must be very small.

The second error source that could be coherent over large velocity ranges is a deviation between our adopted continuum level and the correct one. Our choice of stars with large projected rotational velocities (see col. 4 in Table 1) generally insured that the continuum levels do not have sharp and unpredictable curves caused by stellar features. For most stars, the continuum curvatures were inconsequential, as is evident in Fig. 1 for HD 210839, which made the continuum levels very easy to define. Nevertheless, in a few cases for stars with lower values of $v \sin i$ the levels showed undulations. The worst example was HD 106343 in the vicinity of 1277 Å. Here, stellar features had a depth of about 50% and a width of 0.5 Å FWHM. This single star is unlikely to have much impact on the final results.

Finally, for our third type of error we must consider the possibility that some or most of our f -values are incorrect, despite our best efforts to try to uncover evidence that we were being misled, as discussed in §5.3.2. While we had chosen the 1657 Å multiplet as our standard because we believed it to have the most reliable f -value determinations, this multiplet is one of our worst ones for giving clear, unambiguous signals – see the relative S/N values in Table 3 (number in parentheses below the multiplet numbers in col. 1). Upon inspection of the points in Fig. 3, one might propose that other lines with strengths that are about the same as the ones that we adopted as standards might have been better choices. If that is correct, then all values of $\log f\lambda$ other than the ones belonging to the 1657 Å multiplet should be reduced by about 0.1 dex. The effect of this would be to revise all of the values of $N_a(v)$ (for all three of the fine-structure levels) upward by 0.1 dex, except for the weakest wings of the lines that are primarily defined by the strongest multiplet.

6. Results

6.1. General Remarks

The ultimate product from the analysis of all of the multiplets described in §5.2 is a synthesis of the functional forms $N_a(v)$ for each of the three fine-structure levels of C I. The upper two levels are primarily populated by collisions with other particles, a process that competes with radiative de-excitations. Our main objective is to compare the populations in each level, so that we can learn about the local temperature and density of the C I-bearing material.

Early studies of the C I excitation from observations with the *Copernicus* satellite

indicated population ratios that were sometimes inconsistent with the expected conditions for any given local density and temperature (Snow 1976; Drake & Pottasch 1977; Frisch 1980). It was evident that the results had to be interpreted in terms of a superposition of contributions from regions with different physical conditions. Much of this overlap will be overcome by the ability of the STIS spectrum to show small differences in Doppler shifts. Nevertheless, we must still be prepared to handle cases where there are superpositions of absorptions arising from regions with different excitation conditions, but with nearly the same radial velocity.

To understand what combinations of conditions can create these composite level populations, it is useful to express the measurements at a given velocity in the form of two quantities, $f_1 \equiv N(\text{C I}^*)/N(\text{C I}_{\text{total}})$ and $f_2 \equiv N(\text{C I}^{**})/N(\text{C I}_{\text{total}})$.⁵ For a simple introduction on how these quantities behave under different conditions, we show in Figure 5 the expected outcomes for f_1 and f_2 for C I embedded within neutral hydrogen clouds having a single value for the temperature, but with various internal densities $n(\text{H})$. As the density increases from a low value where collisional excitations are infrequent to much higher densities where the level populations can become appreciable, the (f_1, f_2) points advance along the curve from the lower left to the upper right in the diagram.

With regard to superpositions, the $f_1 - f_2$ representation has a useful geometrical property that was exploited in an early study of C I excitation by Jenkins & Shaya (1979). Specifically, they pointed out that the outcome for a composite measurement on a diagram of f_2 versus f_1 equals the “center of mass” of points that would be plotted for the individual contributors, with “weights” assigned in proportion to the respective local abundances of C I_{total}. This concept is illustrated in Fig. 5: an observed outcome at (0.23, 0.10) may arise from C I within a large amount of material having $n(\text{H}) = 10^{1.4} \text{ cm}^{-3}$ which is then superposed on a contribution from a gas that has a smaller column density of C I but is considerably more dense, i.e., $n(\text{H}) = 10^{3.2} \text{ cm}^{-3}$. Of course, this interpretation is not unique – many other possible combinations of contributions along the curve can produce the same result. The usefulness of this important theorem on composite measurements has been reflected by the adoption of the representation of f_2 vs. f_1 in many subsequent studies of C I (Jenkins et al. 1981, 1998; Jenkins, Jura, & Loewenstein 1983; Smith, et al. 1991; Jenkins & Wallerstein 1995).

⁵In all quantitative statements and formulae in this article, C I always denotes atomic carbon in the lowest fine-structure level *only*, while C I_{total} refers to all of the atomic carbon, irrespective of its fine-structure excitation.

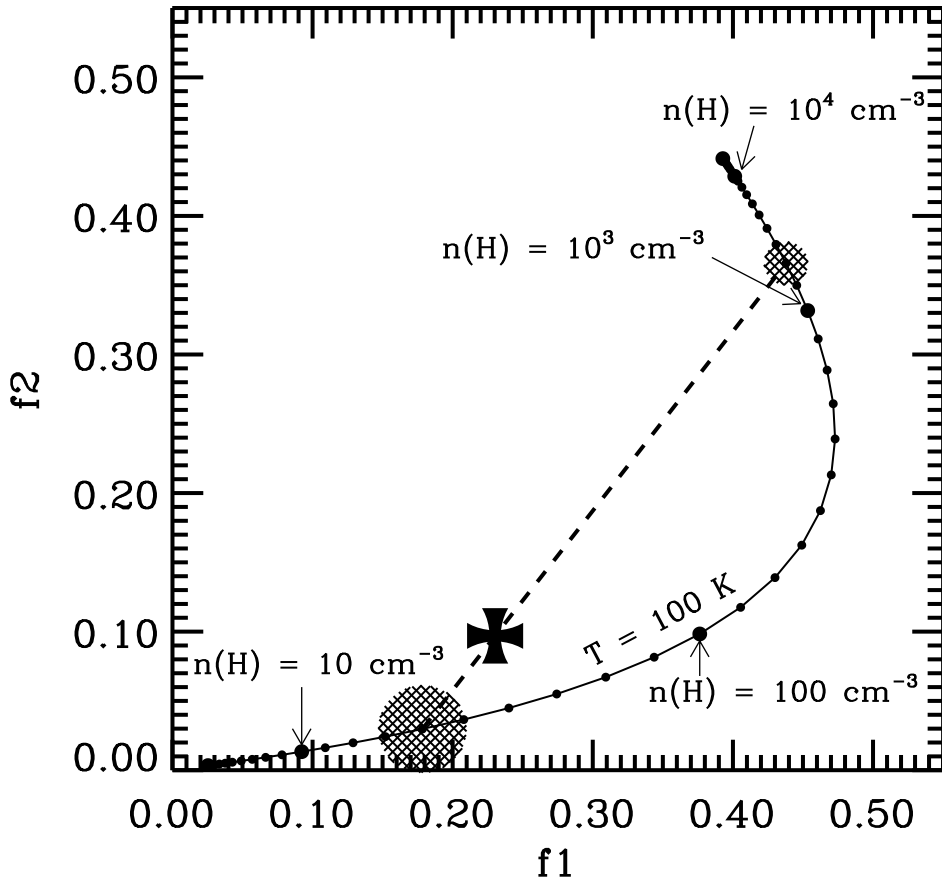


Fig. 5.— Expected outcomes for $f1 \equiv N(\text{C I}^*)/N(\text{C I}_{\text{total}})$ and $f2 \equiv N(\text{C I}^{**})/N(\text{C I}_{\text{total}})$ for absorption by C I-bearing gases at various densities $n(\text{H})$ and a single temperature $T = 100 \text{ K}$. An observed result at $f1 = 0.23$ and $f2 = 0.10$ (at the Maltese cross) may arise from the superposition of contributions from a thick cloud with a low density $n(\text{H}) = 10^{1.4} \text{ cm}^{-3}$ (large, circular cross-hatched region) and a thin cloud with $n(\text{H}) = 10^{3.2} \text{ cm}^{-3}$ (smaller cross-hatched region). This position in the diagram corresponds to the “center of mass” of the C I-weighted combinations that lie on the track representing homogeneous regions.

6.2. Theoretical Expectations for f_1 and f_2

6.2.1. Collisional Excitation

To interpret our measurements of f_1 and f_2 in terms of useful properties of the gas which produces the C I absorptions, we must compute the loci of points on the diagram for a variety of physical and chemical states. In presentations that compare the expected outcomes with the observations, to be discussed in §6.3, we chose to exemplify three fundamental regimes: Case 1 – neutral hydrogen at various temperatures ($20 < T < 160$ K) and densities, but with negligible fractional concentrations of molecules, electrons and protons, Case 2 – gas with all of the hydrogen in molecular form at a typical kinetic temperature $T = 78$ K, one that results in a rotational excitation such that $N_{J=0} = N_{J=1}$ (again with negligible ionization), and Case 3 – fully ionized gas with $T = 7000$ K, as might be found in a star’s H II region. In all cases, we assumed an abundance ratio He/H = 0.0975 (Anders & Grevesse 1989), and that He is neutral in all of the C I-bearing zone of the H II region that applies to Case 3. Table 5 summarizes the relative partial pressures in the three cases.

Table 5: Relative Partial Pressures

Constituent	Case 1	Case 2	Case 3
ortho-H ₂	0.00	0.418	0.00
para-H ₂	0.00	0.418	0.00
H I	0.911	0.00	0.00
He I	0.0888	0.163	0.0465
e	0.00	0.00	0.477
p	0.00	0.00	0.477

One can see from the results tabulated by Keenan (1989) that for Case 1 (neutral atomic gas) excitations caused by the low concentrations of electrons arising from the photoionization of carbon and other species that can be ionized in H I regions should be unimportant. For situations that might call for Case 2, we expect that regions that we are investigating should not have all of the hydrogen in molecular form. Nevertheless, we find that we can regard the precise value of any intermediate molecular fraction as an irrelevant parameter because the outcomes for Case 2 are so similar to those from Case 1, as we will demonstrate shortly. The relevance of Case 3 will be addressed in a later section (§7.3). Generally, the three cases span a useful range of expected conditions in C I-bearing gas clouds, and one can imagine what the consequences would be for intermediate states.

For the excitation and de-excitation of the C I fine-structure levels, we adopted rate

coefficients from the following sources: Launay & Roueff (1977) for atomic hydrogen, Schröder et al (1991) for molecular hydrogen in the ortho and para states, Staemmler & Flower (1991) for neutral helium (with an extrapolation for $T > 150$ K), Johnson et al. (1987) for electrons, and Roueff & Le Bourlot (1990) for protons. For the radiative decay rates of the upper levels, we used the values given by Froese Fischer & Saha (1985). The equilibrium concentrations of the excited levels relative to the ground state are given by

$$\frac{n(\text{C I}^*)}{n(\text{C I})} = \frac{k_{0,1}(k_{2,1} + k_{2,0} + A_{2,1} + A_{2,0}) + k_{0,2}(k_{2,1} + A_{2,1})}{k_{1,2}(k_{2,0} + A_{2,0}) + (k_{1,0} + A_{1,0})(k_{2,0} + k_{2,1} + A_{2,1} + A_{2,0})} \quad (10)$$

and

$$\frac{n(\text{C I}^{**})}{n(\text{C I})} = \frac{k_{0,2}(k_{1,0} + A_{1,0} + k_{1,2}) + k_{1,2}k_{0,1}}{(k_{1,0} + A_{1,0})(k_{2,0} + k_{2,1} + A_{2,1} + A_{2,0}) + k_{1,2}(k_{2,0} + A_{2,0})} \quad (11)$$

where the indices 0, 1 and 2 refer to C I, C I* and C I**, respectively, and $k_{m,n}$ are the collision rates from state m to state n summed in proportion to the concentrations of the projectile species that are present. The reverse reaction rates $k_{n,m}$ are related to the forward ones $k_{m,n}$ through the principle of detailed balancing. The radiative decay rates $A_{2,1}$ and $A_{1,0}$ are the two quantities in the equations that are independent of density and temperature, thereby giving us the leverage to determine the physical conditions for the C I-bearing gas ($A_{2,0}$ is so small compared to the other two decay rates that it can be neglected).

6.2.2. Optical Pumping

In addition to the effects from collisions, C I can be excited through optical pumping, principally by ultraviolet photons from stars. We have adopted the rates computed by Jenkins & Shaya (1979) for the general ISM, but used 10 times these rates for the H II region, i.e., Case (3), on the grounds that the stellar radiation field would be substantially elevated. For all cases, the pumping rates are simply added to the appropriate collision rates.

Figure 6 of Jenkins & Shaya (1979) illustrates how the tracks in the $f_1 - f_2$ diagram are changed when the pumping rates are raised from one to ten times the average rate. For thermal pressures substantially less than about $p/k = 10^4 \text{ cm}^{-3}\text{K}$, enhancements in the optical pumping rate may create considerable elevations in f_1 , accompanied by smaller changes in f_2 . For example, when the pumping is at a level equal to ten times the average rate and there are no collisional excitations, $f_1 = 0.13$ and $f_2 = 0.02$. The tracks for various collisional excitation conditions all emanate from this displaced origin, but the upward

shifts in f_1 and f_2 become smaller as the pressures increase. When $p/k \gtrsim 10^4 \text{ cm}^{-3}\text{K}$, the values of f_1 and f_2 are virtually unchanged.

Pumping by the general background of line radiation emitted by other excited C I atoms in the Galaxy (see §7.1) should be negligible. If the average emission intensity of $6.4 \times 10^{-8} \text{ erg cm}^{-2}\text{s}^{-1}\text{sr}^{-1}$ at $609 \mu\text{m}$ recorded by Wright et al. (1991) for the Galactic plane is assumed to fill a solid angle in the sky of about $2\pi \text{ sr}$ and is spread over a range of Doppler velocities equal to 100 km s^{-1} (making $\Delta\nu = 1.64 \times 10^8 \text{ Hz}$), we conclude that $U_\nu = 8.2 \times 10^{-26} \text{ erg cm}^{-3}\text{Hz}^{-1}$ and calculate an excitation rate

$$U_\nu B_{0,1} = \frac{g_1 U_\nu c^3 A_{1,0}}{8\pi g_0 h \nu^3} = 2.4 \times 10^{-11} \text{ s}^{-1} \quad (12)$$

which is smaller than $A_{1,0}$ by a factor of 3000. A similar conclusion holds for the $J = 2 \rightarrow 1$ radiation at $370 \mu\text{m}$. The measured average radiation field at $370 \mu\text{m}$ is $1.16 \times 10^{-7} \text{ erg cm}^{-2}\text{s}^{-1}\text{sr}^{-1}$.⁶ With the same assumptions as before, we find that $U_\nu B_{1,2} = 1.1 \times 10^{-11} \text{ s}^{-1}$ which is lower than $A_{2,1}$ by a factor of 2.2×10^4 .

Next, we consider the consequences of the carbon atoms being in the vicinity of, or in fact right next to, a bright H II region that is emitting the submillimeter line radiation by other carbon atoms inside of it (or perhaps associated with its photon-dominated, dense, neutral gas just outside). If the brightness temperature of the $609 \mu\text{m}$ $J = 1 \rightarrow 0$ line radiation is 1 K , then the corresponding intensity $B_\nu = 2kT\lambda^{-2} = 7.4 \times 10^{-14} \text{ erg cm}^{-2}\text{s}^{-1}\text{Hz}^{-1}\text{sr}^{-1}$ should give an excitation rate $2\pi B_\nu B_{0,1}/c = 4.6 \times 10^{-9} \text{ s}^{-1}$, i.e., about 6% of the value of $A_{2,1}$, if indeed the region that emits the C I fine-structure radiation subtends $2\pi \text{ sr}$ in the sky. Peak brightness temperatures of about 2.4 K (with a dispersion of 1.8 K) have been recorded for bright, southern-hemisphere H II regions by Huang et al (1999) using the AST/RO telescope. Hence, the pumping rate right next to one of these regions would be about $1.1 \times 10^{-8} \text{ s}^{-1}$. We do not know the strength of the corresponding radiation for $J = 2 \rightarrow 1$, but if we assume that the C I** associated with the H II region has, at worst, a population ratio equal to the ratio of statistical weights, $g_2/g_1 = 5/3$, then the $1 \rightarrow 2$ pumping rate just outside the region could be as high as $2.4 \times 10^{-8} \text{ s}^{-1}$ if $T_B = 2.4 \text{ K}$ for the peak emission of the $609 \mu\text{m}$ line. The two pumping rates discussed above are about equivalent to 15 and 33 times the average optical pumping rates for $0 \rightarrow 1$ and $1 \rightarrow 2$, respectively, estimated for the Galactic plane (away from bright, O-B associations). They do, of course, assume the worst possible case, i.e., that the C I that we are examining is right next to the region and has a radial velocity that exactly matches that of the emission

⁶This value is likely to be an overstatement of the true flux, since the COBE FIRAS spectrometer is unable to resolve the $370 \mu\text{m}$ radiation from CO 7–6 emission at $369 \mu\text{m}$ (Fixsen, Bennett, & Mather 1999).

profile’s peak. It should be clear that even with some relaxation of these optimal conditions, the pumping rates are not entirely trivial. Nevertheless, we point out that most locations on any line of sight will not be affected by this problem.

6.3. Presentations

The key results of our investigations are presented in Figures 6 and 7. The tall panel on the left-hand side of Figure 6 depicts the outcome from our derivations of $N_a(v)$ for C I, C I* and C I** for the star HD 210839 (λ Cep). The upper bound (thin black line) of the colored region indicates $N_a(v)$ for C I_{total}, while the thick blue, yellow and red traces apply to C I, C I* and C I**, respectively. (The latter two quantities are magnified vertically by a factor of 2 to make them easier to discern.) The colors inside the profile for C I_{total} identify different zones in radial velocity which are keyed to identical colors in the points which show f_1 and f_2 in the panels on the right-hand side of the figure. At the top of the panel showing the profiles, we indicate the origin for the velocity scale for the Local Standard of Rest (LSR) and the calculated heliocentric radial velocity caused by differential galactic rotation at the position of the star (see cols. 5 and 6 of Table 2). Quiescent gas along a line of sight must be situated between these two markers. Parts of the profiles outside the markers must arise from gases with peculiar velocities for their locations – we will address this issue later (§7.5).

It is clear from our profiles for HD 210839, as well as nearly all of the other stars in the survey, that we are able to derive f_1, f_2 pairs for many different radial velocities. This is best done by integrating the relevant $N_a(v)$ ’s over finite velocity intervals, taking care that the widths of these intervals are not so small that the results are dominated by noise. At the same time, we wish not to make the intervals so large that we lose potentially useful distinctions of behavior at different velocities. As a good compromise, we chose to define the boundaries for the velocity bins in terms of having a constant $N_a(v)$ for C I_{total} inside them. For all stars except HD’s 3827, 120086 and 206267A (see labels in the f_1, f_2 panels of Figs. 7a, g and i), we chose these intervals to enclose $\Delta N_a(v) = 1.0 \times 10^{13} \text{ cm}^{-2}$. In essence, the intervals have varying widths: they are broad when $N_a(v)$ is low, and they become narrow within the tallest portions of the peaks in $N_a(v)$. They are indicated on the velocity plot as histogram-style bars for the colored regions. These bars are not easy to recognize for HD 210839 in Fig. 6 because they are so narrow, but they are prominent for stars with much lower column densities of C I shown in Figs. 7a, c and d, such as HD’s 3827, 88115, 93843, 94493, etc. The very small amount of C I toward HD 120086 represents an extreme case of coarse velocity intervals; we had to reduce $\Delta N_a(v)$ to $2.5 \times 10^{12} \text{ cm}^{-2}$ to

give some level of differentiation for different velocities. As a consequence, the errors for these points are relatively large.

The lower right panel of Fig. 6 shows the values of f_2 plotted against their respective values of f_1 with colors that match the appropriate velocity-interval bands in the plot of $N_a(v)$. An expanded version of this plot is shown on the upper right portion of the figure. We have refrained from showing error bars for the values of f_1 and f_2 , to avoid confusion. One can judge the uncertainties from random errors by examining the sizes of the fluctuations relative to the signals in $N_a(v)$ at the appropriate matching velocities (indicated by colors). In the plots of f_2 vs. f_1 , the black traces illustrate the computed values of these variables for Case 1 (neutral atomic gas – see §6.2) for the temperatures labeled at the end points. Different thermal gas pressures along these tracks are indicated by points with a spacing $\Delta \log(p/k) = 0.1$. Numbers with circles around them show the positions and values of points having integer $\log(p/k)$. The green and red traces represent Cases 2 (pure hydrogen molecules) and 3 (fully ionized hydrogen with an enhanced pumping field), respectively.

Plots of $N_a(v)$ and f_1 vs. f_2 for the remaining stars in the survey are shown in Fig. 7. The velocity scales and ranges of f_1 and f_2 change from one star to the next, to accommodate for the differences in the outcomes. However to avoid confusing distortions, the aspect ratio of the plots of f_1 and f_2 remain unchanged: in all cases the range for f_2 is half that for f_1 , although the overall magnification may change from one plot to the next. Column densities integrated over the entire velocity ranges shown in the plots are listed (in logarithmic form) in Table 6.

Some of the derived combinations of f_1 and f_2 yielded results that fall outside the region in the diagram bounded by the outermost theoretical curves on the right-hand side and a line running from the origin to the point $(0.33, 0.56)$ that corresponds to infinite temperature and density (i.e., where the population ratios assume values simply in proportion to the statistical weights of the levels). These combinations are clearly inadmissible within the framework of the “center of mass” construction for blended contributions discussed in §6.1. In all instances where this happened, as shown by the outliers in the f_1, f_2 diagrams of Fig. 7, the samples were drawn from velocity ranges where $N_a(v)$ was small. Under our scheme of always sampling a given value of $\Delta N_a(v)$, we had to make the intervals of integration over velocity quite large, and this led to our exposing the measurements to random and systematic errors (§5.5) that were significantly greater than the rest of the samples.

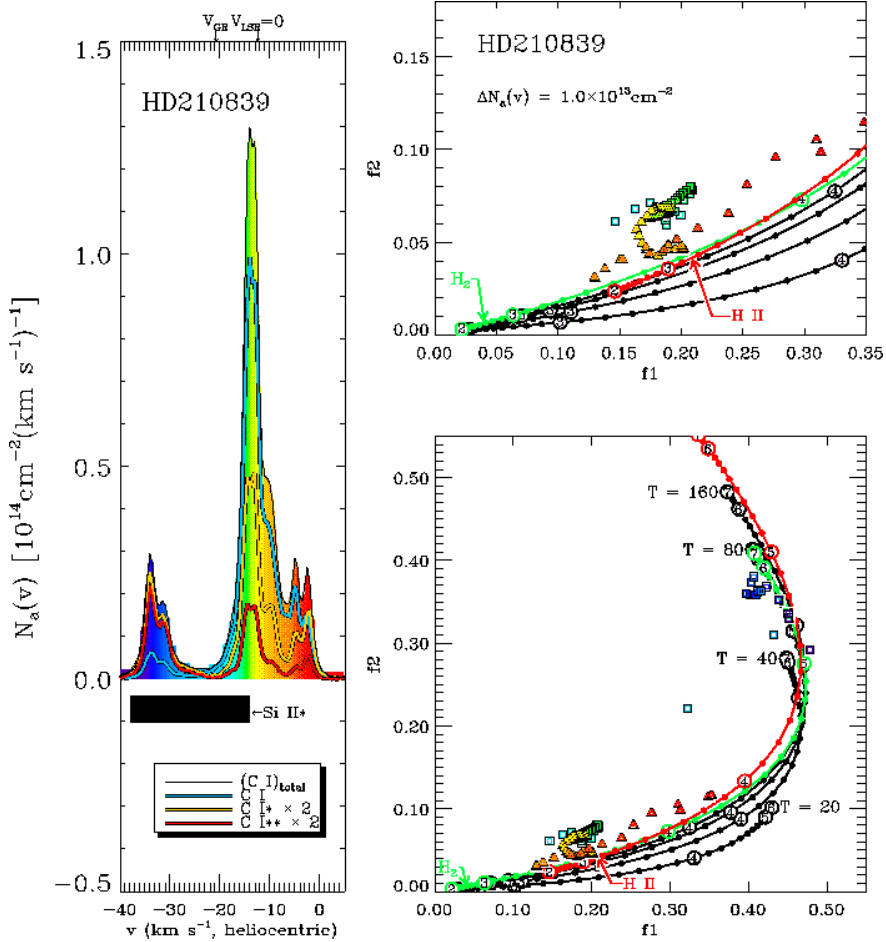


Fig. 6.— *Left panel:* $N_a(v)$ for C I, C I* and C I** (shown with colored lines as indicated in the key) for the star HD 210839 (λ Cep), with the velocity region containing perceptible Si II* absorption that might mark dense H II regions (see §7.3) indicated by a solid, black, horizontal bar. The zero-point for the LSR velocity scale $v_{\text{LSR}} = 0$ and the expected radial velocity from differential galactic rotation at the star's position v_{GR} are indicated at the top. *Right panels:* The values of f_2 plotted against f_1 , as defined in §6.1, with colors that match the indicated velocity regions in the plot of $N_a(v)$. Triangular points come from C I outside the Si II* velocity region, while box-like points come from inside this interval. The tracks with solid, round points on them represent the theoretically expected loci for homogeneous regions at various temperatures (as labeled) and thermal pressures (logarithmic values for the units cm^{-3}K as indicated by integers within the large markers, with minor markers between them which are 0.1 dex apart) for Cases 1 (neutral, atomic gas: black), 2 (neutral molecular gas: green) and 3 (gas with all of the hydrogen fully ionized: red) – see §6.2.

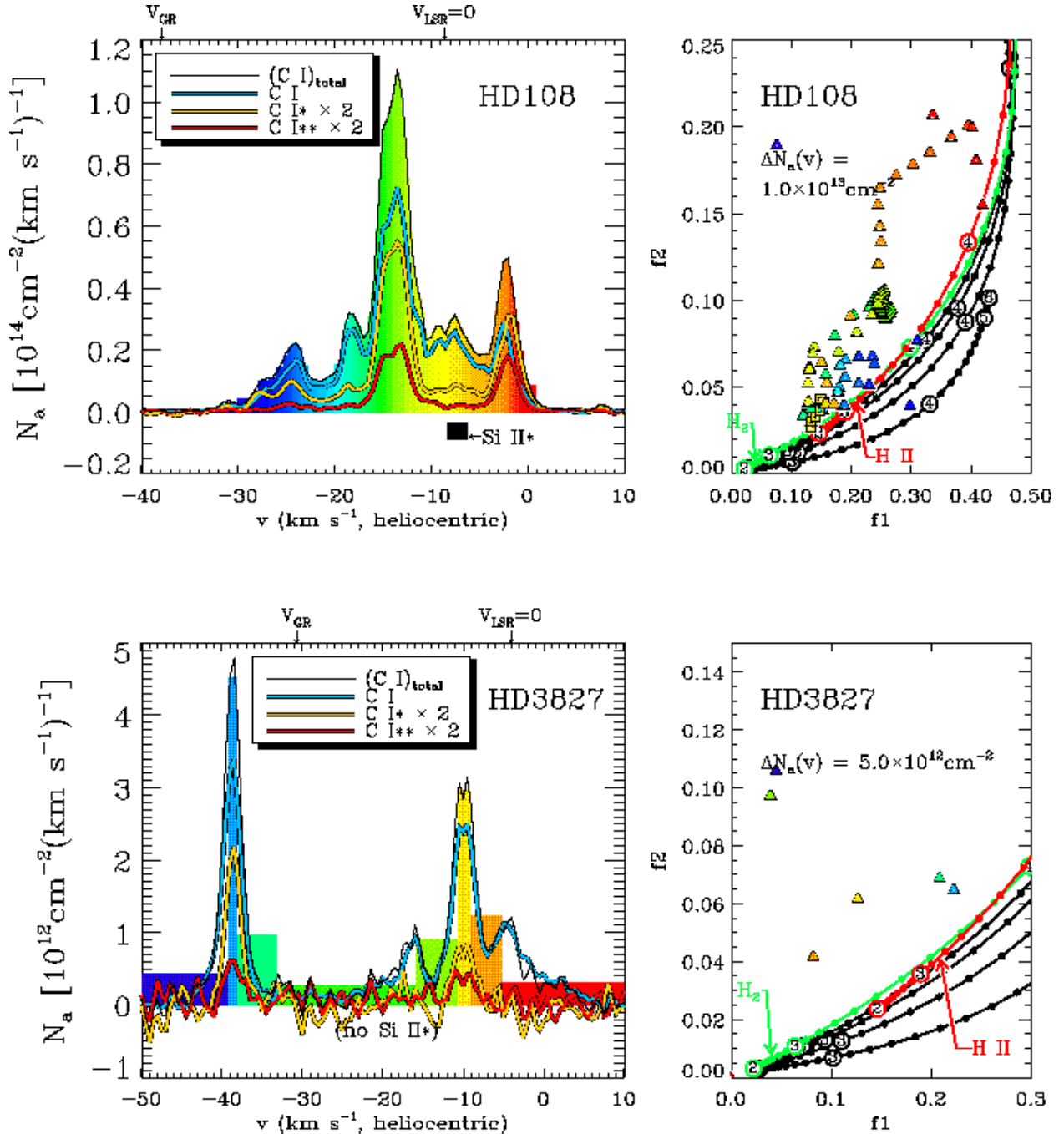


Fig. 7a.— Information on $N_a(v)$ (left panel) and f_2 vs. f_1 (right panel) for stars in the survey, presented in the same style as for HD 210839 in Fig. 6. See the caption for Fig. 6 and the text (§6.3) for details.

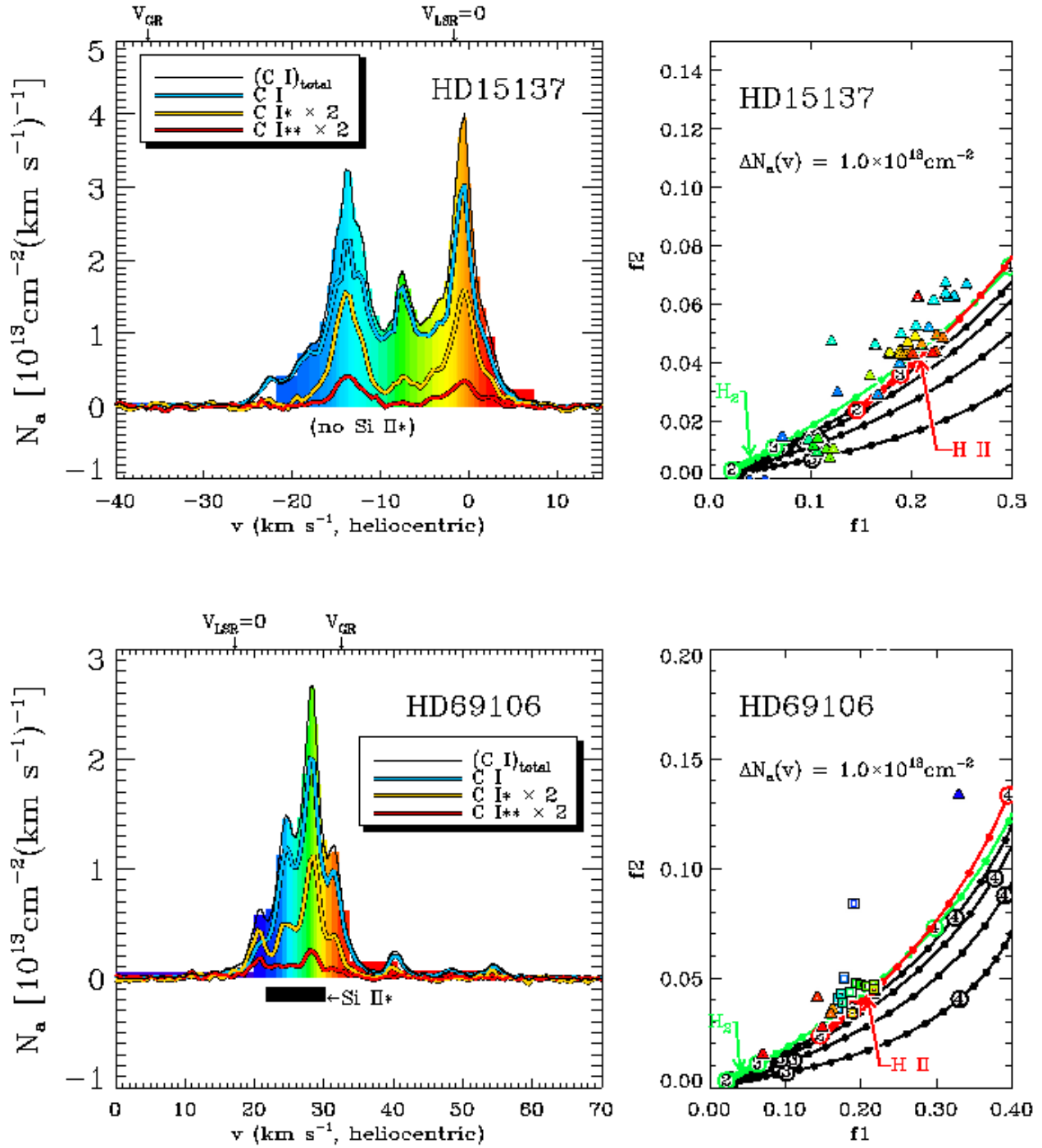


Fig. 7b.— continued

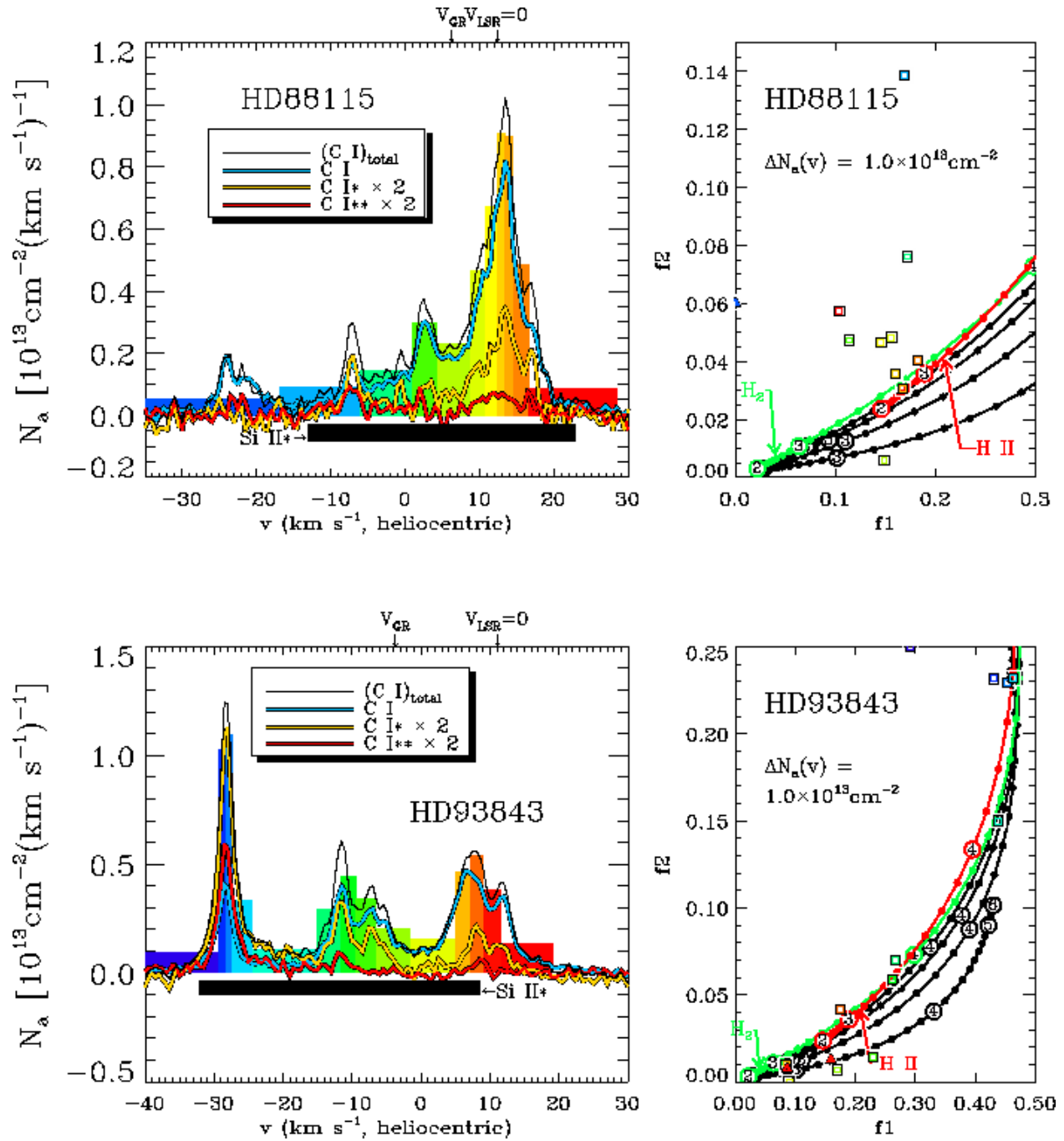


Fig. 7c.— continued

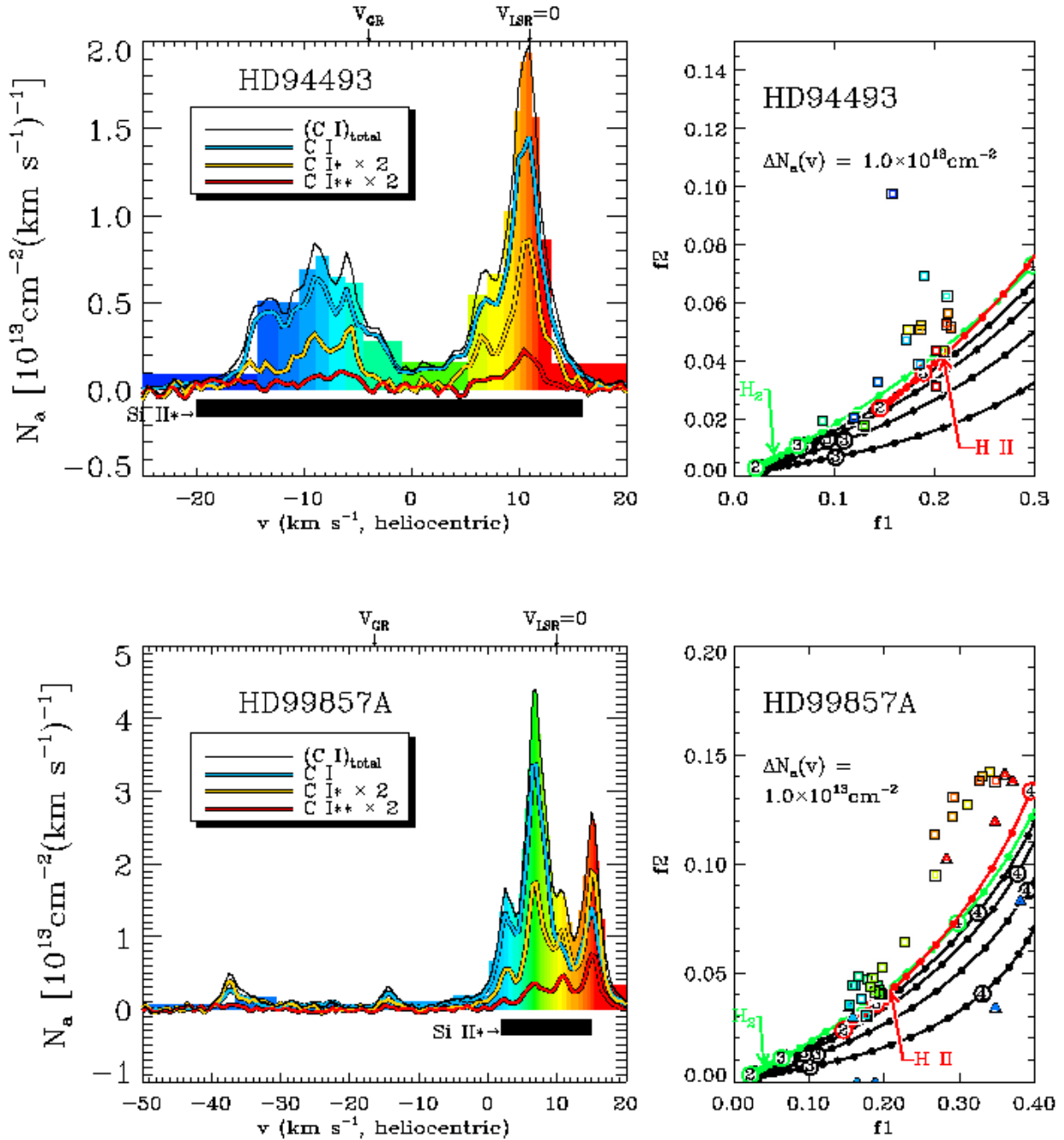


Fig. 7d.— continued

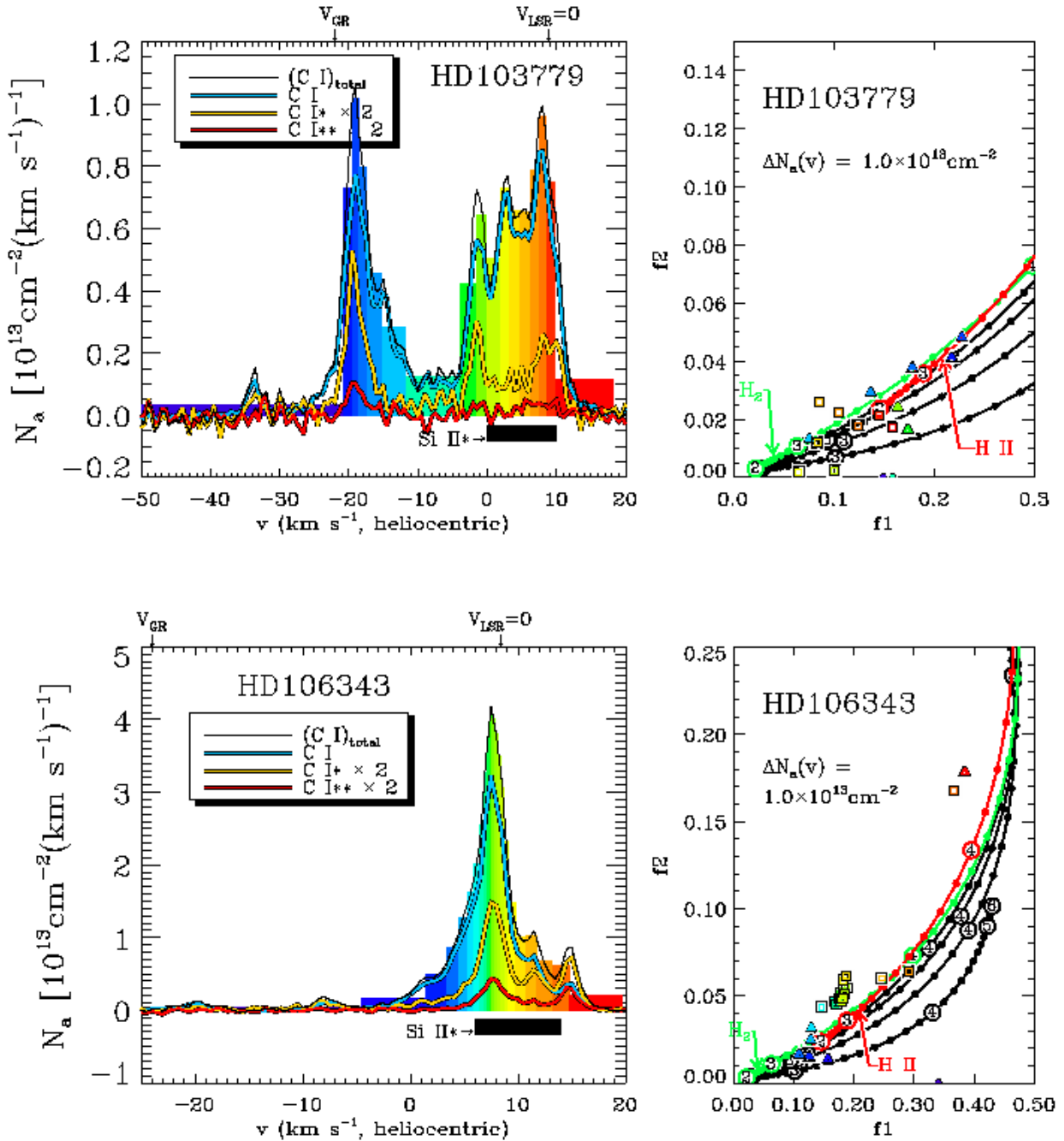


Fig. 7e.— continued

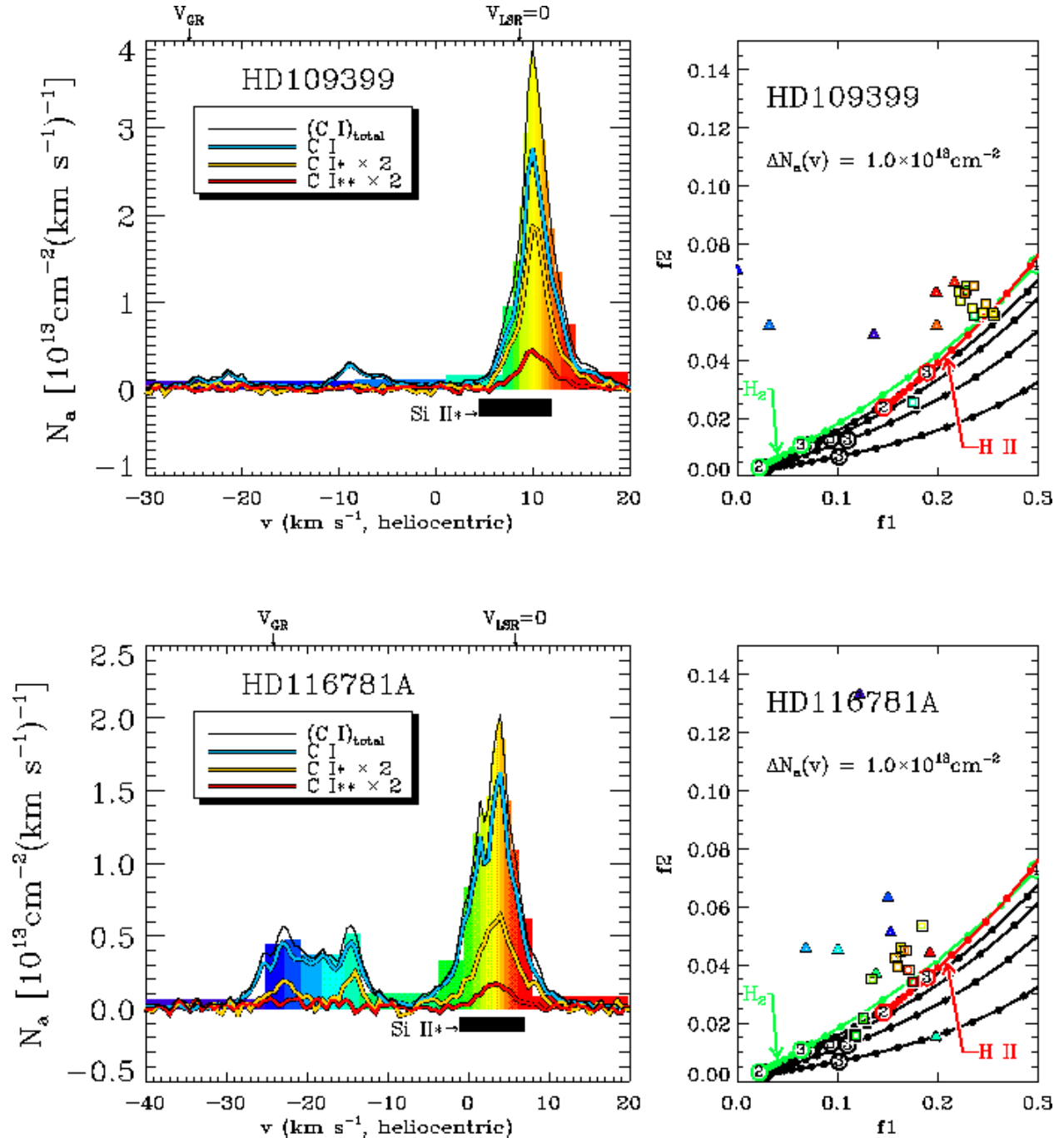


Fig. 7f.— continued

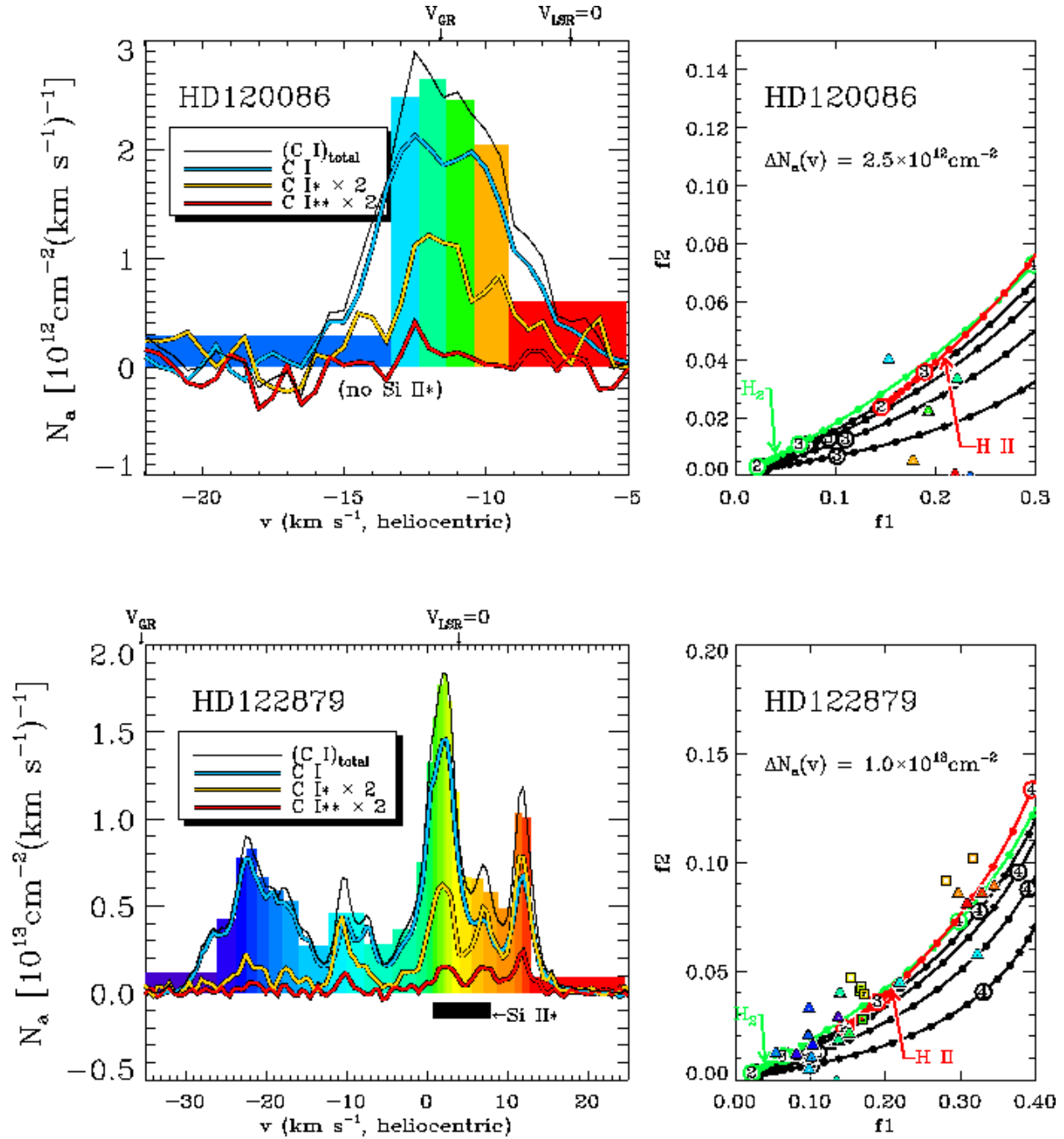


Fig. 7g.— continued

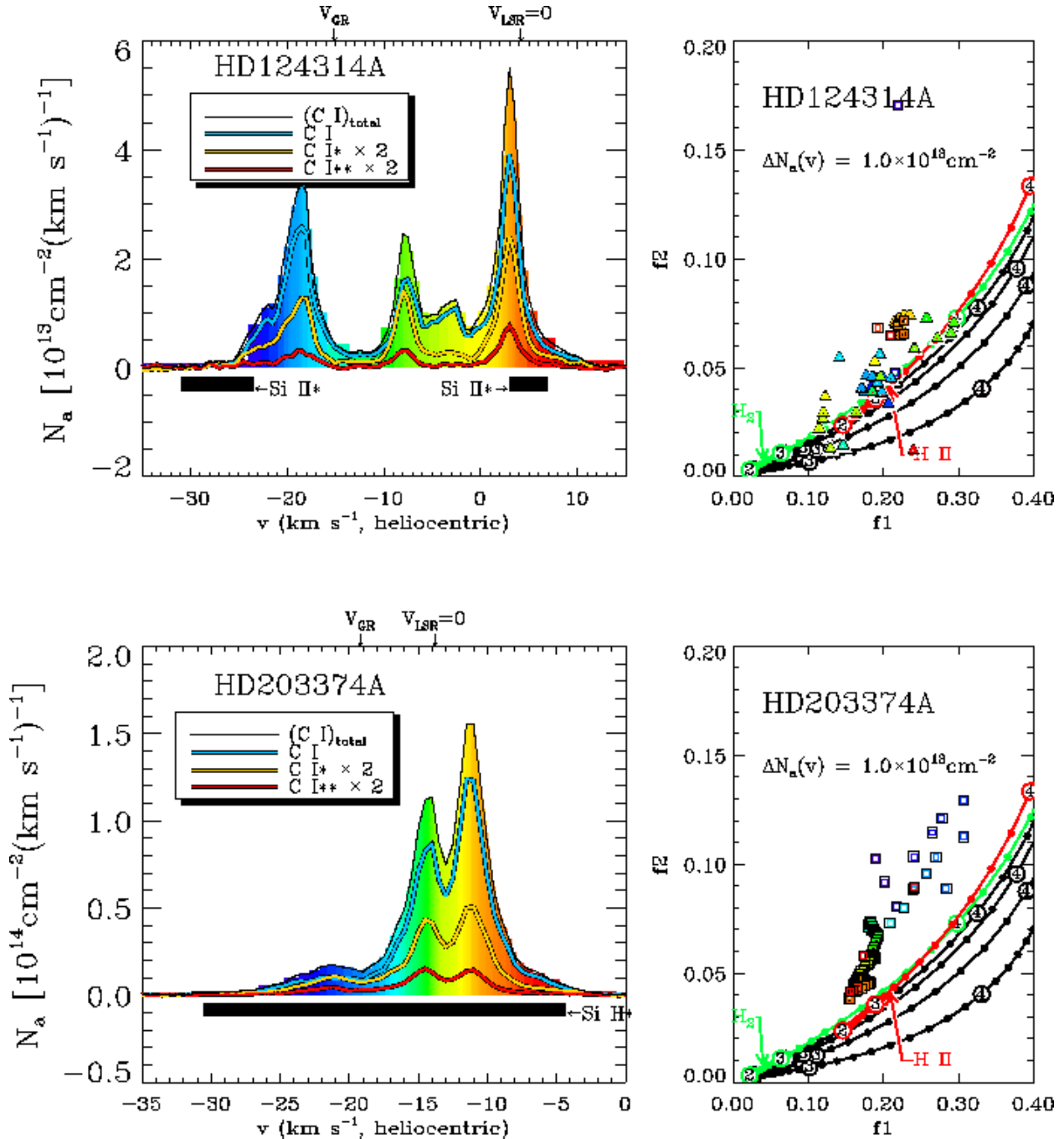


Fig. 7h.— continued

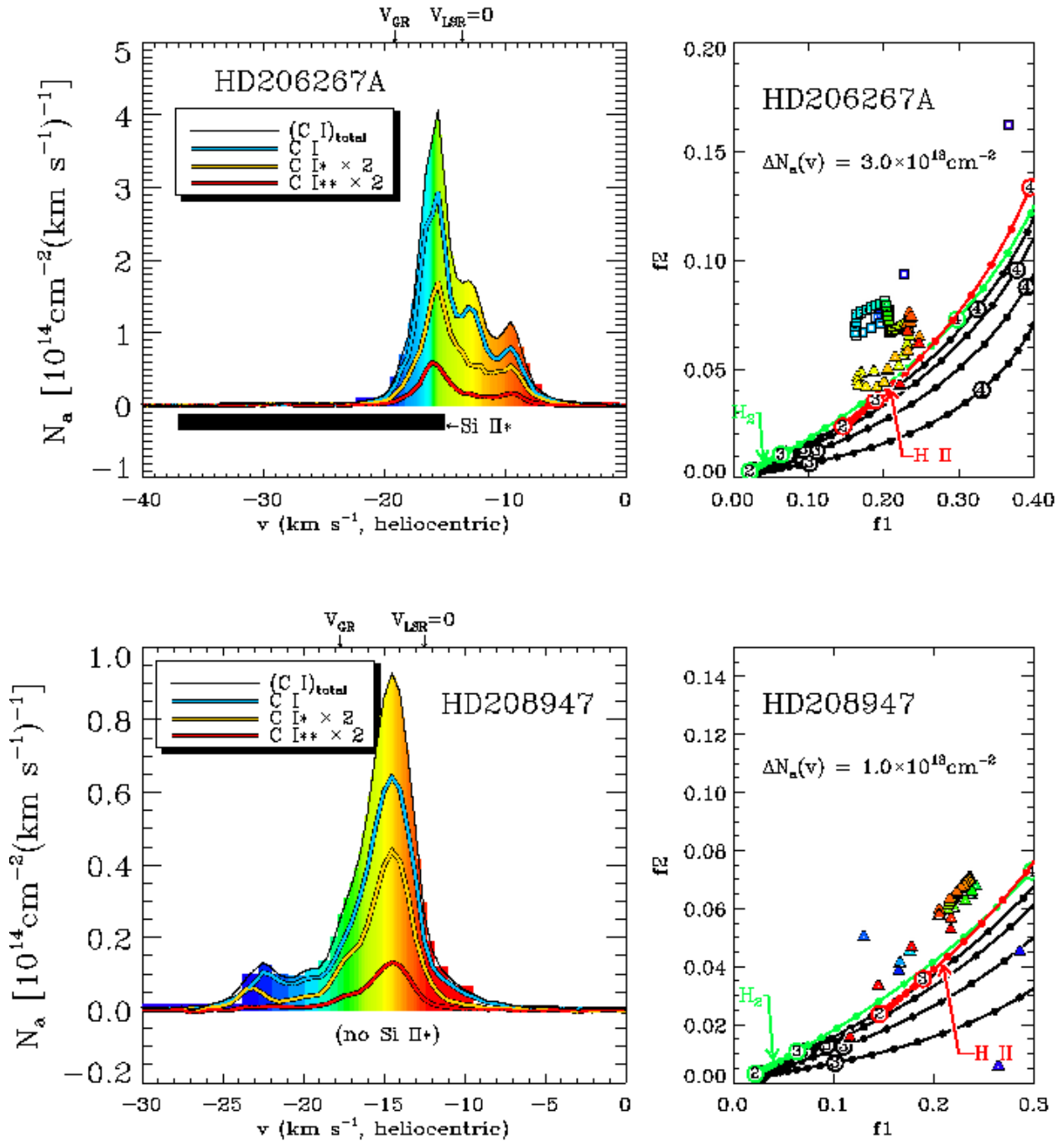


Fig. 7i.— continued

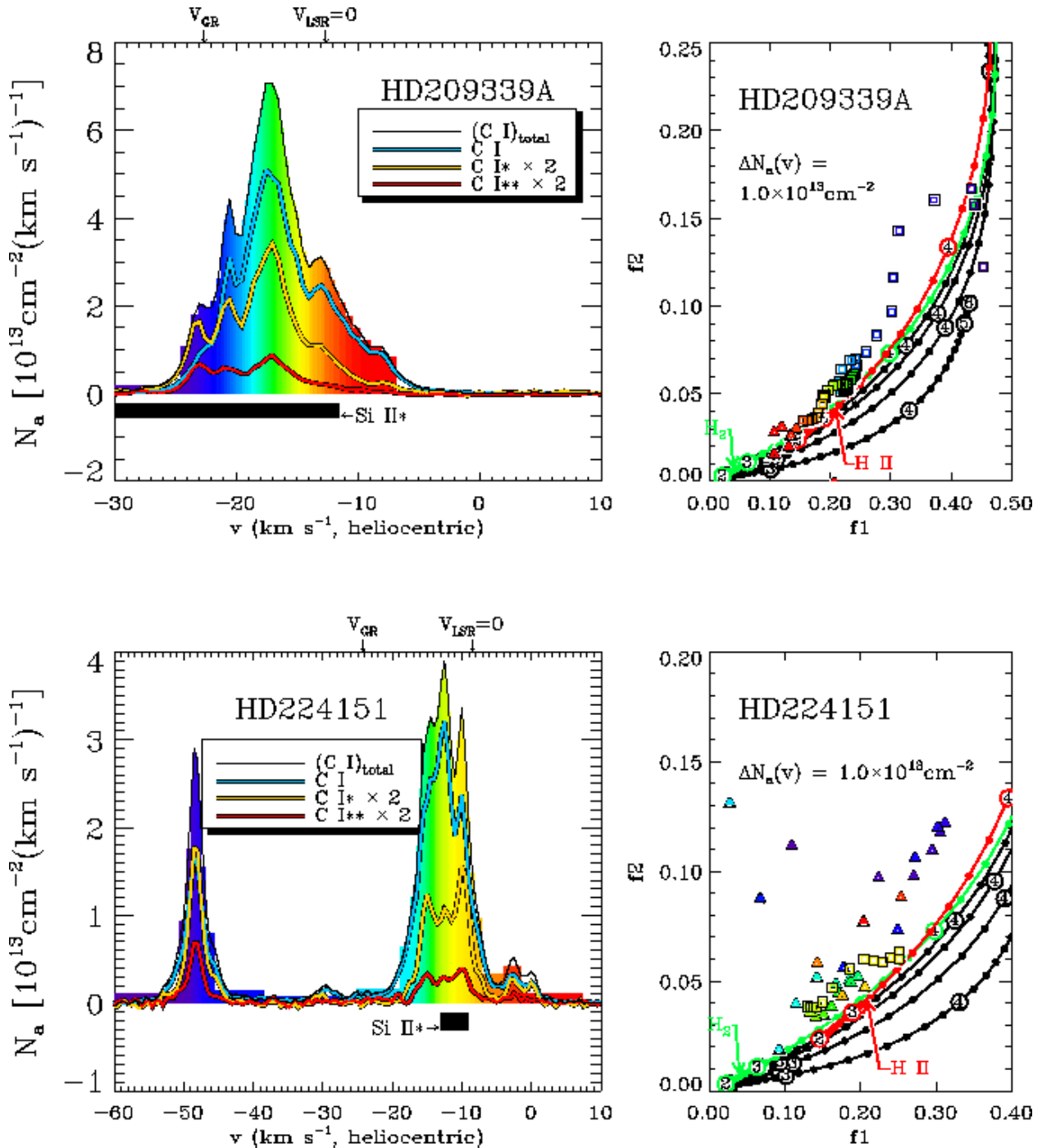


Fig. 7j.— continued

Table 6. Integrated Column Densities^a

HD	$\log N(\text{C I})$ (cm $^{-2}$)	$\log N(\text{C I}^*)$ (cm $^{-2}$)	$\log N(\text{C I}^{**})$ (cm $^{-2}$)	$\log N(\text{C I}_{\text{total}})$ (cm $^{-2}$)
108	14.810	14.320	13.926	14.972
3827	13.514	12.415	12.444	13.580
15137	14.513	13.862	13.219	14.618
69106	14.179	13.555	13.033	14.296
88115	13.956	13.161	12.766	14.044
93843	13.969	13.542	13.112	14.149
94493	14.144	13.504	12.921	14.254
99857A	14.418	13.952	13.397	14.576
103779	14.152	13.365	12.322	14.223
106343	14.210	13.638	13.059	14.337
109399	14.155	13.584	13.049	14.285
116781A	14.188	13.457	12.935	14.282
120086	13.076	12.472	... ^b	13.171
122879	14.309	13.682	13.042	14.420
124314A	14.540	13.970	13.402	14.667
203374A	14.857	14.252	13.763	14.980
206267A	15.160	14.616	14.131	15.300
208947	14.502	13.978	13.418	14.642
209339A	14.608	14.104	13.517	14.753
210839	14.798	14.337	14.013	14.977
224151	14.501	13.898	13.437	14.627

^a $\log[\int N_a(v)dv]$ over the velocity ranges shown in Figs. 6 and 7.^bColumn density consistent with zero, to within the measurement errors.

6.4. Information from O I* and O I**

Neutral oxygen is another element that has absorption features within the wavelength coverage of our survey and, like neutral carbon, has three fine-structure levels in its ground electronic state. The separations of the levels in energy are larger than those for C I, and the radiative decay rates are much larger. As a consequence, measurable concentrations of O I* and O I** occur only when the pressures and temperatures are much higher than those needed to populate C I* and C I**.

All stars in our survey show absorption by telluric O I* and O I** (see Appendix B) from the transitions at 1304.858 and 1306.029 Å, respectively, but only six show additional features that we can attribute to the interstellar medium. These features are shown in Fig. 8, as represented by their $N_a(v)$ profiles. Our derived values of $N_a(v)$ for C I** are shown above them for comparison. The stars HD 93843 and HD 210839 show distinct differences in the shapes and positions of the excited C I and O I features, indicating that the regions have some velocity-dependent stratifications in their physical conditions.

In the wavelength coverage of STIS, there are only two O I lines from the unexcited state: one is an allowed transition at 1302.169 Å and the other a semi-forbidden transition at 1355.598 Å. Unfortunately, the former is usually very badly saturated over a large range of velocity, while the latter is seen only when there is a large amount of material in the line of sight. The only case where we could register an absorption feature at 1355 Å that had accompanying discernible features of O I* and O I** was for HD 210839.

6.5. Physical Conditions in the -35 km s^{-1} Component toward HD 210839

Over all of the C I velocity components studied in our survey, the one centered at -35 km s^{-1} toward HD 210839 (λ Cep) seems to exhibit the clearest evidence for high pressure gas. This negative velocity is generally consistent with a portion of the large, expanding shell of the Cepheus Bubble [$-28 < v_{\text{LSR}} < +9 \text{ km s}^{-1}$ that surrounds this and many other stars in the general vicinity (Patel et al. 1998)]. Evidently this velocity component is not particularly conspicuous in CH⁺, since its presence is not reported by Crane, Lambert & Sheffer (1995), whereas they do present information about CH⁺ blended absorption components centered at $v = -9.5$ and -13.1 km s^{-1} , i.e., velocities consistent with our stronger C I component shown in Fig. 6.

Fortunately, there is enough matter present at -35 km s^{-1} that we can detect a weak absorption by O I for the transition at 1355.598 Å. Using this line in conjunction with the excited lines in the strong multiplet shown in Fig. 8 leads to $N(\text{O I}) = 9.6 \times 10^{16} \text{ cm}^{-2}$,

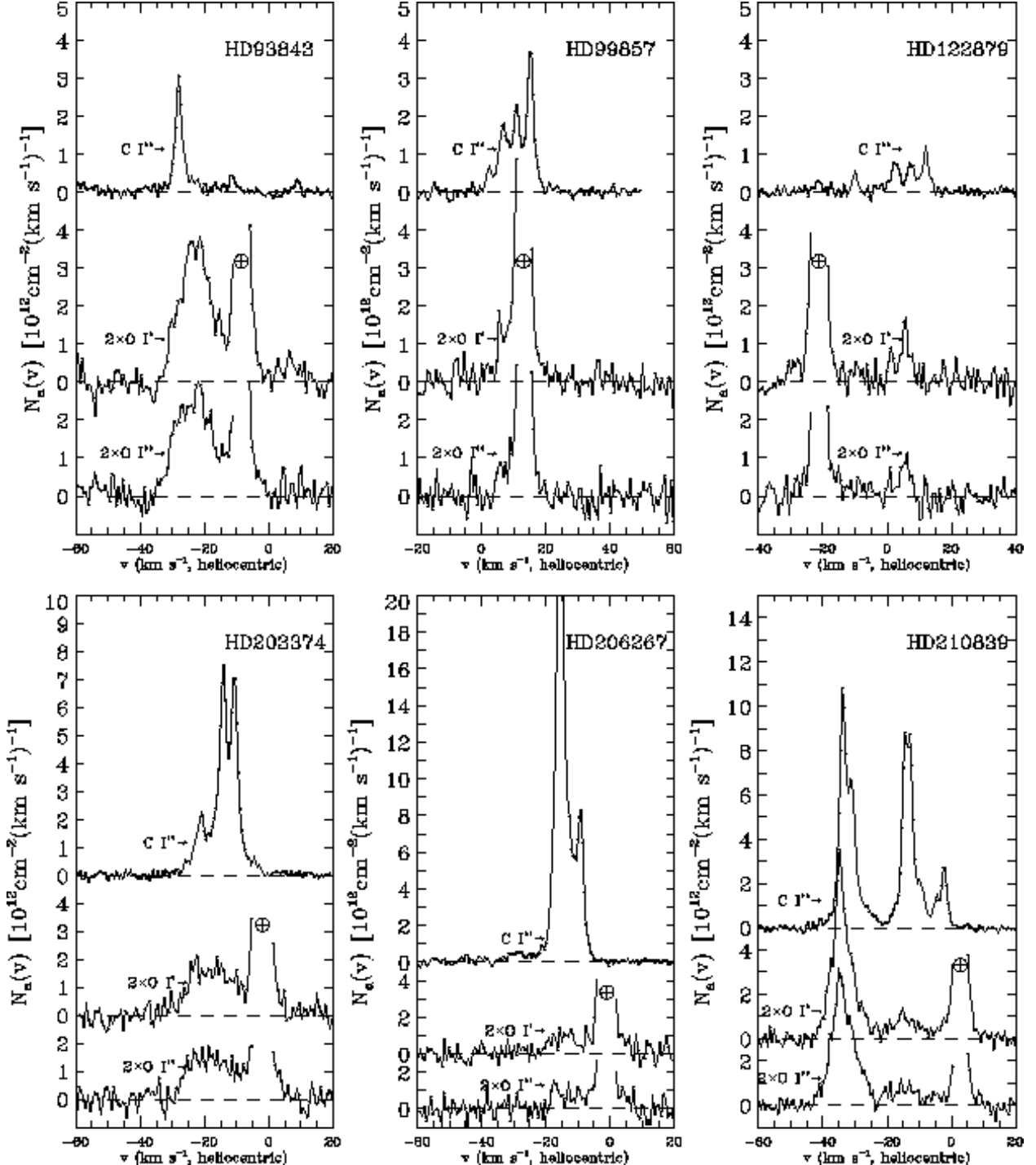


Fig. 8.— A comparison of column densities per unit velocity for C I^{**}, O I^{*}, and O I^{**}, plotted against heliocentric velocity for those stars that showed some detectable absorption from the excited oxygen atoms. The locations of the telluric oxygen absorptions are indicated by the symbol \oplus over the O I^{*} feature. The plots for O I^{*} and O I^{**} have their baselines offset by -5 and -8 in y [unit = $10^{12}\text{cm}^{-2}(\text{km s}^{-1})^{-1}$] and are expanded vertically by a factor of 2 . Values for $N_a(\text{OI}^*)$ and $N_a(\text{OI}^{**})$ were derived using Eq. 2 and values of $\log f\lambda = 1.804$ listed by Morton (1991).

$N(\text{O I}^*) = 2.6 \times 10^{13} \text{ cm}^{-2}$ and $N(\text{O I}^{**}) = 2.3 \times 10^{13} \text{ cm}^{-2}$. For now, we consider the case where the gas is primarily neutral, and later we will present evidence that supports this position. From the tables showing the expected fine-structure population ratios for O I presented by Keenan & Berrington (1988), we find that a region with $n(\text{H I}) = 60 \text{ cm}^{-3}$ and $T \approx 1000 \text{ K}$ gives a reasonably close match to the relative populations that we derived for this component. The resulting pressure, $p/k = 10^{4.8} \text{ cm}^{-3} \text{ K}$, is very close to the answer that we derived for the excitation of C I at high temperatures, as is evident in Fig. 6. This arises from the fact that the theoretical expectations for f_1 and f_2 for neutral gas with $T \sim 1000 \text{ K}$ and various pressures very nearly match the track for fully ionized gas at $T = 7000 \text{ K}$ (Case 3: red tracks in the f_1, f_2 diagrams) at the corresponding identical pressures. The blue, box-like points in the f_1, f_2 diagram are very close to the point representing $p/k = 10^{4.8} \text{ cm}^{-3} \text{ K}$ on the red track.

We consider next evidence provided by the fine-structure excitation of Si II. The strongest transition from Si II* is one at 1264.7 \AA , whose strength may be compared to that of the much weaker line of Si II at 1808.0 \AA . Because it has a positive charge, Si II has its fine-structure excitation dominated by collisions with electrons if the region is not almost completely neutral. The rate coefficient for de-excitations is

$$\gamma_{2,1} = \frac{8.63 \times 10^{-6} \Omega_{1,2}}{g_2 T^{0.5}} \text{ cm}^3 \text{ s}^{-1} \quad (13)$$

(Spitzer 1978, p. 73), with the reverse rate given by detailed balancing, $\gamma_{1,2} = (g_2/g_1) \exp(-E_{1,2}/kT) \gamma_{2,1}$. The statistical weights of the levels are $g_1 = 2$ and $g_2 = 4$, and the temperature equivalent for the difference in energy levels $E_{1,2}/k = 413 \text{ K}$. Thus we find that the condition for equilibrium,

$$n(e) \gamma_{1,2} n(\text{Si II}) = [n(e) \gamma_{2,1} + A_{2,1}] n(\text{Si II}^*) \quad (14)$$

will lead to an equation for the electron density

$$n(e) = \frac{g_2 A_{2,1} T^{0.5} \left[\frac{n(\text{Si II}^*)}{n(\text{Si II})} \right]}{8.63 \times 10^{-6} \Omega_{1,2} \left\{ \left(\frac{g_2}{g_1} \right) \exp \left(\frac{-E_{1,2}}{kT} \right) - \left[\frac{n(\text{Si II}^*)}{n(\text{Si II})} \right] \right\}} , \quad (15)$$

where the radiative decay probability for the upper level is $A_{2,1} = 2.17 \times 10^{-4} \text{ s}^{-1}$ (Nussbaumer 1977), and the collision strength $\Omega_{1,2} = 5.6$ over a broad range of temperature (Keenan et al. 1985).

The derivation of $N(\text{Si II}^*)$ for the velocity complex near -30 km s^{-1} is straightforward, but the corresponding absorption by Si II has strong interference from the main interstellar component at -18 km s^{-1} , as is shown in the top panel of Fig. 9. On the assumption that

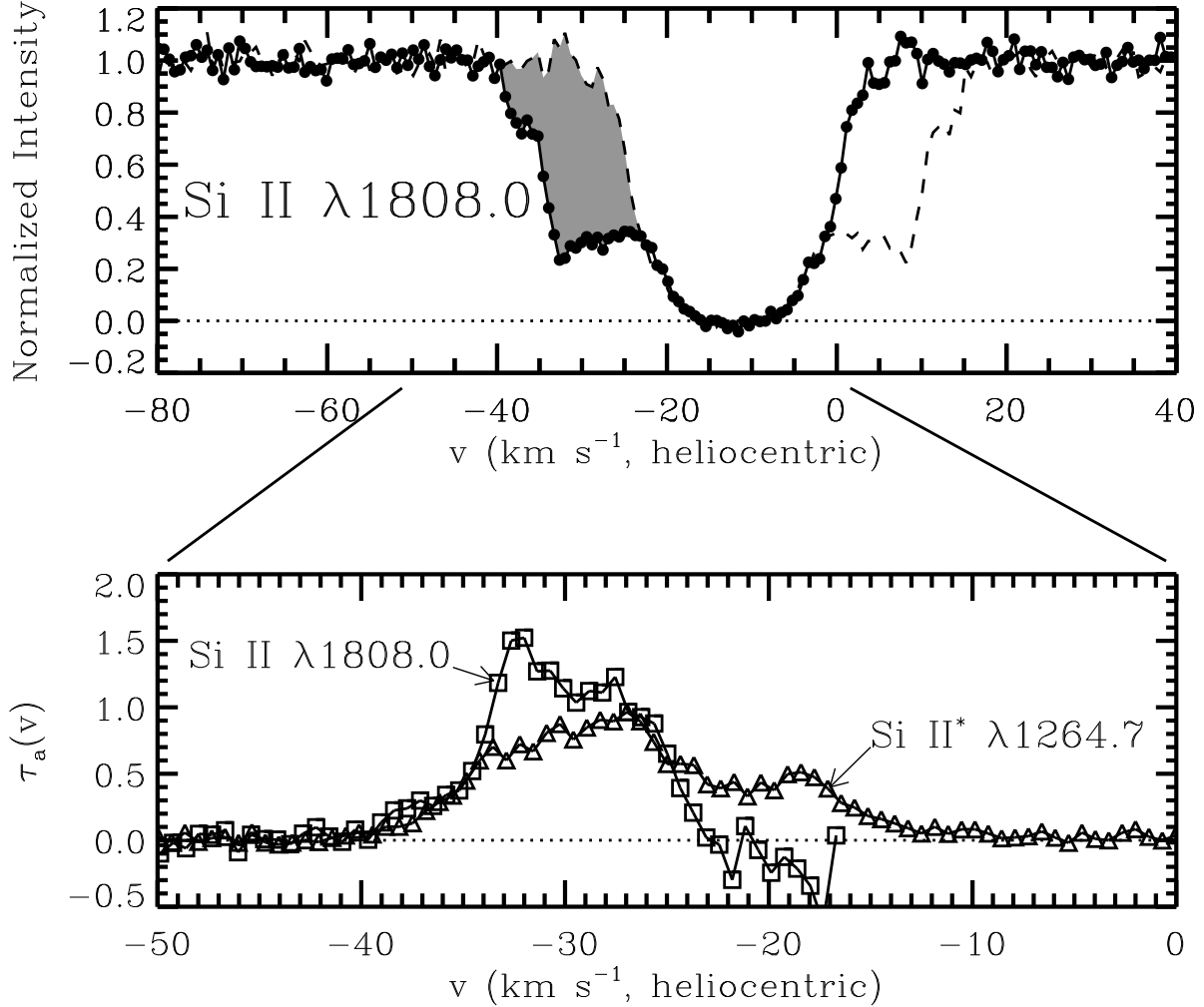


Fig. 9.— *Top panel:* Intensity profile for the absorption by the Si II transition at 1808.013\AA toward HD 210839 (λ Cep), shown by the dark line with dots. The dashed line traces a reflection of this intensity about an axis of symmetry for the main component at -11.9 km s^{-1} . The filled-in area shows the assumed contribution for the absorption centered at -30 km s^{-1} that is expected in the absence of the left-hand wing of the main feature. *Bottom panel:* Apparent optical depths $\tau_a(v)$ for the Si II and Si II* transitions, as labeled. The $\tau_a(v)$ for Si II applies only to the shaded region in the upper panel.

the latter component is perfectly symmetrical and fully resolved by the instrument, we evaluated $\tau_a(v)$ for the high pressure component of Si II against a continuum level that was simply a reflection of the profile about the axis of symmetry of the strong component at -18 km s^{-1} . This absorption is depicted by the shaded region in the figure. The derived $\tau_a(v)$ is shown in the lower panel, overplotted on $\tau_a(v)$ for the Si II* feature at 1264.7 \AA . By integrating the profiles over the velocity interval -40 to -23 km s^{-1} and using Eq. 2 together with the values $\log f\lambda = 0.576$ (Bergeson & Lawler 1993) and 3.100 (Luo, Pradhan, & Shull 1988) for Si II and Si II*, respectively, we find that $N(\text{Si II}) = 1.3 \times 10^{15} \text{ cm}^{-2}$ and $N(\text{Si II}^*) = 4.4 \times 10^{12} \text{ cm}^{-2}$. These two numbers lead to a relative population of 3.5×10^{-3} for the excited form. Substituting this result into Eq. 15, we find that

$$n(e) = 1.0 \exp(0.413T_3) T_3^{0.5} \text{ cm}^{-3} \quad (16)$$

where T_3 is the temperature in units of 1000 K , i.e., for $T_3 = 1$ we obtain $n(e) = 1.5 \text{ cm}^{-3}$. This electron density is not high enough to alter the excited O I populations appreciably from those established by neutral hydrogen collisions. Thus, we feel that it appropriate to identify our C I and O I absorptions as having come from mostly neutral gas. (We note also that the total integrated column density for C I in all three levels for this velocity component is $1.42 \times 10^{14} \text{ cm}^{-2}$, well in excess of what one would predict for the contribution from an H II region generated by one or more O6 stars, as we will show in §7.3.)

It is clear from Figs. 6, 8 and 9 that the velocities and shapes of the excited carbon, oxygen and ionized silicon do not agree in detail, even though they are clearly associated with a complex of gas that has a distinct identity, by virtue of its velocity being well separated from the general gas along the line of sight. All profiles are asymmetrical and have a sharper edge on the negative velocity side than on the positive velocity one. The velocity sequence in peak absorptions start with O I* and O I** profiles at -34.5 km s^{-1} , followed by C I** at -32.5 km s^{-1} (C I and C I* agree with C I** – see Fig. 6), and ending with Si II* which starts to build near the C I and O I maxima, but doesn't reach its peak until -27.5 km s^{-1} . The Si II* profile has an extension to nearly -12 km s^{-1} . Errors in the relative positions of the peaks are of order 1 km s^{-1} , judging from the offsets we found for the carbon multiplets (§4.5).

7. General Interpretation

7.1. Implications of f_2 vs. f_1

Figure 10 shows all of the C I f_1, f_2 points for the 21 stars in the survey. The median value for f_1 for the entire sample is 0.196, which corresponds to $p/k = 2240 \text{ cm}^{-3}\text{K}$ for a purely atomic gas at a most favorable temperature $T = 40\text{K}$. Slightly higher pressures would be derived for temperatures away from this value. We are not surprised to see a broad dispersion of the points, most of which run parallel to the tracks that represent $10^3 < p/k < 10^4 \text{ cm}^{-3}\text{K}$. This behavior seems to reflect chance encounters of the gas regions with random events linked to pressurization and rarefaction in a chaotic medium. However, an unexpected result is that most of the measured values for f_2 seem to be too large for their accompanying f_1 values, if indeed the C I at a particular radial velocity were to reside in a homogeneous region corresponding to any of the three cases for possible mixes of collision particles that we discussed in §6.2 (or admixtures thereof). This is shown by the fact that most of the points fall above the tracks in the diagrams. Looking back to Figs. 6 and 7, we see that particularly noteworthy manifestations of this effect show up on the lines of sight toward HD's 108, 15137, 99857A, 106343, 109399, 116781A, 124314A, 203374A, 206267A, 208947, 210839 and 224151. Recalling the “center of mass” behavior (§6.1 and Fig. 5) for points representing a composite of different regions on the f_1, f_2 diagram, we can reconcile this effect with the existence of a large amount of material within an ordinary range of pressures, i.e., $10^3 \lesssim p/k \lesssim 10^4 \text{ cm}^{-3}\text{K}$, but then accompanied by a small amount of gas at very high pressure having the same radial velocity. From the geometry of how the tracks wrap around in the diagram, it is evident that for the high-pressure gas to be able to “pull” the low-pressure points in a near vertical direction away from their tracks, it must be at a pressure $p/k \gtrsim 10^5 \text{ cm}^{-3}\text{K}$. Except for the components of C I centered at -33 km s^{-1} in the spectrum of HD 210839 and -28 km s^{-1} in the spectrum of HD 93843, this gas at such extraordinary pressures seems never to be unaccompanied by the lower pressure material.

While one might suppose that unusually large C I** populations could arise from the absorption of line-emission photons that are created by H II regions, as we discussed in §6.2.2, it must be remembered that the effect works only if the radial velocity differences are less than the characteristic line widths that average about $\text{FWHM} = 6.7 \text{ km s}^{-1}$ (Huang et al. 1999). Thus, it seems hard to imagine that the C I** populations could be modified over the large ranges of radial velocity that are evident in the figures.

It is important to recognize that while the C I-weighted fraction of this high pressure gas can be of order 0.1, the real fraction of gas, as measured by $N(\text{H})$, can be much lower since a larger fraction of the carbon is in neutral form at high pressures. To take an extreme

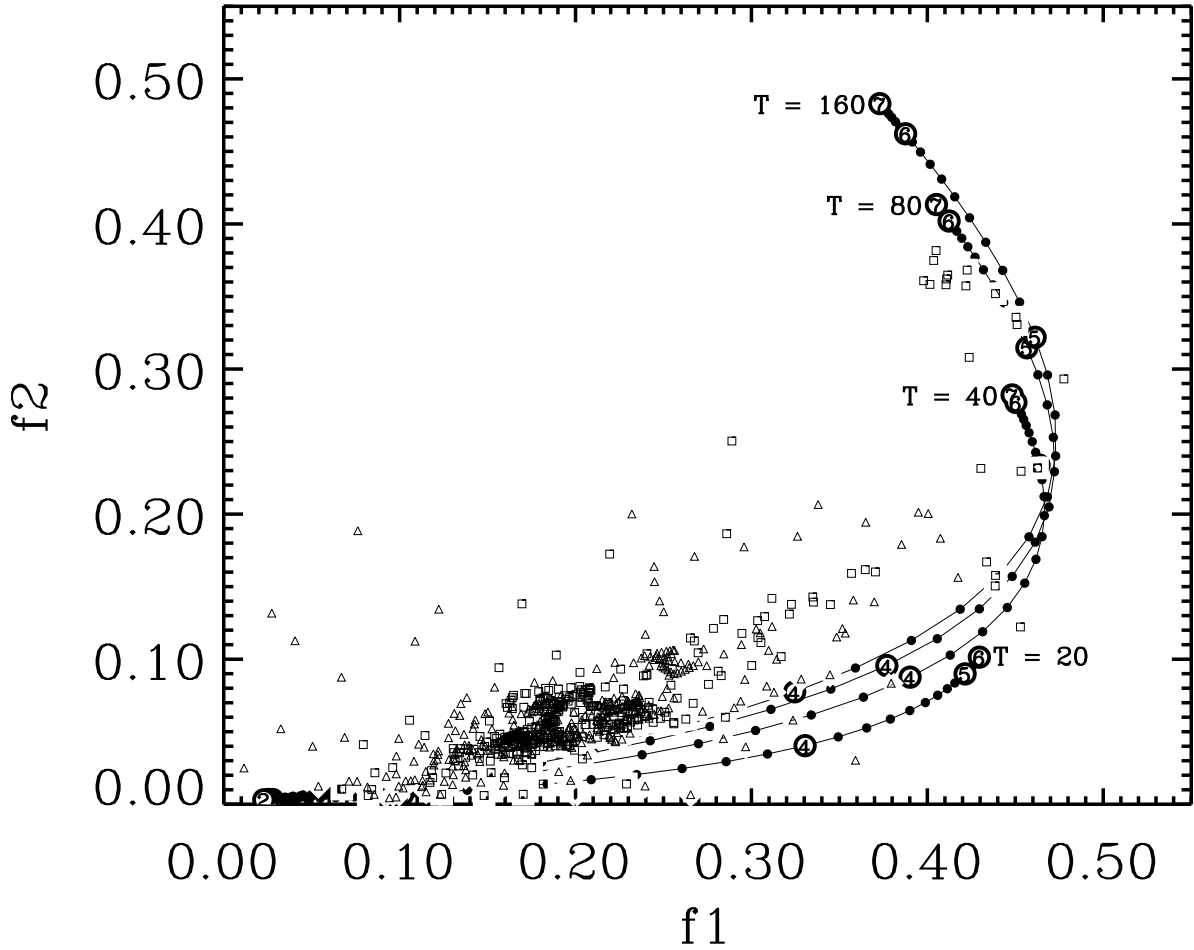


Fig. 10.— The outcome for f_1 and f_2 for all stars in the survey, with triangles representing measurements outside the velocity intervals spanned by Si II* absorption and squares within these intervals (see §7.4). Unlike the treatments for individual stars shown in Figs. 7a, g, and i, $\Delta N_v(v)$ was never allowed to differ from $1.0 \times 10^{13} \text{ cm}^{-2}$, so that all points represent equal amounts of C I. The theoretical tracks for Cases 2 and 3 (§6.2) are omitted for clarity.

example, if indeed $n(\text{C I}_{\text{total}})/n(\text{C}) \propto p/k$ (from $n(e)/n(H)$ being approximately constant), we could envision that a 10^{-5} fraction of the hydrogen at $p/k = 10^6 \text{ cm}^{-3}\text{K}$ would shift a point 10% of the distance spanned from the $f1 - f2$ combination representing the remaining gas at $p/k = 10^2 \text{ cm}^{-3}\text{K}$. Of course, this assumes that the duration of the overpressurized condition is long enough for the carbon to reach a new ionization equilibrium, which can take up to about a thousand years if the photoionization rate is equal to the general galactic value. (Time and length scales are considered further in §8.)

7.2. Simple Checks

Since the conclusions stated above have some far-reaching implications, it is important to verify that the phenomenon is real. For instance, one might have reservations about possible systematic errors that could arise in the solutions to multiplet absorptions (§5.2) or the derivations of relative f -values (§5.3). A very simple test that avoids these complex operations can be implemented to validate the unusual character of our results. Multiplet nr. 4 at 1329 \AA has absorptions from the three levels that are well separated, although the individual transitions from a given excited level are usually blended. The sums of the f -values out of the three levels are identical (this property arises from LS coupling assumed in the published results, and our rederivations agree with it). We now restrict our attention to sight lines that have 1329 \AA multiplets that are of moderate depth, so that they are neither so weak that they are dominated by noise, nor so strong that errors from saturation are large. We then evaluate $\int \tau_a(v) dv$ over the entire widths of the C I* and C I** profiles, knowing that the merging of the lines within them results in our being able to measure only the total column densities without knowing the details in the velocity structures.

Table 7 shows the average values of $\tau_a(v)$ for the complex of three lines arising from C I* centered at 1329.1 \AA , along with similar determinations for the two lines located near 1329.6 \AA for C I**. Measurements of the single line out of C I at 1328.833 \AA are of no use, because this line is saturated when the others are measurable. The ratio of the average τ_a 's, listed in the last column of Table 7, may be compared to the overall averages of $f1/f2$ shown in Figs. 6 and 7. The correspondence between the listed values of $\langle \tau_a(\text{C I}^*) \rangle / \langle \tau_a(\text{C I}^{\text{**}}) \rangle$ and the positions of the points in the respective $f1, f2$ diagrams is excellent for HD 99857A, HD 224151 (both peaks) and HD 210839 (left-hand peak). Reasonably good matches are seen for HD 69106, HD 106343, and HD 124314A. HD 15137, HD 94493 and HD 122879 show matches that are marginally acceptable. The match for HD 116781A is bad, but the value for $\langle \tau_a(\text{C I}^{\text{**}}) \rangle$ is poorly known because the lines are so weak in this multiplet. Overall, our test applied for many lines of sight indicates

that our conclusion that the measurements of f_2 , relative to those of f_1 , are indeed above the theoretical tracks in the diagram, where for $p/k < 2000 \text{ cm}^{-3}\text{K}$ we would expect that f_2/f_1 should always be less than 0.2.

A different approach for questioning the reality of the small amounts of high pressure gas is to examine the possibility that the theoretical tracks themselves are in error. Could there be a problem with any of the physical data used to derive them in §6.2.1? It is difficult to make a fundamental judgement on whether or not the calculations of the collisional rate constants or radiative decay rates have substantial enough errors to mislead us, but we can draw upon real evidence from interstellar absorption lines that indicates that the tracks indeed go about as low in the $f_1 - f_2$ diagram as we have drawn them in the figures. An analysis of the C I lines in the two strongest velocity components toward HD 215733 by Fitzpatrick & Spitzer (1997) shows nominal values of (f_1, f_2) equal to $(0.140, 0.0131)$ and $(0.134, 0.0181)$ for their Components 17 and 18, respectively. The ratio of f_2 to f_1 is the critical quantity for testing the placement of the theoretical tracks. Fortunately, the solutions for $N(\text{C I}^*)$ and $N(\text{C I}^{**})$ in the analysis of Fitzpatrick & Spitzer (1997) depend almost entirely on the data from a single multiplet ($\lambda 1561$), thus avoiding the issue of relative errors in f -values from one multiplet to the next. This increases the confidence in the validity of the nominal values for $f_2/f_1 = 0.093$ and 0.135 (but only if the LS coupling rules apply for the strengths of lines within this multiplet). Thus, in the vicinity of $f_1 \approx 0.14$, the values of f_2/f_1 are indeed consistent with the tracks. The agreement is satisfactory even if we take the values $f_2/f_1 = 0.14$ and 0.19 that arise from Fitzpatrick & Spitzer's lower limits for $N(\text{C I}^*)$ and upper limits for $N(\text{C I}^{**})$. By concentrating on good quality data and choosing a pair of regions that appear to be physically homogeneous and well separated in velocity from other C I components, we have demonstrated that the positions of the theoretical tracks are reasonable. (It should be evident that there is no combination of different conditions that could produce a composite measurement *below* the tracks in this part of the diagram).

Table 7. Average Optical Depths^a

HD	$\langle \tau_a(\text{C I}^*) \rangle$	$\langle \tau_a(\text{C I}^{**}) \rangle$	$\langle \tau_a(\text{C I}^{**}) \rangle / \langle \tau_a(\text{C I}^*) \rangle$
15137	0.846	0.170	0.201
69106	0.549	0.134	0.241
94493	0.235	0.052	0.221
99857A	0.985	0.326	0.331
106343	0.542	0.129	0.238
116781A	0.192	0.042	0.218:
122879 ^b	0.446	0.088	0.197
124314A	0.740	0.172	0.232
224151 ^c	0.583	0.289	0.496
224151 ^b	0.564	0.153	0.271
210839 ^c	1.121	0.993	0.886

^aFor the following blended absorption features: C I* = $\lambda\lambda$ 1329.0853, 1329.1004, 1329.1233 Å; C I** = $\lambda\lambda$ 1329.5775, 1329.6005 Å.

^bRight-hand peak only.

^cLeft-hand peak only.

7.3. C I from a Target Star’s H II Region

In view of the fact that each line of sight penetrates half of the volume of at least one early-type star’s Strömgren sphere, one might question whether or not C I in this region could distort our findings, which are presumed to represent simply a composite sample of conditions in H I regions of moderate density. This could have a significant impact in raising our perceived pressures, since H II regions created by young stars need typically about 2×10^6 yr for their internal densities to drop to about 1/10 their initial values (Spitzer 1978, pp. 251–255). This time is significant compared to the lifetimes of our target stars, which range from about 4×10^6 yr for O5 stars to 10^7 yr for B0 V stars (Schaller et al. 1992).

We now produce some quantitative estimates of how seriously our results could be affected by the contamination from each target star’s H II region. Jenkins & Shaya (1979) developed a way to calculate the amount of C I that should be present between an early-type star and the edge of its Strömgren sphere. They found that $N(\text{C I})$ could be as large as

$$N(\text{C I}_{\text{total}}) = 2(\text{C/H})\alpha_{\text{C}}\alpha_{2,\text{H}}^{-1}N_{0,\text{L}}\Gamma_{0,\text{C}}^{-1} \quad (17)$$

where $\text{C/H} = 2.3 \times 10^{-4}$ is the abundance of carbon relative to hydrogen⁷ [adopted from the B-star abundance ratio measured by Cunha & Lambert (1994)], α_{C} is the recombination rate of carbon with free electrons, $\alpha_{2,\text{H}}$ is the recombination rate of hydrogen to any of its levels with $n \geq 2$, $N_{0,\text{L}}$ is the number of Lyman-limit photons emitted (in units of $\text{cm}^{-2}\text{s}^{-1}$) at the star’s surface, and $\Gamma_{0,\text{C}}$ is the ionization rate of neutral C at the star’s surface.

Figure 11 shows our calculations of $N(\text{C I}_{\text{total}})$ from Eq. 17 for stars with various effective temperatures T_e and surface gravities of 10^3 , 10^4 and 10^5 cm s^{-2} , using the stellar atmosphere model calculations of ionizing fluxes by Kurucz (1993, 1997) to obtain $N_{0,\text{L}}$ and $\Gamma_{0,\text{C}}$. The recombination coefficient α_{C} is from the radiative and dielectronic rates given by Shull & van Steenberg (1982), supplemented by the additional contributions from low-lying resonance states computed by Nussbaumer & Storey (1986). The rate $\alpha_{2,\text{H}}$ is from Spitzer (1978, pp. 106–110). Both rates were evaluated for $T = 8000$ K.

The expression in Eq. 17 overestimates the amount of C I if the Strömgren sphere is one of low density, since near the edge the star’s ionizing radiation is supplemented by the general interstellar ionizing field. The results of Jenkins & Shaya (1979) show that this effect can lower the estimate for $N(\text{C I})$ by as much as 0.4 dex in some cases.

Generally, it is evident that of order $10^{13.5} \text{ cm}^{-2}$ of the C I might arise from the H II

⁷Note that this value is larger than the one that we adopted in §5.3.2 because we are not certain that C is depleted in H II regions. This might lead to an overestimate for $N(\text{C I}_{\text{total}})$.

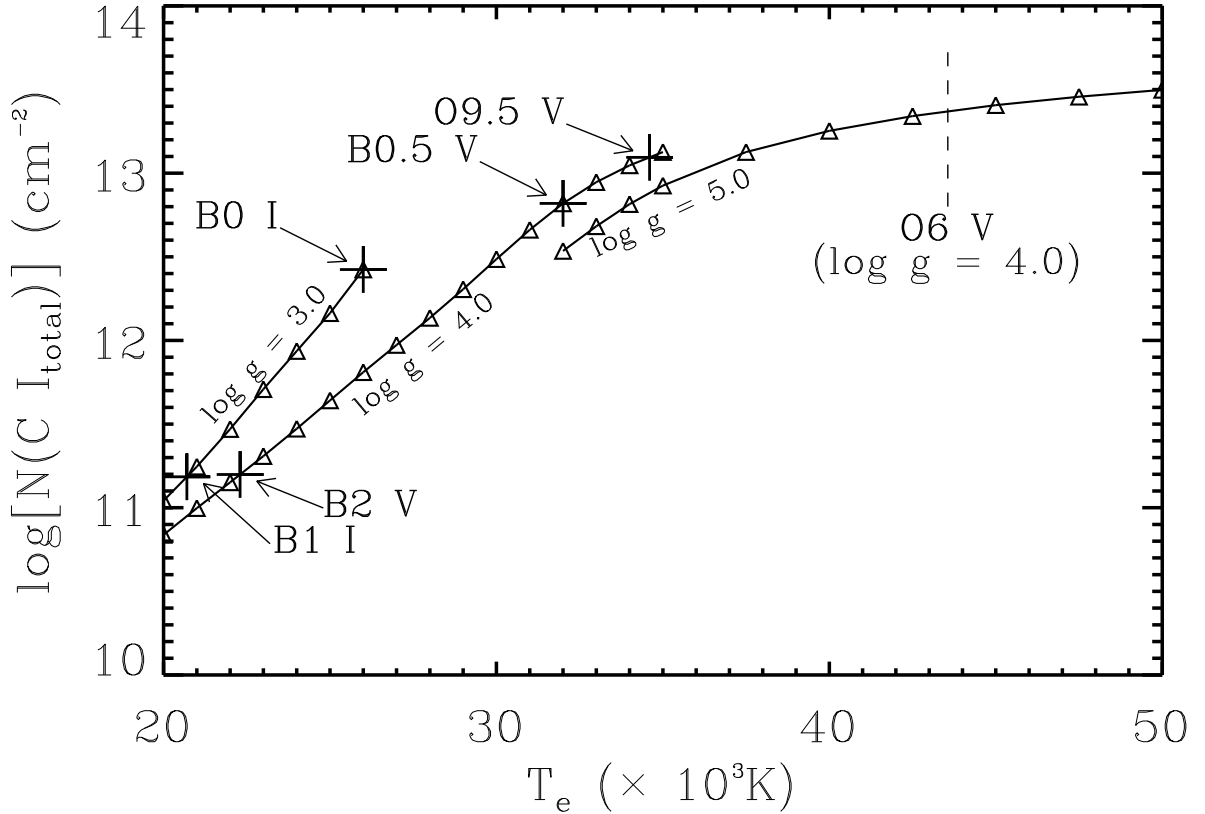


Fig. 11.— Estimated column density of atomic carbon from the surface of a target star to the edge of its Strömgren sphere, as a function of a star’s effective temperature T_e . These results arise from the application of Eq. 17, using the fluxes from model stellar atmospheres of Kurucz (1993, 1997) for stars with different T_e and surface gravities. The locations of stars of various spectral types in this diagram are indicated, using the effective temperature scales listed by Tokunaga (2000) for the B-type stars and Vacca et al. (1996) for the O-type stars. The O6 main-sequence stars have $\log g = 4.0$, but model atmosphere calculations are not available for this surface gravity at the higher values of T_e .

region created by a very hot star, and it follows that this region or a photodissociation front on its edge may be responsible for some readings of high pressure. Even so, this perturbation in our results should be restricted to a limited span of radial velocity in each case, one that is likely to be near the star’s radial velocity v_* (see col. 3 of Table 1) or $v_{\text{gal. rot.}}$ (col. 6 of Table 2) if the star has a large peculiar velocity, such as HD 210839.

7.4. Si II* as an Indicator for other H II Regions

Our study has concentrated on C I, with some occasional insights provided by O I. However as we discussed in §6.5, ionized silicon provides yet one more example showing transitions from an excited fine-structure level within the wavelength coverage of STIS. If Si II* is present without an accompanying stronger absorption by O I*, we can be confident that the absorption arises from a region where most of the hydrogen is ionized (Spitzer & Jenkins 1975). If $p/k = 10^4 \text{ cm}^{-3}\text{K}$ in a warm ionized medium (WIM), $n(\text{C I}^{**})/n(\text{C}) = 2 \times 10^{-4}$ if $T = 8000 \text{ K}$ and $\Gamma_{\text{C}} = 3 \times 10^{-10} \text{ s}^{-1}$, i.e., the normal interstellar ionization rate with no enhancement by especially nearby stars. Under these same conditions, we expect that $n(\text{Si II}^*)/n(\text{Si II}_{\text{total}}) = 8 \times 10^{-4}$; see Eq. 15. If the Si and C are depleted by -1.3 dex (Savage & Sembach 1996) and -0.4 dex (§5.3.2), respectively, we would expect to find roughly comparable strengths for the Si II* line at 1264.7 \AA and the combined effect of the two strong lines of C I** centered at 1329.6 \AA . For $p/k > 10^4 \text{ cm}^{-3}\text{K}$, f_2 increases more slowly than $n(\text{Si II}^*)/n(\text{Si II}_{\text{total}})$, but this is outweighed by the linear dependence of $n(\text{C I}_{\text{total}})/n(\text{C})$ on $n(e)$, making the Si II* line weaker than that for C I**. It is clear, in a broad sense, that we can use the 1264.738 \AA line of Si II* to warn us about the presence of C I** that may have been brought about chiefly by gas that is fully ionized.

The black bars just below the $N_a(v)$ profiles shown in Figs. 6 and 7 show the velocity ranges over which the absorption by Si II* at 1264.7 \AA is greater than 10% of the local continuum. We find that in many cases these bars subtend major fractions of the C I absorbing velocity ranges. However, there are also several sight lines where little or no Si II* is detected.

To investigate whether or not the presence of Si II* is associated with any abnormalities in the C I fine-structure ratios, we derived the distribution functions for f_1 that pertained to measurements both within and outside of the Si II* velocity spans. The results are shown in Fig. 12. There seems to be no significant difference between the two, other than the fact that the measurements outside of the Si II* bands show a larger dispersion of values. This outcome might arise from the larger errors for measurements at the velocity extremes, or alternatively, for independent kinematical reasons discussed in §7.5 below. The apparent

lack of a real difference indicates that the possible presence of H II regions is probably not an important factor that influences the general pressure sensed by the C I excitation.

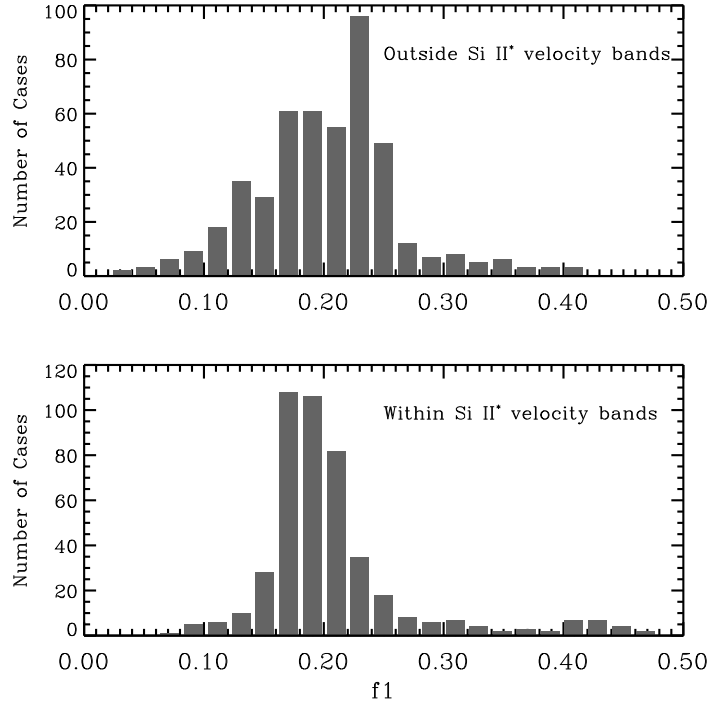


Fig. 12.— *Top panel:* The frequency of occurrences of f_1 for C I outside the velocity coverage of Si II* ($>10\%$ absorption at 1264.738 Å) compared with the analysis for points inside the Si II* ranges (*bottom panel*).

We performed a similar comparison for f_2/f_1 for all cases where $f_1 < 0.3$ to test if the presence of Si II* had any bearing on the tendency for points to fall above the theoretical tracks, as we pointed out in §7.1. Figure 13 shows that C I within the Si II* bands shows a slightly greater tendency to show values $0.30 < f_2/f_1 < 0.45$ than for determinations on the outside. A Kolmogorov-Smirnov test indicates that the two distributions are drawn from different populations at the 99.9% confidence level. Whether or not the presence of Si II* is the main discriminant is still open to question, however. Again, the difference may simply be due to general kinematical considerations.

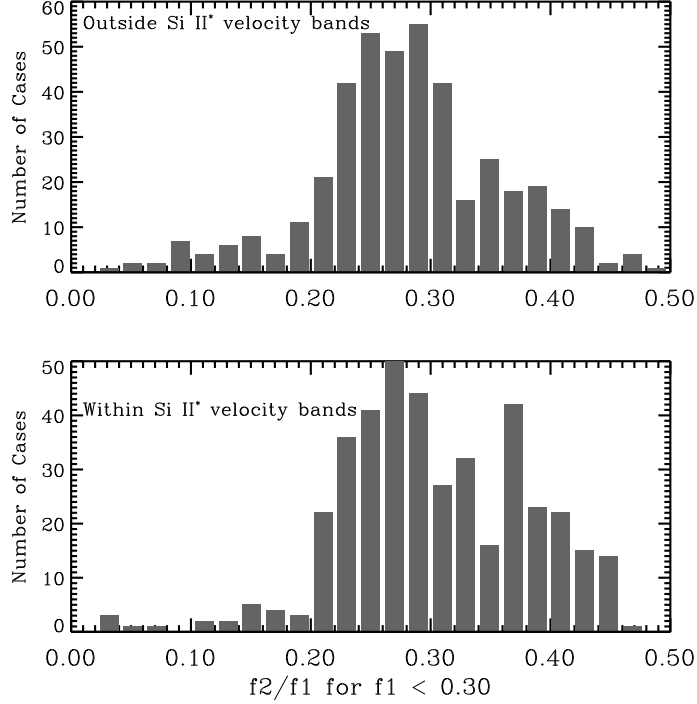


Fig. 13.— Same as for Fig. 12 except that the frequencies of f_2/f_1 for $f_1 < 0.3$ are shown for the two populations of C I measurements.

7.5. The Effects of Kinematics on C I Excitation

Since dynamical events are probably the principal drivers of transient changes in pressure, it is worthwhile to investigate whether or not we see evidence for changes in the C I excitation linked to the kinematical properties of the material. Gas that is quiescent could be identified as having radial velocities between the velocity of differential galactic rotation v_{GR} at the position of the target star and zero point for the Local Standard of Rest $v_{\text{LSR}} = 0$. This material is less likely to have been disturbed by some compression or rarefaction event in the recent past. The heliocentric velocities that mark the adopted endpoints for such gas toward each target are indicated in Table 2⁸ and Figs. 6 and 7. Gas with velocities outside this interval is most likely to represent disturbed material. However, we must not overlook the fact that such material may also be found within these velocity limits, since it could be moving transverse to the line of sight (or have a local velocity offset

⁸The endpoints are actually the maximum and minimum values of the entries – Column 5 and (Column 6 – Column 5) of the table.

that still does not transgress one of our boundaries) or represent turbulent compression arising from oppositely directed flows whose momenta nearly cancel each other.

To explore possible differences between moving and quiescent gases, we start by dividing up our measurements into three velocity intervals: (1) gases at velocities above the interval spanned by v_{GR} and the zero point for v_{LSR} , (2) gas within this interval and (3) gas at velocities below the interval. Interval (3) differs from (1) in one important respect: since this interval includes includes gas that is moving toward us with respect to gases in the general vicinity of the star, it could represent material that is acted upon by the stellar wind of the target star or its neighbors. It could also signal the presence of neutral gas situated at the foreground edge of the star’s H II region which is accelerated by a shock driven by the suddenly overpressured, ionized gas to the rear from our vantagepoint. For all but one star, HD 69106, we have the configuration that v_{GR} is below the zero point for v_{LSR} , which means that most of the time the material moving away from the star should be separated from the more general foreground gas.

Now that we have defined the velocity intervals, we examine how various measurements of f_1 and f_2 differ from one case to the next. The outcomes for f_1 and f_2/f_1 (with $f_1 < 0.30$) in the three velocity divisions are shown in Figs. 14 and 15, respectively. From Fig. 14 it is evident that cases where $f_1 > 0.30$ come almost exclusively from measurements outside the range of “allowed velocities.” (Note that vertical magnifications vary from one panel to the next in the figures.) There is no question about the reality of the samples with large f_1 on the negative side: the extreme deviations toward positive f_1 arise primarily from HD 93843 and HD 210839, and some milder excursions having $f_1 \sim 0.3$ come from gas at the most negative velocities for HD’s 203374A, 209339A and 224151. It seems reasonable to identify the material that is compressed and appears at $v \approx -22 \text{ km s}^{-1}$ in front of HD’s 203374A and 209339A as part of the expanding shell associated with the Cepheus Bubble (Patel et al. 1998). On the positive velocity side, i.e., above the allowed velocity range, less spectacular but nevertheless believable results with $f_1 > 0.30$ are seen for HD’s 108, 99857A, 106343, 122879, and 210839.

Do the deviations of f_1 toward the low end of the distribution for the allowed velocities, i.e., $f_1 < 0.10$, arise from results that can be trusted? We believe that most of them, such as those those that came from HD’s 15137, 93843, 94493 [only a single contribution representing $\Delta N_a(v)$], 103779, 116781A [only 2 $\Delta N_a(v)$ determinations], and 122879 are reliable, while those for HD’s 3827, 109399, and 224151 are not.

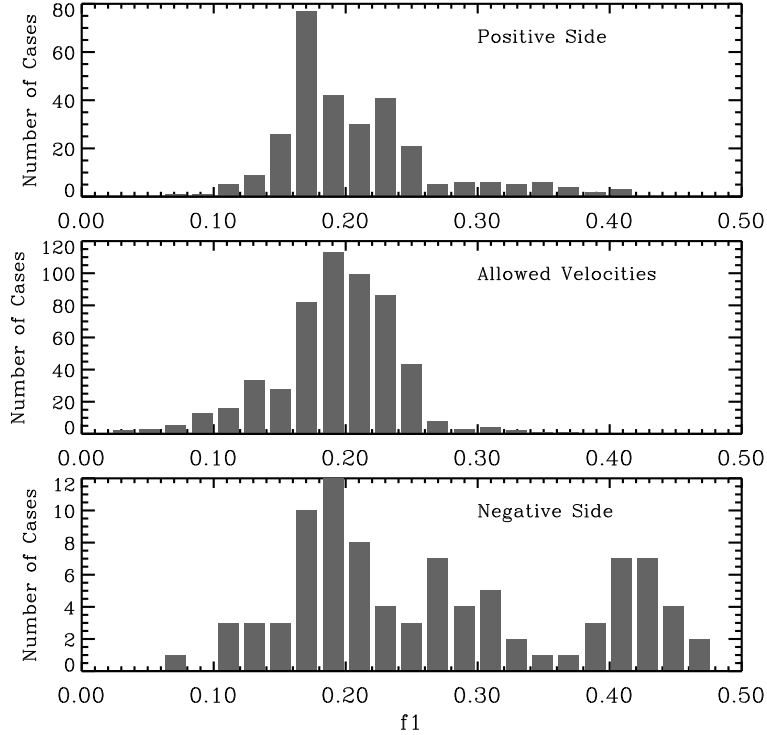


Fig. 14.— The frequency of occurrences of $f1$ for C I above (*top panel*), within (*middle panel*), and below (*bottom panel*) the “allowed” velocity ranges spanned by v_{GR} and $v_{\text{LSR}} = 0$ shown for the profiles in Figs. 6 and 7.

To summarize, thermal pressures represented by $f1 > 0.30$, corresponding to $p/k > 5000$ to $10^4 \text{ cm}^{-3} \text{ K}$ (depending on temperature), almost exclusively arise from gas outside the allowed velocity range. The data shown in Fig. 14 indicate that about 15% of the gas parcels moving outside the allowed velocities have $f1 > 0.30$, whereas this applies to only 1.5% of material within the allowed velocities. While the most spectacular cases occur with negative velocity gas, perhaps associated with gas driven by stellar winds from the target star, examples for high pressures are also evident for gas moving at extraordinary positive velocities. For rapidly moving material, there seem to be very few incidents showing very strong rarefactions. Nearly all of the cases with $f1 < 0.10$ ($p/k < 1000 \text{ cm}^{-3} \text{ K}$) arise from gas inside the allowed range of velocities.

Table 8 shows numerical values for the breakdown into broad pressure ranges for the three kinematical divisions. The definitions of the pressure boundaries are approximate, due to the uncertainties in temperature. Also, our definition of pressure ignores the elevation of f_1 caused by the contribution from the high pressure matter that is responsible for pulling f_2 above the theoretical tracks.

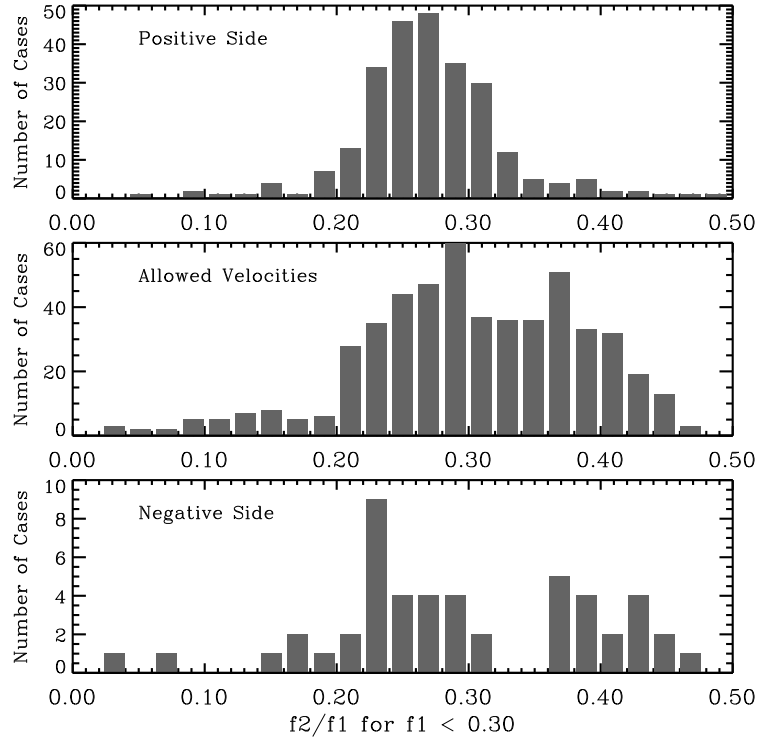


Fig. 15.— Same as for Fig. 14 except that the frequencies of f_2/f_1 for $f_1 < 0.3$ are shown for the three populations of C I measurements.

Turning to Fig. 15, we find that our index that senses the presence of a small amount of gas at extreme pressures ($p/k \gtrsim 10^5 \text{ cm}^{-3} \text{ K}$, see §7.1), f_2/f_1 for $f_1 < 0.3$, shows distinct differences between the three panels. A Kolmogorov-Smirnov test reveals that all three cases are drawn from populations that differ from each other at more than the 98% level of significance. Gas that has no detectable contribution from high pressures, signified by $f_1/f_2 < 0.20$, seems to be present in all three velocity divisions: 6.6% of the cases in the positive range, 8.3% in the allowed range, and 12.2% in the negative range. The differences in these percentages are not significant – they can easily arise from the uncertainties in counting small numbers of discrete events. We are led to conclude that the incidence of small contributions from high pressure gas is ubiquitous.

Table 8. Relative Fractions^a of Occurrences of Different Pressures

Velocity Division	Number of Cases ^b	$\log p/k \lesssim 10^{3.0}$ ($f_1 < 0.10$)	$10^{3.0} \lesssim \log p/k \lesssim 10^{3.5}$ ($0.10 < f_1 < 0.22$)	$10^{3.5} \lesssim \log p/k \lesssim 10^{4.0}$ ($0.22 < f_1 < 0.36$)	$\log p/k \gtrsim 10^{4.0}$ ($f_1 > 0.36$)
Positive	290	0.001	0.658	0.310	0.031
Allowed	542	0.042	0.685	0.271	0.002
Negative	90	0.011	0.433	0.289	0.267
All	922	0.028	0.650	0.285	0.037

^aFractions apply to each row in the table, not the table as a whole.

^bEach occurrence applies to an accumulation of $\Delta N_a(C I_{\text{total}}) = 1.0 \times 10^{13} \text{ cm}^{-2}$.

8. Discussion

We have used C I fine-structure excitations to indicate the distribution of thermal pressures in the ISM. If we exclude gas with large negative velocities, i.e., material which might be connected in some way with mass ejected from the target stars, we find that most of the observations indicate pressures in the general range $10^3 \lesssim p/k \lesssim 10^4 \text{ cm}^{-3} \text{ K}$, as indicated in Table 8. However, an unexpected and noteworthy outcome of our study is the evidence for a small but pervasive admixture of high-pressure material ($p/k \gtrsim 10^5 \text{ cm}^{-3} \text{ K}$) within the matrix of gas exhibiting a more normal range of thermal pressures. Figure 10 indicates that this phenomenon exists over most samples in the lines of sight in our survey, with the instances showing gas without such high-pressure contributions being the exception, instead of the rule. The ubiquity of small contributions from the high pressure state seems to indicate that we are not viewing just occasional manifestations of some isolated, sporadic events, such as the compressions following individual shock fronts from stellar winds or nearby supernova events. Instead, the phenomenon seems to be a persistent but perhaps highly convoluted pattern woven into the fabric of the general ISM.

We now address what other kinds of observations might show some evidence that can support existence of, and give added information about, the regions that show enhanced thermal pressures. One obvious class is the broad range of investigations that have revealed the presence of small-scale enhancements in gas density, starting with the discovery of $0''.1$ structures in the 21-cm H I absorption against the extragalactic source 3C 147 by Dieter, Welch & Romney (1976). Confirmations of this phenomenon came from similar studies toward other sources (Diamond et al. 1989; Davis, Diamond, & Goss 1996; Faison et al. 1998), along with observations of variations in molecular line absorption (Marscher, Moore, & Bania 1993; Moore & Marscher 1995). Likewise, Frail et al. (1994) observed 21-cm absorptions that varied with time toward pulsars with high transverse velocities. These findings, along with studies of differences in visible and uv absorption features toward visual binary stars (Meyer & Blades 1996; Watson & Meyer 1996; Lauroesch et al. 1998; Lauroesch & Meyer 1999; Lauroesch, Meyer, & Blades 2000) and stars in a globular cluster (Meyer & Lauroesch 1999), suggest the presence of density enhancements over size scales ranging from tens to thousands of AU. Indeed, one of these absorption line observations can be directly related to a measurement of C I excitation in our survey. Lauroesch & Meyer (1999) observed three members of the visual multiple star HD206267 (Components A, C and D). They found the greatest column density variations for a velocity component at -17.2 km s^{-1} . This is consistent with our finding an upward excursion of $f2$ above the theoretical tracks at velocities similar to this value (as depicted by the green and blue points in the upper right panel of Fig. 7*i*). However, this correspondence is too fragmentary for us to claim that we have a convincing case for a meaningful relationship between the presence

of small-scale structures and gas at greatly elevated pressures.

The extent to which the apparent changes in 21-cm and visible absorption lines are amplified by reductions in temperature is unclear. Both kinds of absorption become stronger with decreasing temperature at a constant density, scaling in proportion to T^{-1} and $\sim T^{-0.7}$, respectively. Moreover, the very large densities ($n(H) \sim 10^5 - 10^6 \text{ cm}^{-3}$) that one derives from the column density differences divided by the transverse separations may be misleading (Deshpande 2000). Heiles (1997) pointed out the severe difficulties that arise from the simple characterization of discrete, static blobs of gas at such densities. Aside from the obvious problem of how such clouds are contained in a medium with a much lower (total) pressure, Heiles pointed out that one should ordinarily predict the existence of an inadmissibly large amount of H₂ (and accompanying extinction) in each cloud. [Even moderate increases of molecular content for very small, isolated clouds that absorb at 21-cm seems to be ruled out by the lack of corresponding CO emission (Gibson et al. 2000)]. Heiles (1997) suggested that this overproduction of H₂ could be overcome if the structures had large longitudinal dimensions and thus much lower internal densities because they consisted of curved filaments or sheets viewed near their tangent points. He also proposed that low temperatures ($T \sim 15 \text{ K}$) would help to resolve the pressure imbalance.

Regardless of their geometry, if small-scale density enhancements are indeed accompanied by significant drops in temperature, it would be hard to relate them to our detections of small amounts of highly excited C I because the Boltzmann factors in the upward collisional rate constants become very small (recall that the energies of the excited levels have temperature equivalents $E/k = 23.6$ and 62.4 K). This is clearly shown by the behavior of the theoretically expected $f_1 - f_2$ tracks that appears in lower right-hand panel of Fig. 6. For instance, when $T = 20 \text{ K}$ we find that f_2 should never exceed about 0.10, even for p/k approaching $10^6 \text{ cm}^{-3} \text{ K}$. We will revisit this issue in a slightly different context further on in our discussion.

It is plausible that our results are signaling the presence of ephemeral enhancements of pressure caused by the inertial forces that arise from supersonic interstellar turbulence. This is an outgrowth of the picture that cusp-like compressions of gas are continuously being created and deformed by an ever-changing, stochastic swirl of converging flows. It is a picture of the ISM that conforms with a structural description consisting of a continuum of varying density enhancements suggested long ago by Chandrasekhar & Münch (1952) and departs from the usual paradigm of discrete, static clouds with well defined boundaries that are constrained by various forms of external pressure from a surrounding medium. Hydrodynamical simulations of turbulence under typical interstellar conditions indeed show that ridges of enhanced density should arise when randomly directed flows of material

collide with each other (Vázquez-Semadeni, Passot, & Pouquet 1995; Scalo et al. 1998; Ballesteros-Paredes, Vázquez-Semadeni, & Scalo 1999; Elmegreen 1999), with lifetimes that exceed the crossing time for the gas particles through the thickness of each region (Elmegreen 1993b). These structures are expected to be found over a very broad range of size scales, reflecting the downward cascade of turbulent wavenumbers. In regimes of density that are higher than what we can observe, these compressions that arise from supersonic turbulence might, along with other instabilities, help lead to star formation (Larson 1981; Hunter et al. 1986; Elmegreen 1993a, b).

As long as the size of a region is much greater than a critical length of about 10^{-2} pc (see Eq. 18 below), the time scale for the gas to arrive at a thermal equilibrium after compression or expansion is considerably shorter [$\sim 2 \times 10^4$ yr for the cold, neutral medium (Wolfire et al. 1995)] than the typical residence time of atoms in the new state (Ballesteros-Paredes, Vázquez-Semadeni, & Scalo 1999). When this requirement is satisfied, we can anticipate that there should be a unique sequence of temperature as a function of density governed purely by the rates of heat loss and gain by various (sometimes indirect) means of absorbing or emitting radiation. Thus, over some limited range of physical parameters one may characterize thermal equilibrium of the gas with the use of a barotropic index, or “effective γ ,” γ_{eff} , resulting in a simple scaling of pressure with density, $p \propto \rho^{\gamma_{\text{eff}}}$.

The expected lifetimes and structural properties of density enhancements caused by turbulence depend on the average Mach number M and γ_{eff} (the latter can vary over different density regimes). Isothermal turbulence corresponds to $\gamma_{\text{eff}} = 1$, while isobaric turbulence arises from $\gamma_{\text{eff}} = 0$. As γ_{eff} decreases below 1.0, the density peaks become taller, sharper and farther apart, and their lifetimes increase because the effective sound speed decreases (Vázquez-Semadeni, Passot, & Pouquet 1996; Scalo et al. 1998). Also, the (volume weighted) distribution of densities evolves from a log-normal distribution with an extended power-law tail toward low densities when $\gamma_{\text{eff}} > 1$, through a purely symmetrical log-normal distribution at $\gamma_{\text{eff}} = 1$, to a log-normal distribution with a power-law tail on the high density side when $\gamma_{\text{eff}} < 1$ (Passot & Vázquez-Semadeni 1998; Scalo et al. 1998; Nordlund & Padoan 1999). When γ_{eff} dips below zero between two density regimes that have positive values, ρ can be double-valued, and a thermal instability (Field 1965) will cause the gas to bifurcate into two phases (Field, Goldsmith, & Habing 1969; Shull 1987; Begelman 1990; Wolfire et al. 1995), although Kelvin-Helmholtz instabilities and small-scale forcing of the turbulence caused by star formation may often obliterate the distinctive bimodality of densities and make the instability a second-order effect, according to simulations conducted by Vázquez-Semadeni, Gazol & Scalo (2000). Nevertheless, under the right conditions the instability can create very small clumps of dense gas (Burkert & Lin 2000).

Wolfire et al. (1995) have calculated the thermal equilibrium curves in the representation of $\log p$ vs. $\log \rho$ for interstellar gases under a variety of conditions, i.e., different values of column density (which affect the low energy x-ray fluxes), abundances of the principal coolants (C and O), far-UV radiation field strengths, and dust-to-gas ratios. For soft x-ray absorption equivalent to $N(\text{H I}) = 10^{20} \text{ cm}^{-2}$, a reasonable estimate (or lower limit) for most of the individual regions in our lines of sight, the slope of their curve indicates that $\gamma_{\text{eff}} = 0.72$ and the gas is thermally stable for $n \gtrsim 25 \text{ cm}^{-3}$ (and $p/k \gtrsim 10^{3.1} \text{ cm}^{-3} \text{ K}$). However, lower values of γ_{eff} (and a shift for the thermal instability to higher pressures) can arise at these densities when the far-UV radiation field is enhanced, as might be the case for some portions of our lines of sight.

If indeed the lifting of the observed f_2 values above the lower parts of the theoretical tracks (for homogeneous regions having $p/k < 10^4 \text{ cm}^{-3} \text{ K}$ in Fig. 10) is caused by small contributions arising from density fluctuations produced by turbulence, we can use our observations to define a lower limit on γ_{eff} . In essence, we require that the gas responds to compression in a manner such that its trajectory on the $f_1 - f_2$ diagram passes through locations that can pull the measurements of other regions at the same velocity away from the lower portions of the tracks, in a manner that reflects our geometrical interpretation about the effects of gas mixtures that we presented in §6.1. Figure 16 shows the trajectories in the f_1 and f_2 coordinates for gas undergoing compression for two values of γ_{eff} . For the case where $\gamma_{\text{eff}} = 0.72$, it is clear that when we start with a representative unperturbed state having $n = 10 \text{ cm}^{-3}$ and $T = 100 \text{ K}$ (and thus $p/k = 1000 \text{ cm}^{-3} \text{ K}$), the cooling is sufficient to deactivate the C I excitation at higher pressures.

Clearly, we need a value of γ_{eff} that is higher than 0.72 if the initial conditions stand as we have defined them. The curve in Fig. 16 that represents $\gamma_{\text{eff}} = 0.90$ starts from these same initial conditions, but when compressed, it undergoes less severe cooling which in turn makes the C I excitations appear high enough in the diagram to satisfy our need for uplifting the points off the low pressure portions of the tracks (rather than just dragging them toward the right, nearly parallel to the tracks). This modification in γ_{eff} should be expected for smaller regions with a characteristic size of order or less than a critical length L_{cool} given by

$$L_{\text{cool}} = 4 \times 10^{-3} M T_{10}^{-1/2} \text{ pc} \quad (18)$$

where M is the Mach number of the compression and T_{10} is the temperature in units of 10K (Ballesteros-Paredes, Vázquez-Semadeni, & Scalo 1999). This equation applies to the density regime $10^3 \lesssim n \lesssim 10^4 \text{ cm}^{-3}$ where cooling by CO is dominant, and it indicates the scale below which the densities start to change more rapidly than the time needed to reach thermal equilibrium. It follows that as we go to smaller scales, gas accumulations with dimensions less than L_{cool} will begin to respond in a manner such that γ_{eff} deviates from

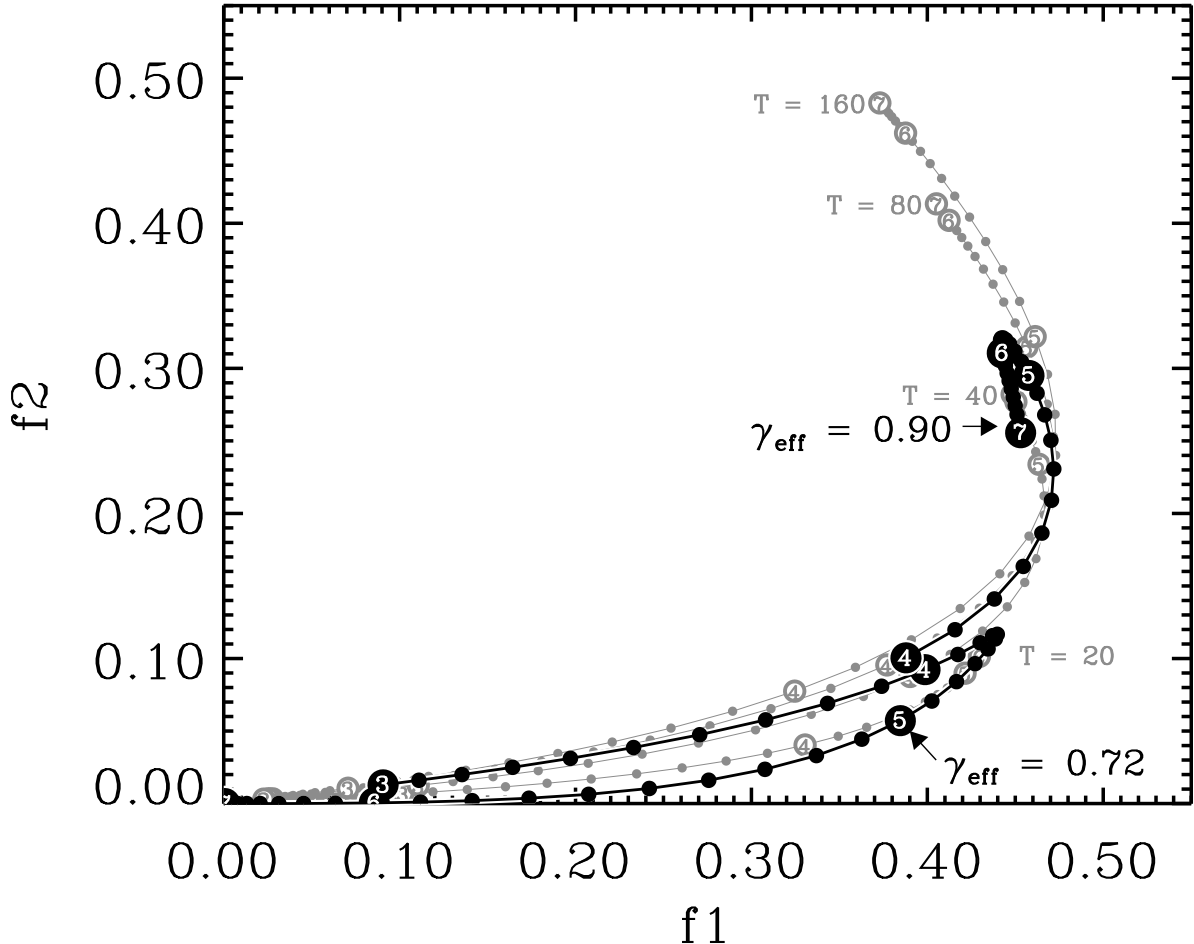


Fig. 16.— Expected evolution of the fine-structure population ratios f_1 and f_2 for gas which is compressed with $\gamma_{\text{eff}} = 0.72$ and 0.90 , starting from initial quiescent conditions $n = 10 \text{ cm}^{-3}$, $T = 100 \text{ K}$ for the thermal pressure $p/k = 1000 \text{ cm}^{-3} \text{ K}$. These (heavy) tracks are superposed on the (lighter) tracks for atomic gas at various specific temperatures (tracing an isothermal $\gamma_{\text{eff}} = 1.00$) as an aid in comparing against the results presented in Figs. 6, 7, and 10. Numbers in the large markers indicate logarithms for the thermal pressures (in units of $\text{cm}^{-3} \text{ K}$). For clarity, the portion of the track for $\gamma_{\text{eff}} = 0.90$ is omitted below $p/k = 10^4 \text{ cm}^{-3} \text{ K}$ because it is so close to that for $\gamma_{\text{eff}} = 0.72$.

the thermal equilibrium predictions and, for the greatest disparities between the thermal equilibrium and compression time scales, approach the adiabatic response, i.e., $\gamma_{\text{eff}} \rightarrow c_p/c_v$ where the gas heats as it is compressed. Fig. 16 illustrates that once the threshold of $\gamma_{\text{eff}} \approx 0.90$ is crossed, the temperatures at high pressures are sufficient to explain the C I excitations.

It is reasonable to suppose that the turbulence will cascade from large to small scales, but for the most part only down to a critical length L_{AD} where ambipolar diffusion would start to dissipate much of the mechanical energy into heat. Klessen, Heitsch & Mac Low (2000) give the formula for L_{AD} ,

$$L_{\text{AD}} = 1.3 \times 10^{-4} \frac{B}{M_A x n^{3/2}} \text{ pc} \quad (19)$$

(see their Eq. 12) where B is the magnetic field strength (in μG), M_A is the Alfvén Mach number, x is the fractional ionization of the gas, and n is the number density of the gas (in cm^{-3}). If we assume that nearly all of the electrons arise from the ionization of carbon, we can set $x = 1.4 \times 10^{-4}$, i.e., the expected fractional abundance of C in the gas (see §5.3.2). Eq. 19 then reduces to $L_{\text{AD}} = n^{-3/2} B / M_A$ which equals $3 \times 10^{-5} \text{ pc}$ if $n = 10^3 \text{ cm}^{-3}$, a density where the elevations in pressure start to become important for exciting C I, and B/M_A is of order unity. We thus can consider a range of length scales $L_{\text{AD}} < L < L_{\text{cool}}$ that spans about two orders of magnitude where compressions can start to become adiabatic in character at the upper end of the range and then weaken as they cascade down to the bottom end where the fluctuations start to dissipate.

The difference between our minimum acceptable value of 0.90 for γ_{eff} and 0.72 implied by the calculations of Wolfire et al. (1995) is small. Effects that they may not have considered that could modify the equilibrium states, including not only the slope in the diagram for $\log \rho$ vs. $\log n$ but also the starting point ($n = 10 \text{ cm}^{-3}$, $T = 100 \text{ K}$), might modify the behavior to give a trajectory that would run high enough in the $f_1 - f_2$ diagram. However, if our conclusion that the regions must be small enough to drive γ_{eff} to values that exceed the prediction for thermal equilibrium is correct, we add some validity to our earlier conjecture about the commonality between our extraordinary pressures and the evidence for small scale structures in the ISM obtained by other means.

It would be interesting investigate further the hypothesis that the distribution of points in Fig. 10 could arise from a turbulent field with a (C I-weighted) density probability function defined from the numerical simulations for given values of the average Mach number and γ_{eff} . However, in order to do so we must know more about the turbulent structures than simply their density probability functions, since the outcomes depend on how well regions with large pressure enhancements are correlated with adjacent material

that has only a moderate elevation of pressure. In addition, we must know how much the one-dimensional velocities change across the typical dimensions of these density enhancements and the degree to which unconnected regions make contributions to a single velocity (in one dimension), e.g., see Figs. 6 and 7 of Ballesteros-Paredes et al. (1999). This information must be derived either from more complete statistical descriptions that include the two-point density correlation function and the coupling of density changes to velocity differences (Klessen 2000) or by simulations that try to duplicate how the C I observations would behave for random interceptions through the density grids of some actual turbulent models. To be realistic for our applications, such models would need to recognize the near equality of turbulent and magnetic energies for very small condensations (Valée 2000) and the dynamical consequences that follow (Passot, Vázquez-Semadeni, & Pouquet 1995).

Finally, we briefly touch upon an entirely different interpretation for the existence of a small amount of gas at high density but not extraordinarily low temperatures. In their proposal to explain the presence of CH^+ and other molecular species that are difficult to produce under standard cloud conditions, Nguyen, Hartquist & Williams (2001) proposed that these molecules could arise from thin, compressed zones at the edges of clouds. (Note here that we are returning to the paradigm of “identifiable clouds immersed in an intercloud medium.”) These zones are pressurized by the Bernoulli effect and heated by the dissipation of waves arising from the Kelvin-Helmholtz instability as cloud moves through a warm, intercloud medium (or is subjected to a flow arising from some byproduct of stellar mass loss or a supernova explosion). Their model for such interfaces that seems to yield the best match to observed molecular abundance ratios has $p/k \approx 4 \times 10^5 \text{ cm}^{-3} \text{ K}$ and $T \approx 2000 \text{ K}$. If this proposal is correct, the interfaces that produce molecules could easily account for the small amount of gas that shows large C I excitations. As with the turbulent fluctuations, the pressurized cloud sheaths could also be commonplace.

9. Conclusions

We have made a survey of interstellar C I in its three levels of fine-structure excitation, creating results that, by virtue of their good velocity resolution (1.5 km s^{-1}), are a considerable refinement over the earlier work of Jenkins & Shaya (1979) and Jenkins et al. (1983) using the *Copernicus* satellite. Except for two of the targets, HD 3827 and HD 120086, all stars are within Galactic longitudes $\ell = 120 \pm 20^\circ$ and $300 \pm 20^\circ$ and latitudes $b = 0 \pm 10^\circ$. With distances that range from about 500 to 3700 pc, many of these stars are located in regions whose velocities arising from differential Galactic rotation are displaced from the Local Standard of Rest by more than 25 km s^{-1} , which allows one to

make crude identifications for the locations of the gas based on kinematics. This velocity separation was especially useful in allowing us to differentiate from the foreground material a special, highly-pressurized region that is probably very near HD 210839 (§6.5).

For each star we created column-density profiles as a function of velocity for each level by analyzing up to 10 multiplets that contain transitions whose strengths spanned 2 orders of magnitude. In order to do so, we had to solve a large system of linear equations to minimize the overall χ^2 , thus enabling us to unravel the complex blends of lines in each multiplet. In order to obtain consistent results from one multiplet to the next, we had to modify the transition f -values from recent results published by others. These modifications are summarized and are compared with the published values in Table 3 (and depicted in Fig. 3). A remarkable effect is that there is a steady divergence between our values and the published ones as the lines become weaker, with very little random scatter in this relation. We discussed several tests which suggest that unresolved saturation is not artificially driving these f -value revisions.

While the amounts of C I found along the lines of sight are of some interest (the total column densities integrated over all velocities toward each star are listed in the last column of Table 6), we regard the ratios of C I in the three levels as the most significant outcome of this survey. These ratios are expressed in terms of f_1 and f_2 , the fractions of carbon in the two excited levels relative to the numbers of atoms in all three levels. It is important to note that validity of the numbers we derived are dependent on the correctness of the assumption that LS coupling applies to the 1657 Å multiplet, one that we chose as a standard for calibrating the strengths of transitions in other, weaker multiplets. Because there is a large separation in energy of its upper electronic level from those of other C I multiplets, we regard the 1657 Å multiplet as being the least likely to suffer perturbations that would cause deviations from the LS coupling rules that govern the relative strengths of lines within the multiplet. We found it reassuring that a comparison of derived pressures from C I agreed with those from O I in a special case where both could be seen together (HD 210839, see §6.5).

After comparing our measurements of f_1 and f_2 to theoretical predictions for various physical and chemical states of the gas, we concluded that a large percentage of the gas has thermal pressures in the general range $10^3 < p/k < 10^4 \text{ cm}^{-3} \text{ K}$. The relative number of C I atoms showing $p/k > 5000 \text{ cm}^{-3} \text{ K}$ is strongly dependent on kinematics: a figure of 15% applies to gas that is moving outside the range bounded by the Local Standard of Rest and the velocity expected for differential Galactic rotation at the position of the target, but this fraction drops by about an order of magnitude for gas within the allowed velocity range (i.e., material that is either quiescent or moving transverse to the line of

sight). This outcome is consistent with the notion that rapidly moving gas parcels are likely to experience compressions leading to pressures that are noticeably elevated compared to undisturbed material. We found no strong indication that pressurized regions containing C I were favored at velocities where there was evidence for ionized gases, as indicated by the presence of Si II*. At the opposite extreme, about 3% of the C I bearing gas seems to have a gas pressure well below the total p/k of $3 \times 10^4 \text{ cm}^{-3} \text{ K}$ (Boulares & Cox 1990) caused by the weight of material within the Galactic gravitational potential. We propose that this condition arises from rarefactions, probably from the same dynamical processes that create the compressions.

For quantitative statements about the amount of material in various pressure regimes, we emphasize that it is important to realize that the results are weighted by the local abundances of C I. For regions that have a lifetime greater than about 1000 yr, i.e., the time needed to reach ionization equilibrium for the normal average intensity of ionizing radiation, the C I abundance scales in proportion to the local density of electrons, which in turn is usually proportional to the total density of atoms since the electrons principally come from the photoionization of C. One must factor in this consideration when trying to make quantitative statements about the fractions of hydrogen at various pressures.

Finally, it is no surprise that we occasionally find values of f_1 and f_2 indicating C I-bearing gases exclusively at $p/k \gtrsim 10^5 \text{ cm}^{-3} \text{ K}$. The clearest manifestation of this is the component at -35 km s^{-1} in front of HD 210839, where there is no evidence that this material is mixed with lower pressure gas. In all cases, this same material also shows excited O I, and it probably is the result of pressurization by the winds or expanding H II regions created by the target stars and their association companions. However, somewhat unexpectedly we also found evidence that overpressured gases may be rather pervasive, although the amounts are small. This conclusion arises from our finding that most of the C I seen at specific velocities shows an excess in the values of f_2 relative to expectations from their f_1 counterparts. If this effect is real and not due to errors in the assumptions about LS coupling (see above) or the collisional rate constants used in our calculations of the expected level populations, we conclude that a very small fraction of the gas exists at extraordinary pressures $p/k \gtrsim 10^5 \text{ cm}^{-3} \text{ K}$, that is, at least 2 orders of magnitude above the overall average. The widespread nature of this material indicates that it arises from some generalized property of the medium, rather than isolated, unusual events. We suggest that compressions created from interstellar turbulence are a likely source of this effect.

If turbulent motions are indeed the explanation for the compressions, we conclude that the affected regions must be small, because we require that the barytropic index γ_{eff} of the gas must be greater than predictions based on thermal equilibria at different densities. This

could happen if the regions had a compression that was closer to adiabatic in character, as we would expect if characteristic dimensions were less than about 10^{-2} pc and there was insufficient time for the gas to reach thermal equilibrium by various radiative processes before it re-expanded (or collapsed further). It is important to note that the characteristic time for cooling $(3/2)kT/\Lambda = 5 \times 10^{12} n^{-1} \text{ cm}^{-3} \text{s}$, if $\Lambda n^{-2} = 4 \times 10^{-27} \text{ erg cm}^{-3} \text{s}^{-1}$ (Dalgarno & McCray 1972) and $T = 100 \text{ K}$, is 4 orders of magnitude shorter than the timescale for forming an appreciable concentration of molecular hydrogen, $R^{-1}n^{-1}$ for an H_2 formation rate constant $R = 2 \times 10^{-17} \text{ cm}^3 \text{s}^{-1}$ (Hollenbach & McKee 1979) at the same temperature. Since our C I evidence indicates that the lifetimes of the compressed states are comparable to or shorter than this cooling time, it follows that Heiles's (1997) objection to small structures based on excessive molecule formation, a point we raised in §8, is not a problem. This now eliminates an important reason that supported Heiles's proposal that the small scale structures must simply be curved sheets or filaments viewed edge-on.

From the considerations expressed above, we are persuaded that small-scale, short-lived structures formed by turbulent motions in the interstellar medium are a likely source for small amounts of overpressurized material. The plausibility of this interpretation is reinforced by various types of observations that indicate the existence of density enhancements over scales ranging upwards from about 10 pc. In effect, our results may serve as an independent confirmation of their existence. Perhaps more important, the C I fine-structure levels can give insights on the nature of these regions, such as the fact that they are not extremely cold. Also, our results can be compared to predictions from contemporary models of interstellar turbulence, with the objective of supplying some useful constraints on the free parameters.

We thank K. Sembach for supplying IDL Legendre polynomial fitting modules that we implemented for our continuum definitions (§4.4). Discussions with J. Zsargó and S. Federman were useful in our re-examinations of the newly derived f -values presented in §5.3. We benefitted from discussions with M. Mac Low and B. Draine on various aspects of interstellar turbulence. We thank C. Bowers and F. Roesler for their willingness to contribute some of their personal observing time for this project under the block of time allocated for the STIS Team Guaranteed Observing with HST. This research was supported by NASA Grant NAS5-30110 to Princeton University.

A. STIS Wavelength Resolving Power

The research discussed here clearly benefits from our having the highest resolution possible, since the ionization equilibrium of carbon imposes the condition that absorption features from the neutral state preferentially arise from dense gas regions that are likely to have small velocity dispersions. In fact, C I should behave much like Na I or K I, species that can be detected at visible wavelengths and are known to have narrow features (Welty, Hobbs, & Kulkarni 1994; Welty & Hobbs 2001). It is for this reason that we placed strong emphasis on achieving the highest wavelength resolution that STIS could provide, leading to the selection of the E140H and E230H echelle gratings with the narrowest possible entrance slit (§3).

Along with the rigorous demands our program placed to register narrow velocity structures, there is also an opportunity before us to use these features as a way to learn about the wavelength resolving power of STIS in its highest resolution mode. To accomplish this, we searched for the best example of an isolated, narrow C I feature and assumed that its intrinsic width is small enough to reveal the full potential of the instrument to register small differences in velocity.

In principle, a study of this sort must be done with care, since two effects can distort the conclusions. On the one hand, a feature that is thought to be narrow but is indeed intrinsically broad enough to degrade the profile may lead to an underestimate of the instrument's resolving power. This problem grows worse as the feature is reflected in stronger transitions where saturation sets in. On the other hand, the selection of the narrowest, weak features that can be seen in a spectrum may lead to an error in the opposite direction. The chance effects of noise can spuriously narrow or broaden an outcome for any feature that is not seen at extraordinarily good S/N , and selecting only the narrowest features will unfairly favor the noise effects that operate in one direction only. To overcome these problems as best we could, we selected a velocity component that seemed to be narrower than all the rest in our survey. Next, as evenhandedly as possible, we measured the widths all manifestations of this component in the different multiplets. We excluded only those cases where the lines were either too weak to be seen or were clearly compromised by interference from other lines or extreme saturation. We added to the sample three of the strongest lines of S I. This element, like carbon, is below its favored ionization stage for H I regions when it is neutral.

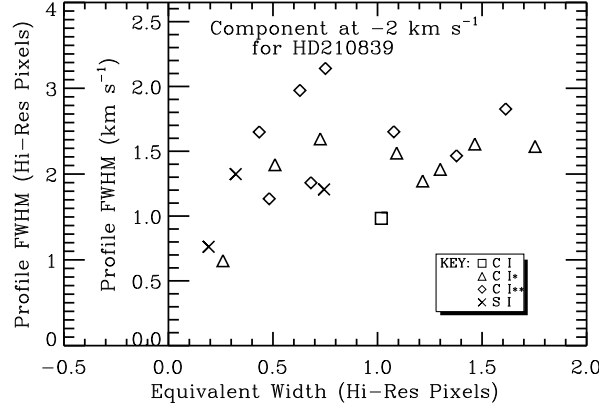


Fig. 17.— Widths (FWHM) of best-fit, inverted Gaussians that match the intensity profiles recorded by STIS operating in the E140H mode with its narrowest ($0''.1 \times 0''.03$) entrance slit. Measurements of different transitions arising from C I, C I*, C I** and S I, as indicated by plot symbols, apply to an interstellar velocity component at -2 km s^{-1} in the spectrum of HD 210839. These widths (ordinates) are plotted against line strengths (abscissae), expressed as equivalent widths in units of a Hi-Res pixel of the far-UV MAMA detector.

Table 9 shows the results for many measurements of our selected component: a feature at -2 km s^{-1} in the spectrum of HD 210839 recorded with the E140H grating. We chose to measure the widths of individual transitions, rather than the width of the component expressed in our derived composite $N_a(v)$, so that the outcome would not be compromised by deficiencies in our velocity registrations (§4.5), errors in the scale factors for Å/pixel along a single diffraction order, or small offsets in the published laboratory wavelengths from the true separations of transitions within a multiplet. The widths given in the table represent the FWHM for a best (minimum χ^2) fit of the intensity to a single Gaussian profile that is inverted.

To obtain a better understanding about whether or not the results depended on line strength, we plotted the apparent widths of the profiles as a function of their equivalent widths (expressed in units of a Hi-Res pixel). This plot is presented in Fig. 17. The strong lines do not seem to be significantly wider than the weak ones, which indicates that saturation is probably not an important factor in broadening these particular lines. As expected, the weak lines show more scatter caused by the influence of random noise.

From the average location of points shown in Fig. 17, it seems reasonable to conclude that the resolution of the E140H mode of STIS, as configured for our survey, is $R = 200,000$ (for the profile's FWHM) which equals 1.5 km s^{-1} . This assumes, of course, that the profile

Table 9. Line Widths^a for a Component at -2 km s^{-1} in the Spectrum of HD 210839

λ (Å)	Origin	Equivalent Width W (Hi-Res Pixels)	Profile FWHM (Hi-Res Pixels)
1329.123	C I*	1.300	2.055
1329.578	C I**	1.078	2.493
1329.600	C I**	0.434	2.490
1279.890	C I*	1.465	2.350
1280.333	C I**	0.482	1.712
1280.404	C I*	0.726	2.410
1280.597	C I*	1.092	2.245
1279.056	C I*	0.261	0.990
1277.723	C I**	1.378	2.213
1277.550	C I**	1.613	2.758
1277.723	C I**	0.751	3.231
1277.723	C I**	0.629	2.975
1276.483	C I	1.018	1.484
1276.750	C I*	0.509	2.109
1260.927	C I*	1.753	2.322
1261.122	C I*	1.216	1.919
1261.552	C I**	0.681	1.899
1316.542	S I	0.322	1.999
1296.174	S I	0.192	1.152
1295.653	S I	0.744	1.821

^aLeast-squares fits of the observed profiles to those of inverted, single Gaussian profiles of the form $I = I_0\{1 - D\exp[-(x-x_0)^2/2\sigma^2]\}$, where each profile's center x_0 , depth D , and standard deviation σ are free parameters that arise from a minimum χ^2 . The equivalent widths W (column 3) equal $(2\pi)^{1/2}\sigma D$. The widths listed in column 4 are given in terms of the profiles' full width at half maxima $\text{FWHM} = 2^{3/2}(\ln 2)^{1/2}\sigma$. The data listed here are plotted in Fig. 17.

has an intrinsic width that is much smaller than 1.5 km s^{-1} .

Unfortunately, we were unable to perform a good measurement of the resolution of STIS operating with the E230H grating. The only absorption line in Multiplet 1 (the only multiplet covered by our longer wavelength setting) that was weak enough to be unsaturated for the -2 km s^{-1} component was the one arising from the weak transition from C I** at 1658.1 Å. A satisfactory measurement of this line could not be made because the amplitude of the noise was about half as large as the line depth.

B. Telluric Profiles of O I* and O I**

Initially, when we attempted to determine the resolution of STIS we thought that features at 1304.858 Å and 1306.039 Å arising from excited oxygen atoms in the Earth’s upper atmosphere would yield appropriate signals for this task. These features are especially strong for our observing program because most of our targets are in the CVZ (§2), a configuration that typically produces large zenith angles for the telescope’s viewing axis. They rarely suffer from interference from interstellar O I* and O I** (§6.4). Moreover, the fact that both lines are near the ends of the echelle diffraction orders meant that we could sense them twice at very different locations on the MAMA detector. This made the lines especially attractive, since we could obtain double the normal number of measurements and look for possible changes in resolution along one of the image dimensions.

After we had examined the C I data, it was clear that the telluric profiles are indeed resolved by STIS, or at least partially so, and thus inappropriate for measuring the resolving power of STIS. Nevertheless, the outcomes are of possible use in understanding the properties of Earth’s atmosphere above the altitude of HST’s orbit.

Figure 18 shows the recorded widths of the telluric O I* and O I** features, plotted as a function of their central intensities. We did not employ the Gaussian fitting procedures discussed §A because distortions that arise when the lines become saturated lead to poor fits. For comparison, the expected behavior for lines of different strength arising from oxygen atoms with no macroscopic velocities but with a Doppler broadening corresponding to $T = 2000 \text{ K}$ is also shown (line with ×’s). These expected profiles are Voigt profiles convolved with the STIS line-spread function (assuming it’s Gaussian), whose determination was described in §A.

Weak profiles are consistent with a pure Doppler broadening at $T = 2000 \text{ K}$, an amount that exceeds generally accepted value of around 1000 K for the temperature of the Earth’s exosphere, such as that given in the MSIS-86 model atmosphere (Meier 1991). As the

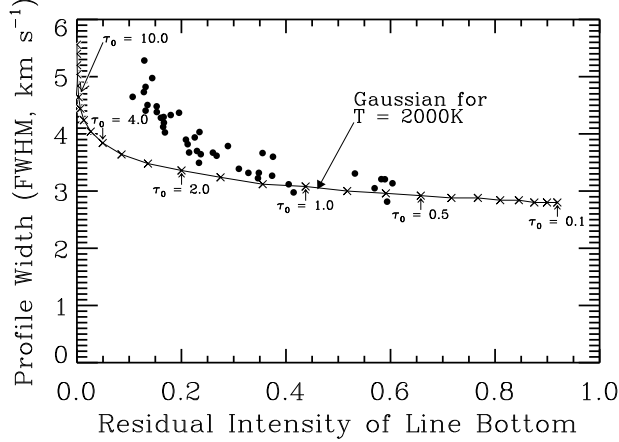


Fig. 18.— Measured widths (FWHM) of the telluric O I* and O I** profiles for the transitions at 1304.858 Å and 1306.039 Å, respectively, plotted against their minimum intensities. As the lines become stronger (going from right to left in the plot), they broaden. While this behavior is expected as the lines saturate, they do so faster than that expected for a pure Gaussian velocity profile seen at the STIS resolution, as indicated by the line with \times 's and markers for the central optical depths τ_0 .

profiles grow stronger (due in large part to higher zenith angles of the observations) they broaden faster than the expected behavior of a simple Voigt profile. Evidently, the wings of the profile suggest the presence of some bulk macroscopic motions in the upper atmosphere of the Earth.

REFERENCES

- Abbott, D. C. 1982, ApJ, 263, 723
 Anders, E., & Grevesse, N. 1989, Geochim. Cos. Acta, 53, 197
 Ballesteros-Paredes, J., Vázquez-Semadeni, E., & Scalo, J. 1999, ApJ, 515, 286
 Bally, J. 1982, in Regions of Recent Star Formation, ed. R. S. Roger & P. E. Dewdney (Dordrecht: Reidel), p. 287
 Begelman, M. C. 1990, in The Interstellar Medium in Galaxies, ed. H. Thronson & M. Shull (Dordrecht: Kluwer), p. 287
 Bergeson, S. D., & Lawler, J. E. 1993, ApJ, 414, L137
 Boulares, A., & Cox, D. P. 1990, ApJ, 365, 544
 Bracewell, R. 1965, The Fourier Transform and Its Applications, (New York: McGraw-Hill)

- Burkert, A., & Lin, D. N. C. 2000, ApJ, 537, 270
- Cardelli, J. A., Savage, B. D., Bruhwiler, F. C., Smith, A. M., Ebbets, D. C., Sembach, K. R., & Sofia, U. J. 1991, ApJ, 377, L57
- Cardelli, J. A., Mathis, J. S., Ebbets, D. C., & Savage, B. D. 1993, ApJ, 402, L17
- Cardelli, J. A., Meyer, D. M., Jura, M., & Savage, B. D. 1996, ApJ, 467, 334
- Castor, J. C., McCray, R., & Weaver, R. 1975, ApJ, 200, L107
- Chandrasekhar, S., & Münch, G. 1952, ApJ, 115, 103
- Clemens, D. P. 1985, ApJ, 295, 422
- Conti, P. S., & Alschuler, W. R. 1971, ApJ, 170, 325
- Cox, D. P. 1979, ApJ, 234, 863
— 1981, ApJ, 245, 534
- Cox, D. P., & Smith, B. W. 1974, ApJ, 189, L105
- Crane, P., Lambert, D. L., & Sheffer, Y. 1995, ApJS, 99, 107
- Cunha, K., & Lambert, D. L. 1994, ApJ, 426, 170
- Dalgarno, A., & McCray, R. A. 1972, ARA&A, 10, 375
- Davis, R. J., Diamond, P. J., & Goss, W. M. 1996, MNRAS, 283, 1105
- Deshpande, A. A. 2000, MNRAS, 317, 199
- Diamond, P. J., Goss, W. M., Romney, J. D., Booth, R. S., Kalberla, P. M. W., & Mebold, U. 1989, ApJ, 347, 302
- Dieter, N. H., Welch, W. J., & Romney, J. D. 1976, ApJ, 206, L113
- Diplas, A., & Savage, B. D. 1994, ApJS, 93, 211
- Drake, J. F., & Pottasch, S. R. 1977, A&A, 54, 425
- Elmegreen, B. G. 1993a, in Star Formation, Galaxies and the Interstellar Medium, ed. J. Franco, F. Ferrini & G. Tenorio-Tagle (Cambridge: Cambridge Univ.), p. 337
— 1993b, ApJ, 419, L29
— 1997, ApJ, 480, 674
— 1999, ApJ, 527, 266
- Evans, D. S. 1967, in Determination of Radial Velocities and their Applications, ed. A. H. Batten & J. F. Heard (London: Academic Press), p. 57
- Faison, M. D., Goss, W. M., Diamond, P. J., & Taylor, G. B. 1998, AJ, 116, 2916

- Federman, S. R., & Cardelli, J. A. 1995, ApJ, 452, 269
- Federman, S. R., Sheffer, Y., Lambert, D. L., & Gilliland, R. L. 1993, ApJ, 413, L51
- Ferlet, R., Laurent, C., Vidal-Madjar, A., & York, D. G. 1980, ApJ, 235, 478
- Field, G. B. 1965, ApJ, 142, 531
- Field, G. B., Goldsmith, D. W., & Habing, H. J. 1969, ApJ, 155, L149
- Fitzpatrick, E. L., & Spitzer, L. 1994, ApJ, 427, 232
- 1997, ApJ, 475, 623
- Fixsen, D. J., Bennett, C. L., & Mather, J. C. 1999, ApJ, 526, 207
- Frail, D. A., Weisberg, J. M., Cordes, J. M., & Mathers, C. 1994, ApJ, 436, 144
- Frisch, P. C. 1980, ApJ, 241, 697
- Froese Fischer, C., & Saha, H. P. 1985, Physica Scripta, 32, 181
- Garrison, R. F., Hiltner, W. A., & Schild, R. E. 1977, ApJS, 35, 111
- Genzel, R., & Downes, D. 1982, in Regions of Recent Star Formation, ed. R. S. Roger & P. E. Dewdney (Dordrecht: Reidel), p. 251
- Gibson, S. J., Taylor, A. R., Higgs, L. A., & Dewdney, P. E. 2000, ApJ, 540, 851
- Hébrard, G., Mallouris, C., Ferlet, R., Koester, D., Lemoine, M., Vidal-Madjar, A., & York, D. 1999, A&A, 350, 643
- Heiles, C. 1979, ApJ, 229, 533
- 1997, ApJ, 481, 193
- Hill, G., & Fisher, W. A. 1987, A&A, 171, 123
- Hill, P. W. 1970, MNRAS, 150, 23
- Hobbs, L. M. 1976, ApJ, 203, 143
- Hobbs, L. M., & Welty, D. E. 1991, ApJ, 368, 426
- Hobbs, L. M., York, D. G., & Oegerle, W. 1982, ApJ, 252, L21
- Hollenbach, D., & McKee, D. F. 1979, ApJS, 41, 555
- Howarth, I. D., Siebert, K. W., Hussain, G. A. J., & Prinja, R. K. 1997, MNRAS, 284, 265
- Howk, J. C., Savage, B. D., & Fabian, D. 1999, ApJ, 525, 253
- Huang, M., Bania, T. M., Bolatto, A., Chamberlin, R. A., Ingalls, J. G., Jackson, J. M., Lane, A. P., Stark, A. A., Wilson, R. W., & Wright, G. A. 1999, ApJ, 517, 282
- Hunter, J. H., Sandford, M. T., Whitaker, R. W., & Klein, R. I. 1986, ApJ, 305, 309

- Hurwitz, M., Appenzeller, I., Barnstedt, J., Bowyer, S., Dixon, W. V., Grewing, M., Kappelmann, N., Krämer, G., Krautter, J., & Mandel, H. 1998, ApJ, 500, L61
- Hutchings, J. B. 1975, ApJ, 200, 122
- Jenkins, E. B. 1996, ApJ, 471, 292
- Jenkins, E. B., Jura, M., & Loewenstein, M. 1983, ApJ, 270, 88
- Jenkins, E. B., & Shaya, E. J. 1979, ApJ, 231, 55
- Jenkins, E. B., & Wallerstein, G. 1995, ApJ, 440, 227
- Jenkins, E. B., Silk, J., Wallerstein, G., & Leep, E. M. 1981, ApJ, 248, 977
- Jenkins, E. B., Tripp, T. M., Fitzpatrick, E. L., Lindler, D., Danks, A. C., Beck, T. L., Bowers, C. W., Joseph, C. L., Kaiser, M. E., Kimble, R. A., Kraemer, S. B., Robinson, R. D., Timothy, J. G., Valenti, J. A., & Woodgate, B. E. 1998, ApJ, 492, L147
- Johnson, C. T., Burke, P. G., & Kingston, A. E. 1987, J. Phys. B, 20, 2553
- Johnson, H. L. 1963, in Stars and Stellar Systems, ed. K. A. Strand (Chicago: U. Chicago Press), p. 204
- Johnson, H. L., & Morgan, W. W. 1953, ApJ, 117, 313
- Jones, E. M., Smith, B. W., Straka, W. C., Kodis, J. W., & Guitar, H. 1979, ApJ, 232, 129
- Kasle, D. B., & Morgan, J. S. 1991, in EUV, X-Ray, and Gamma-Ray Instrumentation for Astronomy II, ed. O. H. Siegmund & R. E. Rothschild (Bellingham: SPIE), p. 52
- Keenan, F. P. 1989, ApJ, 339, 591
- Keenan, F. P., & Berrington, K. A. 1988, ApJ, 333, 806
- Keenan, F. P., Johnson, C. T., Kingston, A. E., & Dufton, P. L. 1985, MNRAS, 214, 37p
- Kerr, F. J., & Lynden-Bell, D. 1986, MNRAS, 221, 1023
- Kimble, R. A. et al. 1998, ApJ, 492, L83
- Klessen, R. S. 2000, ApJ, 535, 869
- Klessen, R. S., Heitsch, F., & Mac Low, M. 2000, ApJ, 535, 887
- Königl, A. 1996, in Disks and Outflows Around Young Stars, ed. S. Beckwith, J. Staude, A. Quetz & A. Natta (Berlin: Springer), p. 282
- Kurucz, R. L. 1993, in Peculiar Versus Normal Phenomena in A-Type and Related Stars, ed. M. M. Dworetsky, F. Castelli & R. Faraggiana (San Francisco: Astron. Soc Pacific), p. 87

- 1997, in Fundamental Stellar Properties: the Interaction between Observation and Theory, ed. T. R. Bedding, A. J. Booth & J. Davis (Dordrecht: Kluwer), p. 217
- Lamers, H. J. G. L. M. 1981, ApJ, 245, 593
- Lamers, H. J. G. L. M., Harzevoort, J. M. A. G., Schrijver, H., Hoogerwerf, R., & Kudritzki, R. P. 1997, A&A, 325, L25
- Larson, R. B. 1981, MNRAS, 194, 809
- Launay, J. M., & Roueff, E. 1977, A&A, 56, 289
- Lauroesch, J. T., & Meyer, D. M. 1999, ApJ, 519, L181
- Lauroesch, J. T., Meyer, D. M., & Blades, J. C. 2000, ApJ, 543, L43
- Lauroesch, J. T., Meyer, D. M., Watson, J. K., & Blades, J. C. 1998, ApJ, 507, L89
- Leitherer, C. 2000, Space Telescope Imaging Spectrograph Instrument Handbook for Cycle 10, 4.1 ed., (Baltimore: Space Telescope Science Institute)
- Lemoine, M., Ferlet, R., & Vidalmadjar, A. 1995, A&A, 298, 879
- Lesh, J. R. 1968, ApJS, 16, 371
- Lindler, D., & Bowers, C. 2001, BAAS, AAS 197th meeting, paper 12.02
- Luo, D., Pradhan, A. K., & Shull, J. M. 1988, ApJ, 335, 498
- Mac Low, M.-M., McCray, R., & Norman, M. L. 1989, ApJ, 337, 141
- Marscher, A. P., Moore, E. M., & Bania, T. M. 1993, ApJ, 419, L101
- McCray, R., & Snow, T. P. 1979, ARA&A, 17, 213
- McKee, C. F. 1986, Ap&SS, 118, 383
- McKee, C. F., & Ostriker, J. P. 1977, ApJ, 218, 148
- Meier, R. R. 1991, Space Sci. Rev., 58, 1
- Mermilliod, J.-C. 1987, A&AS, 71, 413
- Meyer, D. M., & Blades, J. C. 1996, ApJ, 464, L179
- Meyer, D. M., & Lauroesch, J. T. 1999, ApJ, 520, L103
- Mihalas, D., & Binney, J. 1981, Galactic Astronomy Structure and Kinematics, 2nd ed., (New York: Freeman)
- Moore, E. M., & Marscher, A. P. 1995, ApJ, 452, 671
- Morgan, W. W., Code, A. D., & Whitford, A. E. 1955, ApJS, 2, 41
- Morton, D. C. 1991, ApJS, 77, 119

- 1992, ApJS, 81, 883
- Mosteller, F., & Tukey, J. W. 1977, Data Analysis and Regression a Second Course in Statistics, (Reading, Mass: Addison-Wesley)
- Nguyen, T. K., Hartquist, T. W., & Williams, D. A. 2001, A&A, 366, 662
- Nordlund, A., & Padoan, P. 1999, in Interstellar Turbulence, ed. J. Franco & A. Carramiñana (Cambridge: Cambridge Univ.), p. 218
- Nussbaumer, H. 1977, A&A, 58, 291
- Passot, T., & Vázquez-Semadeni, E. 1998, Physical Review E, 58, 4501
- Passot, T., Vázquez-Semadeni, E., & Pouquet, A. 1995, ApJ, 455, 536
- Patel, N. A., Goldsmith, P. F., Heyer, M. H., Snell, R. L., & Pratap, P. 1998, ApJ, 507, 241
- Petrie, R. M., & Petrie, J. K. 1967, Publications of the Dominion Astrophysical Observatory, 13, 101
- Press, W. H., Teukolsky, S. A., Vetterling, W. T., & Flannery, B. P. 1992, Numerical Recipes in Fortran, 2nd ed., (Cambridge: Cambridge Univ. Press)
- Rogerson, J. B., Spitzer, L., Drake, J. F., Dressler, K., Jenkins, E. B., Morton, D. C., & York, D. G. 1973, ApJ, 181, L97
- Roueff, E., & Le Bourlot, J. 1990, A&A, 236, 515
- Savage, B. D., & Sembach, K. R. 1991, ApJ, 379, 245
- 1996, ARA&A, 34, 279
- Scalo, J., Vázquez-Semadeni, E., Chappell, D., & Passot, T. 1998, ApJ, 504, 835
- Schaller, G., Schaerer, D., Meynet, G., & Maeder, A. 1992, A&AS, 96, 269
- Schröder, K., Staemmler, V., Smith, M. D., Flower, D. R., & Jaquet, R. 1991, J. Phys. B, 24, 2487
- Schulz, N. S., Berghöfer, T. W., & Zinnecker, H. 1997, A&A, 325, 1001
- Sembach, K. R., & Savage, B. D. 1992, ApJS, 83, 147
- Shull, J. M. 1987, in Interstellar Processes, ed. D. J. Hollenbach & H. A. Thronson (Dordrecht: Reidel), p. 225
- Shull, J. M., & Van Steenberg, M. 1982, ApJS, 48, 95
- Smith, A. M., Bruhweiler, F. C., Lambert, D. L., Savage, B. D., Cardelli, J. A., Ebbets, D. C., Lyu, C.-H., & Sheffer, Y. 1991, ApJ, 377, L61
- Smith, B. W. 1977, ApJ, 211, 404

- Snow, T. P. 1976, ApJ, 204, 759
- Sofia, U. J., Cardelli, J. A., & Savage, B. D. 1994, ApJ, 430, 650
- Sofia, U. J., Fitzpatrick, E. L., & Meyer, D. M. 1998, ApJ, 504, L47
- Sofia, U. J., Cardelli, J. A., Guerin, K. P., & Meyer, D. M. 1997, ApJ, 482, L105
- Spitzer, L. 1978, Physical Processes in the Interstellar Medium, 1st ed., (New York: Wiley)
- Spitzer, L., & Fitzpatrick, E. L. 1993, ApJ, 409, 299
- 1995, ApJ, 445, 196
- Spitzer, L., & Jenkins, E. B. 1975, ARA&A, 13, 133
- Staemmler, V., & Flower, D. R. 1991, J. Phys. B, 24, 2343
- Stickland, D. J. 1995, Observatory, 115, 180
- Thackeray, A. D., Tritton, S. B., & Walker, E. N. 1973, MmRAS, 77, 199
- Thompson, G. I., Nandy, K., Jamar, C., Monfils, A., Houziaux, L., Carnochan, D. J., & Wilson, R. 1978, Catalogue of Stellar Ultraviolet Fluxes, (Science Research Council)
- Tokunaga, A. T. 2000, in Allen's Astrophysical Quantities, ed. A. N. Cox (New York: Springer), p. 719
- Uesugi, A., & Fukuda, I. 1981, in Data for Science and Technology, Proceedings of the Seventh International CODATA Conference Kyoto, Japan, 8-11 October 1980, ed. P. S. Glaeser (Oxford: Pergamon), p. 201
- Vacca, W. D., Garmany, C. D., & Shull, J. M. 1996, ApJ, 460, 914
- Valée, J. P. 2000, ApJ, 538, 226
- Vallerga, J. V., Vedder, P. W., Craig, N., & Welsh, B. Y. 1993, ApJ, 411, 729
- van Dishoeck, E. F. 1988, in Rate Coefficients in Astrochemistry, ed. T. J. Millar & D. A. Williams (Dordrecht: Kluwer), p. 49
- Vázquez-Semadeni, E., Gazol, A., & Scalo, J. 2000, ApJ, 540, 271
- Vázquez-Semadeni, E., Passot, T., & Pouquet, A. 1995, ApJ, 441, 702
- 1996, ApJ, 473, 881
- Vidal-Madjar, A., Laurent, C., Bonnet, R. M., & York, D. G. 1977, ApJ, 211, 91
- Vreux, J.-M., & Conti, P. S. 1979, ApJ, 228, 220
- Wada, K., Spaans, M., & Kim, S. 2000, ApJ, 540, 797
- Walborn, N. R. 1971, ApJS, 23, 257

- 1972, AJ, 77, 312
- 1973, AJ, 78, 1067
- Wannier, P., Andersson, B.-G., Penprase, B. E., & Federman, S. R. 1999, ApJ, 510, 291
- Watson, J. K., & Meyer, D. M. 1996, ApJ, 473, L127
- Weaver, R., McCray, R., Castor, J., Shapiro, P., & Moore, R. 1977, ApJ, 218, 377
- Weikard, H., Wouterloot, J. G. A., Castets, A., Winnewisser, G., & Sugitani, K. 1996, A&A, 309, 581
- Weingartner, J. C., & Draine, B. T. 2001, astro-ph/0105237
- Welsh, B. Y., Vedder, P. W., & Vallerga, J. V. 1990, ApJ, 358, 473
- Welsh, B. Y., Vedder, P. W., Vallerga, J. V., & Craig, N. 1991, ApJ, 381, 462
- Welty, D. E., & Hobbs, L. M. 2001, ApJS, 133, 345
- Welty, D. E., Hobbs, L. M., & Kulkarni, V. P. 1994, ApJ, 436, 152
- Welty, D. E., Hobbs, L. M., & York, D. G. 1991, ApJS, 75, 425
- Wesselius, P. R., van Duinen, R. J., de Jonge, A. R. W., Aalders, J. W. G., Luinge, W., & Wildeman, K. J. 1982, A&AS, 49, 427
- Wiese, W. L., Fuhr, J. R., & Deters, T. M. 1996, Atomic Transition Probabilities of Carbon, Nitrogen, and Oxygen: A Critical Data Compilation, (Journal of Physical and Chemical Reference Data Monographs, 7), (Washington: American Chem. Soc. and American Phys. Soc. for NIST)
- Wilson, R. E. 1953, General Catalogue of Stellar Radial Velocities, (Washington: Carnegie Inst.)
- Wolfire, M. G., Hollenbach, D., McKee, C. F., Tielens, A. G. G. M., & Bakes, E. L. O. 1995, ApJ, 443, 152
- Woodgate, B. E. et al. 1998, PASP, 110, 1183
- Wright, E. L., Mather, J. C., Bennett, C. L., Cheng, E. S., Shafer, R. A., Fixsen, D. J., Eplee, R. E., Jr., Isaacman, R. B., Read, S. M., Boggess, N. W., Gulkis, S., Hauser, M. G., Janssen, M., Kelsall, T., Lubin, P. M., Meyer, S. S., Moseley, S. H., Jr., Murdock, T. L., Silverberg, R. F., Smoot, G. F., Weiss, R., & Wilkinson, D. T. 1991, ApJ, 381, 200
- Zsargó, J., Federman, S. R., & Cardelli, J. A. 1997, ApJ, 484, 820